THEORETICAL INVESTIGATION OF SATURABLE ABSORPTION IN GRAPHENE

WANG QIAN

NATIONAL UNIVERSITY OF SINGAPORE

2012

THEORETICAL INVESTIGATION OF SATURABLE ABSORPTION IN GRAPHENE

WANG QIAN

(B.Sc, SHANDONG UNIV)

A THESIS SUBMITTED

FOR THE DEGREE OF MASTER OF SCIENCE

DEPARTMENT OF PHYSICS

NATIONAL UNIVERSITY OF SINGAPORE

2012

ACKNOWLEDGEMENTS

It is my great pleasure to take this opportunity to thank those who have supported and helped me to complete this thesis. Their assistance and encouragement are extremely precious to me at every stage of this long and enduring journey.

First and foremost, I would like to express my deepest appreciation to my supervisor, Prof. Ji Wei, for his unfailing and indispensable guidance, constant support and consistent encouragement throughout my thesis. He led me into the fantastic world of nonlinear optics with his expertise, enthusiasm, wide knowledge and logical way of thinking, and always offered me many constructive suggestions and guidance every time when I came across failures or difficulties on the challenging road of exploration. Despite his busy schedule as the vice dean of Faculty of Science, he spent plenty of time and endeavors in discussing with me and revising my manuscript and thesis word by word with greatest diligence and patience. I could not expect a better advisor and mentor for my Master project, which could not have come to fruition without his persistent guidance and hard work.

I would like to express my sincerest gratitude to Dr. Yang Hongzhi, who taught me many experimental skills, gave me lots of advice and stimulated me to make greater efforts to fulfill my project. In particular, the experimental measurements on our graphene samples in this thesis were mainly produced by Dr. Yang with my assistance.

Much appreciation also goes to Prof. Chen Wei and Dr. Huang Han for many valuable suggestions for my research project. Furthermore, the epitaxial graphene samples used in the experiments in this thesis were supported by them.

My sincere gratefulness is also directed to my group members and all my friends in NUS. To Dr. Xing Guichuan, Dr. Venkatram Nalla, Dr. Venkatesh Mamidala, Mr. Mohan Singh Dhoni, Dr. Feng Xiaobo and Dr. Gu Bing for their kind support and fruitful discussions. To Yuzhan, Yingying, Xiaqing, Fusheng, Chen Yu, Chen Xiao, Huihui, Junpeng, Hongwei, Wentao, Yinghui for their cooperation, valuable discussions and help.

Personally, I am appreciative to my parents for their everlasting love, endless trust and unconditional understanding since I was born; to my brother who has been always supportive and tolerant. And I offer my honest thanks to my beloved fiancé, Guanggeng, who has been always thoughtful and selfless to give me strength for the completion of the thesis.

Due to the limited space, I hereby express my deep appreciation to all the people that I do not mention who have contributed to the efforts that made this dissertation possible.

TABLE OF CONTENTS

ABSTRACT

The unique electronic and optical properties of graphene have attracted wide attention in a variety of research areas. Specifically, graphene has been demonstrated as a promising saturable absorber, due to its wavelength-independent broadband absorption, ultrafast recovery time, high modulation depth, and low-cost fabrication techniques. It has great advantages in ultrashort laser pulse generation by passive mode-locking. Hence, the ultrafast saturable absorption of graphene has recently been studied intensively. However, there is a large discrepancy in the reported saturation intensity of graphene; and an explicit relation between the saturation intensity and the operated laser wavelength, number of graphene layers, as well as the substrates is still lacking. In this thesis, we focused to study the spectral dependence of saturation intensity in graphene in addition to the effects of graphene layer numbers and substrates on the saturation.

In Chapter 2, the ultrafast carrier dynamics in graphene associated with the cooling and recombination of photoexcited carriers is explicated. This photodynamics is then applied to develop a mathematical model for quantitative explanations on the saturable absorption in graphene due to Pauli blocking effects. Our consideration is based on a set of assumptions about the carrier relaxation processes. Firstly, the linear energy dispersion relation and interlayer uncoupled multilayer graphene are considered. Secondly, an independent excited electron temperature evolution is assumed for different electron densities and different wavelengths. Thirdly, time-averaging

approximations are taken for photoexcited carrier density and photoexcited electron temperature.

In Chapter 3, saturable absorption in epitaxial graphene was experimentally determined by conducting Z-scan measurements on the monolayer, bilayer and six-layer graphene samples. The nonlinear signal is found to increase linearly as the number of graphene layer increases, which indicates that the modulation depth can be enhanced by increasing the stacking of graphene layers. Moreover, the spectral dependence of saturable absorption of graphene was systematically studied by extending Z-scan measurements from 780 nm to the spectral range of 900 nm to 1100 nm with femtosecond laser pulses. It was demonstrated that the saturation intensity of graphene is sensitively dependent on the operating wavelength, which reduces from ~5 GW/cm^2 to 1.5 GW/cm^2 as the operating wavelength increasing from 900 nm to 1100 nm.

Systematically theoretical investigation on the saturable absorption of an intrinsic graphene under ultrafast excitation was presented in Chapter 4. The saturation intensity of graphene shows little dependence on its thickness, while the saturation depth is proportional to the number of layers of graphene. Moreover, the graphene placed on a substrate with higher refractive index (n_2) saturates at higher intensity. It is also shown that the saturation depth of the graphene sample decreases as n_2 increases. Our mathematical model was validated by a comparison with the experimental measurements of saturable absorption of epitaxial graphene in the spectral range from

780 nm to 1100 nm. The spectral conditions of saturation of absorption were found in the visible-near infrared spectral regions, revealing that the saturation intensity of graphene decrease as the light wavelength increases. Different from other saturable absorbers based on bulk materials and heterostructures, our study exhibits a broadband response of graphene as a saturable absorber. It is concluded that graphene performs superiorly as a saturable absorber due to its ultrafast recovery time, broadband response, large modulation depth and low loss of scattering.

LIST OF TABLES

LIST OF FIGURES

Chapter 1

Introduction

Graphene is a two-dimensional carbon-based honeycomb lattice structure which is the basic building block for all graphitic materials.[1, 2] Although known as a theoretical concept for years [3], graphene was isolated by micromechanical exfoliation of graphite for the first time in 2004 [4, 5]. Since then, graphene has attracted considerable attention in both experimental and theoretical arenas because of its unique and excellent electronic and optical properties [4, 6, 7], which can find technological applications such as photovoltaic devices,[7-10] photodetectors,[11-14] light-emitting devices,[15-19] optical limiters,[20-24] and saturable absorbers [25-33]. Despite the efforts in graphene research, many fundamental properties of graphene have not been fully understood yet, and saturable absorption is one of them. Saturable absorption is one of the nonlinear optical phenomena in which the optical absorption of a material decreases as light is intensified; and it can be utilized for generation of short laser pulses. In this thesis, we report our attempt to develop a quantitative understanding on the relationship between optical absorption of graphene and light intensity.

In this Chapter, we provide the reader with an overview on graphene and aims of our research. It is organized as follows. Section 1.1, a general introduction is given

about the electronic and optical properties, fabrication techniques and applications of graphene. In Section 1.2, a literature review of recent advances in mode-locking techniques is presented. In Section 1.3, a variety of well-known saturable absorbers, in particular graphene-based saturable absorbers, are elaborated. Subsequently, the motivation for the research project reported in this thesis is given and the objective of the thesis is defined in Section 1.4.

1.1 Introduction of Graphene

Graphene has a peculiar zero bandgap linear energy-momentum dispersion relation for both electrons and holes, and thus behaves as massless Dirac fermions [1-3]. The conduction and valence bands touch each other at K points [3] in the Brillouin zone, and in the vicinity of these points following the relationship $E = \hbar v_F k$ [7, 34] (as depicted schematically in Figure 1.1), where k is the momentum measured relatively to the Dirac points and v_F is the Fermi velocity of around 10^6 m s^{-1}. This remarkable band structure can be analytically calculated in the tight binding approximation.[3] For a single layer graphene, the symmetry group leads to a degeneracy of the π bands at the K point. The Fermi level intersects the π band at the K point, leading to a vanished density of states (DOS) at E_F but sharp rises in the DOS above and below E_F.

This peculiar electronic structure of graphene gives rise to high mobility of electrons in graphene and near-ballistic transport at room temperature, making it a

favorable candidate for high speed nanoelectronics, such as field-effect transistors [35-38], p-n junction diodes and transistors [9, 39-42], and terahertz oscillators [43].

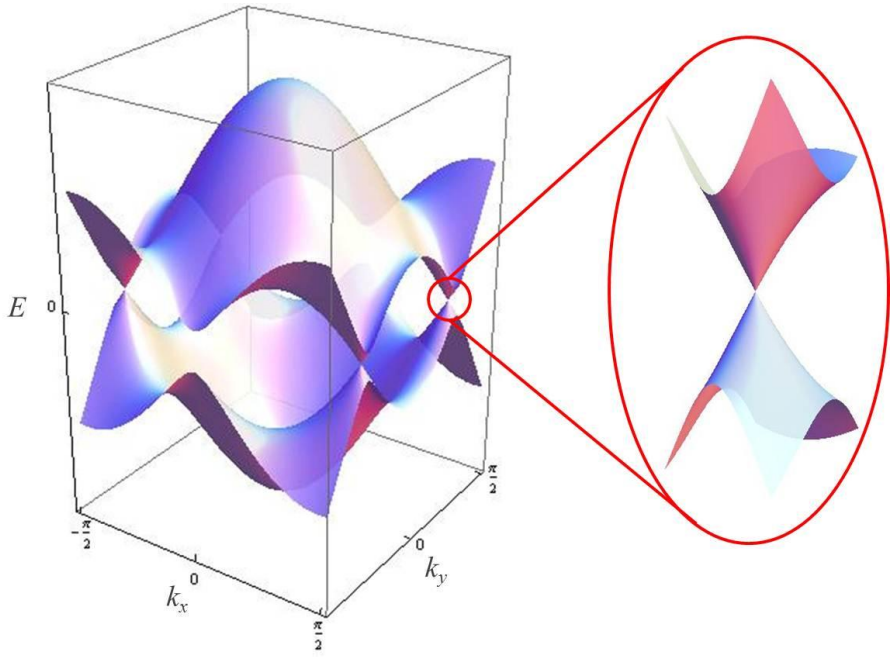

Figure 1.1 Schematic diagram of electronic dispersion in the honeycomb lattice of graphene.

Graphene also reveals remarkable optical properties, such as the universal linear optical absorption of 2.3% which can be expressed in terms of the fine structure constant [6, 44], and it's optical visibility despite being only single atomic thick. Saturable absorption in graphene is observed as a result of state-filling effects induced by interband absorption [25, 26, 33, 45, 46]. Because of the gapless linear dispersion, graphene can possibly be used in broadband applications. These properties make graphene a promising

photonic and optoelectronic material.

Usually, graphene can be classified according to their different layer thicknesses, *i.e*. monolayer graphene(MLG), bilayer graphene(BLG), and few(3-10) layer graphene (FLG), noting that the electronic structure and many properties of graphene evolve to those of graphite by approximately 10 layers [2, 47].

Graphene was firstly produced in 2004, by peeling it off from highly oriented pyrolytic graphite using adhesive tapes in a Manchester group [4]. Such exfoliation method still produces the best samples in terms of defects, purity, mobility and optoelectronic properties [7]. Besides, it has been optimized to produce MLG of up to millimeters in size with high structural and electronic qualities [7]. However, this approach still has several limitations in the widespread applications, such as inefficiency, low throughput, small scale, and uncontrollability etc.

Several other approaches for graphene fabrication have been developed to provide graphene with large scale and quantity for mass applications. The most commonly used methods include epitaxial growth on silicon carbide (SiC) [48-55], chemical vapor deposition (CVD) methods [10, 56-59], and liquid phase exfoliation (LPE) [26, 33, 60-66].

Epitaxial growth of graphene, from a few monolayers to several (>50) layers, by thermal decomposition of SiC surface in ultrahigh vacuum system at high temperatures has been explored by a Georgia group in 2004 [48, 49]. High temperature annealing of SiC leads to the decomposition of SiC and desorption of Si from the surface. The

accumulation of carbon atoms forms a carbon-rich buffer layer, on top of which, MLG, BLG or FLG is formed, depending on time and other conditions.[51, 53, 55] Graphene multilayers grown by this technique have been indicated to have electronic and phononic properties different from that of bulk graphite, but similar to those of graphene monolayers obtained by micromechanical exfoliation techniques [48, 49, 67, 68] This observed difference indicates that the electrons and phonons in different layers of the epitaxial graphene are uncoupled.[69] From a viewpoint of large scale device fabrication and application, the graphene/SiC structure is favored over CVD or exfoliation methods, due to higher reproducibility, better thermal conductivity of SiC substrates and easier manipulation of the samples.

CVD offers an alternative approach for producing large quantities of graphene in a relatively short time. MLG and FLG can now be produced on various substrates by feeding hydrocarbons at a suitable temperature [56, 59, 70-73]. Due to the development of CVD method, large area graphene samples of over 60 cm can be synthesized and transferred to substrates suitable for applications [73]. However, we need to note that most as-grown CVD graphene samples are multilayered. Even if the Raman spectrum of them seems similar [59, 74] to that of ideal MLG [75], this is just an indication of electronic decoupling of the layers, not definite proof of MLG growth [7].

LPE consists of chemical wet dispersion followed by ultrasonication, in both aqueous [66] and non-aqueous solvents [60]. Up to ~70% MLG can be achieved by hundreds

of hours of mild sonication in water with sodium deoxycholate followed by sedimentation-based ultracentrifugation.[76]. The size of graphene synthesized by this method is around few micrometers due to long time sonication. LPE offers advantages of scalability and has no requirement for expensive growth substrates. Moreover, it is an ideal method to produce films and composites.[7]

1.2 Mode-locking technology

Over the past few years, progress in research on ultrafast lasers continues to expand laser applications in not only scientific research but also technology, which has profound impact on the way we live and work. Most applications can be classified into four categories which benefit from different properties of ultrashort laser pulses. First of all, in the time domain, the ultrashort pulse provides excellent high time resolution for characterization of ultrafast physical processes; second, the relatively high peak power and peak intensity at low average power is crucial to reduce thermal effects in material processing; third, the high spatial resolution, which is given by the pulse duration multiplied by the speed of light, makes ultrashort pulses useful for some microscopy and imaging applications; and fourth, the broad coherent spectrum can be filtered to obtain different pulse sequences and be important for optical communications as well as other applications.[77]

Mode-locking is a key technique in optics which was introduced in the mid-1960s to generate laser pulses shorter than 10^{-9} s [78-82]. The demonstration of mode-locking opened up a new era of a novel class of laser systems which is now known as ultrashort pulse or ultrafast lasers. Since then, impressive progress has been achieved in the development of mode-locking technologies, and femtosecond (fs, 10^{-15} s) light pulses have successfully been generated from those mode-locked lasers [77, 83, 84].

There are mainly two techniques for achieving mode-locking, *i.e.* active mode-locking and passive mode-locking. Active mode-locking is one of the first demonstrated and conceptually simplest methods; however it requires external modulation as well as external energy consumption and suffers from ineffectiveness for very short pulses. These drawbacks can be overcome by using passive scheme. Therefore, different schemes of passive mode-locking have been explored, such as additive pulse mode-locking [85], Kerr lens mode-locking [86] and saturable absorber mode-locking [87].

Among these techniques, passive mode-locking using a saturable absorber is well-established as the most effective alternative. It simplifies the mode-locking procedures and allows for more flexibility in the specific laser cavity design. Currently, the dominant technology is based on semiconductor saturable absorber mirrors (SESAMs) [83, 88]. However, SESAMs normally require complex fabrication and packaging issues as well as narrow tunable range. A simple and cost-effective alternative is to use Single-Walled Carbon Nanotubes (SWNTs), in which the band gap

and thus the operating wavelength are controlled by the tube diameter and chiral vector.[89, 90] Therefore, broadband tunability is realizable by using SWNTs with a wide diameter distribution. However, when operated at a particular wavelength, SWNTs which are not in resonance would cause unwanted losses. The more recently developed material, graphene, offers an ideal solution to an ultra-broadband, fast saturable absorber due to its unique gapless linear dispersion relation of Dirac electrons, the ultrafast carrier dynamics, combined with its low saturation intensity and large modulation depth.[7]

1.3 Saturable absorber and graphene based saturable absorber (GSA)

In this Section, the basic concept of a saturable absorber is outlined, the key properties of a graphene saturable absorber (GSA) are summarized, and the reports on GSA mode-locking are reviewed.

1.3.1 Basic concept of a saturable absorber

A saturable absorber is a material in which the absorption of light decreases nonlinearly with increasing incident light intensity. To explain this phenomenon, ones often employ simple qualitative arguments based on a two-level electronic model, for which saturable absorption is symmetrical to gain saturation. As shown in Figure 1.2, electrons in the ground state of the lower energy level can absorb photons when their

photon energy is the same as the difference between the two levels, and be excited to higher energy level if there is no electron at the upper level. Under strong photoexcitation, the absorption can be significantly decreased due to the fact that less electrons at the lower level and less un-occupied states at the upper level. As a result, the absorption is saturated and the light can be transmitted through the absorber without being absorbed.

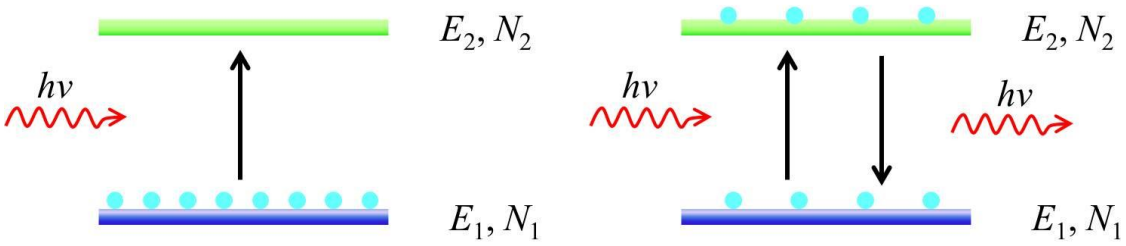

Figure 1.2 Physical mechanism of a saturable absorber based on a two-level model.

Based on this simple framework, a hyperbolic dependence of the absorption coefficient on the incident light intensity is a satisfactory approximation:

$$\alpha(I) = \frac{\alpha_0}{(1 + I / I_s)} \tag{1.1}$$

where α_0 is the low-intensity (or sometimes called as linear) absorption coefficient and I_s is the saturation intensity, a phenomenological parameter, at which α decreases to a half of its value at low incident light intensity (*i.e.* α (I_s) = α_0 / 2). The saturation intensity

is an important parameter in determining the performance of a saturable absorber. This nonlinear relationship between the absorption coefficient and the incident light intensity is shown in Figure 1.3.

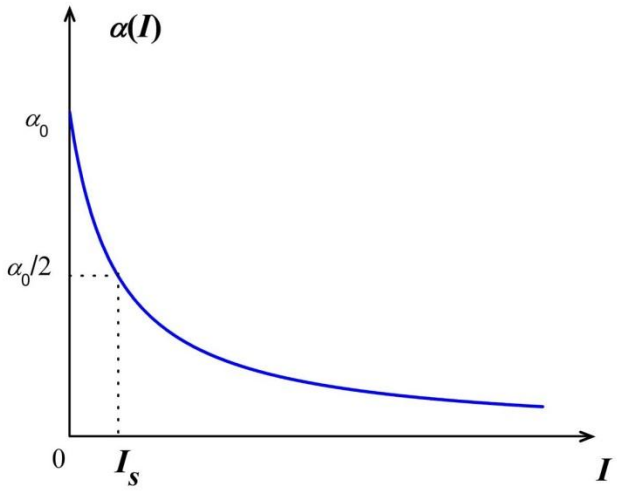

Figure 1.3 Simple hyperbolic model of the absorption coefficient of a two-level system as a function of the incident light intensity. When the intensity reaches the saturation value I_s the low-intensity absorption α_0 is reduced by a factor of two.

As the light intensity increases, the absorption coefficient of the saturable absorber decreases, which translates for the transmitted intensity approximately as

$$T(I_i) = \frac{I_t}{I_i} = \exp[\frac{-\alpha_0 L}{1 + I_i / I_s}] \tag{1.2}$$

Equation (1.2) is obtained by replacing the constant low-intensity absorption coefficient in the Beer-Lambert law, $I_t = I_i \exp(-\alpha_0 L)$ by Equation (1.1). I_i is the intensity incident on the absorbing medium of length L, and I_t is the transmitted light intensity. It should

be pointed out that Equation (1.2) is an approximation. The exact solution should be obtained from the following differential equation:

$$\frac{dI(z)}{dz} = -\frac{\alpha_0}{1+\frac{I(z)}{I_s}} I(z) \tag{1.3}$$

where z is the distance within the medium. Figure 1.4 shows the exact solution for the transmission as a function of the incident light intensity.

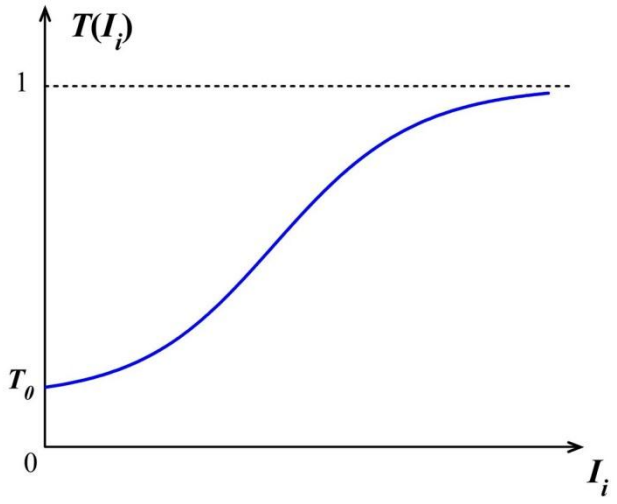

Figure 1.4 Numerical simulation of transmission as a function of incoming light intensity in a two-level electronic system.

As can be seen in Figure 1.4, at low intensity ($I_i << I_s$), $T \approx T_0$. As I_i increases to be comparable to I_s, the population of the upper level involved in absorption increases, and the population of the lower level decreases, leading to a nonlinear behavior of $T(I_i)$. As I_i is further increased to higher intensity, the absorber is saturated totally and becomes

transparent ($T = 1$).

Saturable absorber can be used in passive mode-locking for short pulse generation because of the above-mentioned nonlinear transmission. The schematic setup of passive mode-locking by a saturable absorber is shown in Figure 1.5 [91]. Typically, a mode-locked laser is composed of a gain medium (or called laser amplifier) within an optical cavity- a pair of mirrors on either end of the gain medium. Light propagates back and forth between the mirrors, passing through the gain medium and being amplified each time by stimulated emission. Normally, one of the two mirrors, the output coupler, is partially transparent to allow a portion of the laser light to escapes through this mirror. In addition, a saturable absorber is placed inside the laser cavity that leads to a passive mode-locking of the laser. The mode-locking process in the time domain can be described as follows [92]. In a multimode laser, the output is the incoherent interference of random modes, resulting in the temporal fluctuations of light intensity inside the cavity (Figure 1.6(a)). Due to the presence of the saturable absorber, some strong noise spikes experience less loss compared to the weak noises when passing through the absorber. The most energetic noise spike suppresses all the other background noises by experiencing the least amount of saturable absorption and saturating the gain to a level where the other background noises can only experience net losses in each round-trip (Figure 1.6(b)). After a few round-trips, one dominant spike contains a significant part of the circulating energy because of the lowest absorption, while other background noises decay quickly (Figure 1.6(c)).

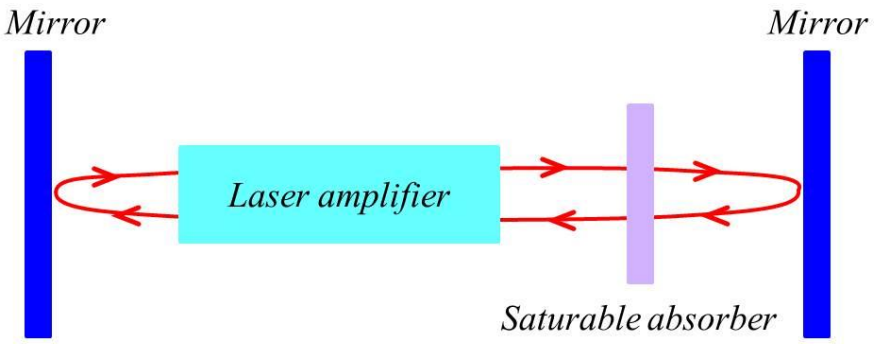

Figure 1.5 Schematic setup for passive mode-locking by a saturable absorber.

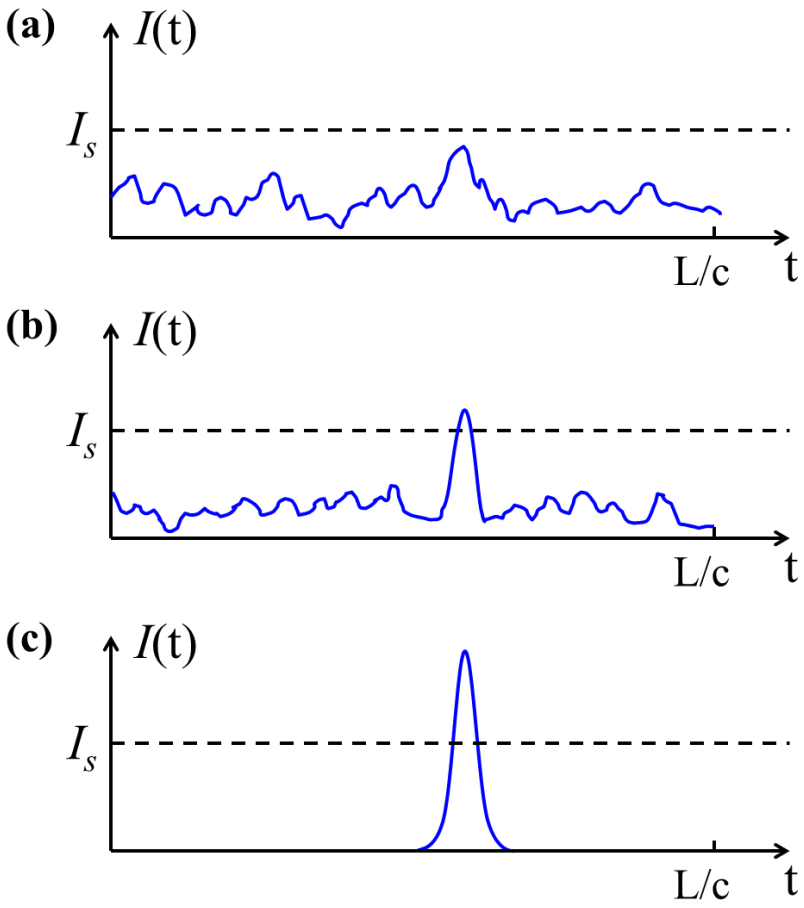

Figure 1.6 Evolution of a short pulse during the mode-locking by a saturable absorber. (a) Low intensity regime ($I_i < I_s$), with random fluctuations; (b) $I_i \approx I_s$, the onset of the discrimination of the weak peaks; and (c) final energy distribution.[92] Here, L is the cavity length and c is the speed of light.

Saturable absorbers can be split into two categories depending on the recovery time of the absorber. Fast saturable absorbers have a recovery time shorter than the pulse duration. As it has instantaneous response under light illumination, the wings of the pulse which have relatively lower intensities would experience more absorption than the peak of the pulse [93]. Figure 1.7 shows a simulation of the effect of such a saturable absorber on a Gaussian pulse. It shows that the pulse undergoes a temporal narrowing when propagation through a fast absorber.

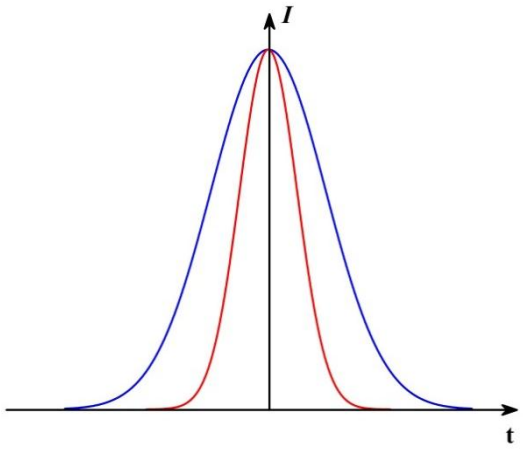

Figure 1.7 Illustration of the pulse modification by a fast saturable absorber on a Gaussian light pulse. The modified pulse (red) has been normalized to the original one (blue) in order to make clear the narrowing of the pulsation.[93]

On the contrary, a slow saturable absorber recovers in a longer time scale compared to the pulse duration. It is normally bleached by the strong absorption of the leading part of the pulse and the trailing part cannot experience efficient absorption. Therefore, only the pulse front gets shortened, resulting in an asymmetric pulse shape, as can be seen in

Figure 1.8 [93]. For ultrashort light pulses (picoseconds or sub-picoseconds), most saturable absorbers are slow ones since their recovery times are usually nanoseconds to picoseconds.

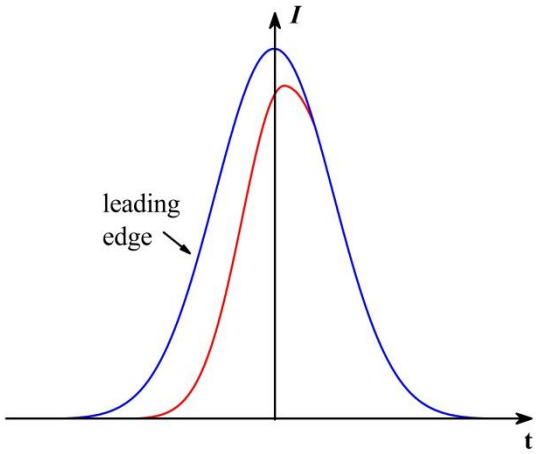

Figure 1.8 Illustration of the pulse modification by a slow saturable absorber on a Gaussian light pulse. Only the pulse front gets shortened.[93]

To achieve the effective pulse shaping, the saturable absorber should recover to its initial state in a short time (a few ps to a few tens of ps). However, the absorption recovery time of most semiconductor saturable absorbers normally falls in the nanosecond range [93]. Graphene, which has a very short recovery time, (a few ps [68]) has been employed as a promising candidate of passive mode-locking. Compared with the traditional SESAMs, graphene is more favorable as saturable absorbers, since it reveals broadband operation wavelength, ultrashort recovery time, low saturation intensity, low insertion loss, large modulation depth and low costs.[25]

1.3.2 Key properties of a graphene saturable absorber (GSA)

Various strategies have been proposed to integrate GSAs in laser cavities for ultrashort pulse generation. The most common one in mode-locked ultrafast fiber lasers is realized by sandwiching a GSA between two fiber connectors with a fiber adaptor, as shown schematically in Figure 1.9 [25, 26]. Graphene on a side-polished fiber has also been reported, targeting at high power generation by evanescent field interaction [29]. A graphene saturable absorber mirror (GSAM) used for ultrafast pulse solid-state laser has been fabricated by depositing high-quality graphene sheets on high-reflection mirror, as indicated in Figure 1.10 [33].

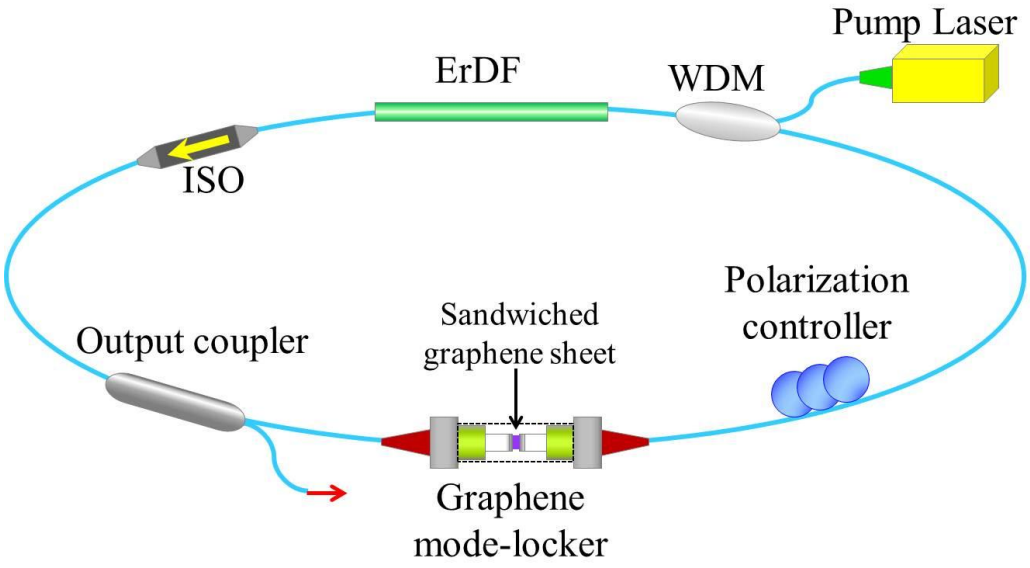

Figure 1.9 Schematic diagram of the graphene mode-locked ultrafast laser: a GSA is sandwiched between two fiber connectors. An erbium-doped fiber (ErDF) is the gain medium, pumped by a laser diode with a wavelength-division multiplexer (WDM). An isolator (ISO) maintains unidirectional operation, and a polarization controller (PC) optimizes mode-locking.[25, 26]

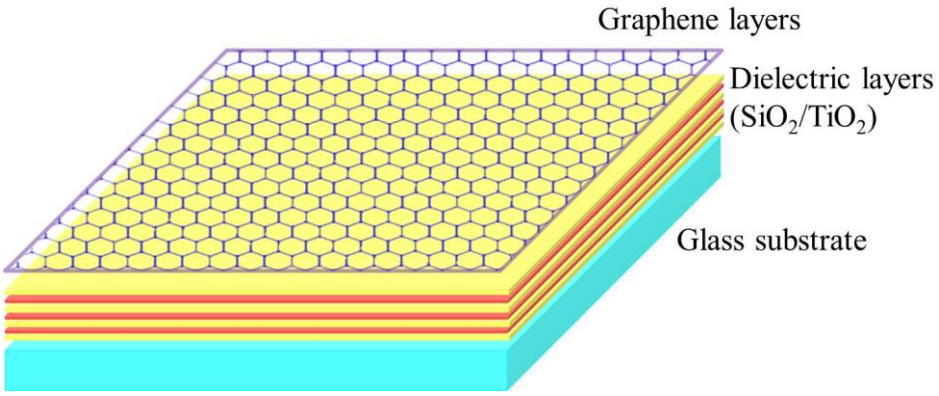

Figure 1.10 Schematic structure of the graphene saturable absorber mirror used in ultrafast pulse solid-state laser.[33]

For the GSA used in the solid-state lasers, graphene is deposited on a mirror which is fabricated by stacking pairs of alternating layers with a high refractive indices contrast (*e.g.* SiO_2/TiO_2) on a glass substrate (see Figure 1.10). A typical nonlinear reflectivity property of such GSAM is shown in Figure 1.11. As can be seen, when the incident light intensity increases, the reflectance increases nonlinearly, and saturates at high intensities. Then the reflectance difference between the low-intensity and the saturated values (ΔR) is called the optical modulation depth of a GSAM, which is an important parameter for a GSAM.

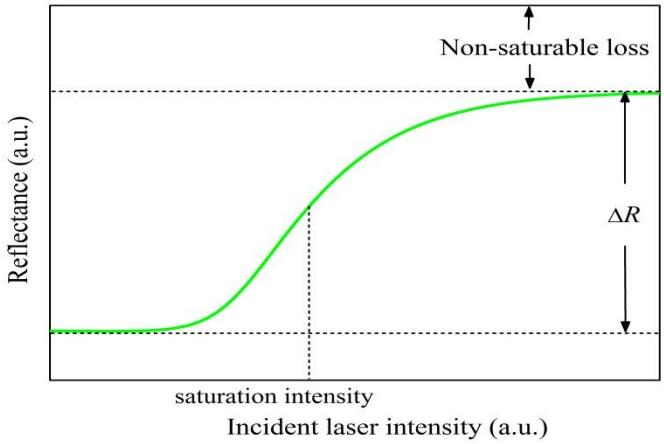

Figure 1.11 Schematic diagram of nonlinear reflectance from a GSAM.

It has been shown that for traditional SESAMs, the width of a mode-locked pulse (τ_p) is inversely proportional to the modulation depth:

$$\tau_p \propto (\Delta R)^{-\beta} \qquad (\beta > 0), \tag{1.4}$$

where β is a numerical factor [94]. It indicates that the larger the modulation depth is, the shorter the pulses are. Considering similar expression in GSAM, in order to generate shorter laser pulses, the modulation depth should be larger.

Another important parameter for a GSAM is the saturation intensity I_s. As shown in Figure 1.11, the saturation intensity I_s is the intensity required to increase the reflectance by half of ΔR.

If a GSA is sandwiched between two fiber connectors, without a mirror, its nonlinear property can then be characterized through the nonlinear transmittance

behavior. As shown in Figure 1.12, the modulation depth of a GSA is now the transmittance difference (ΔT) between the low-intensity and saturated values.

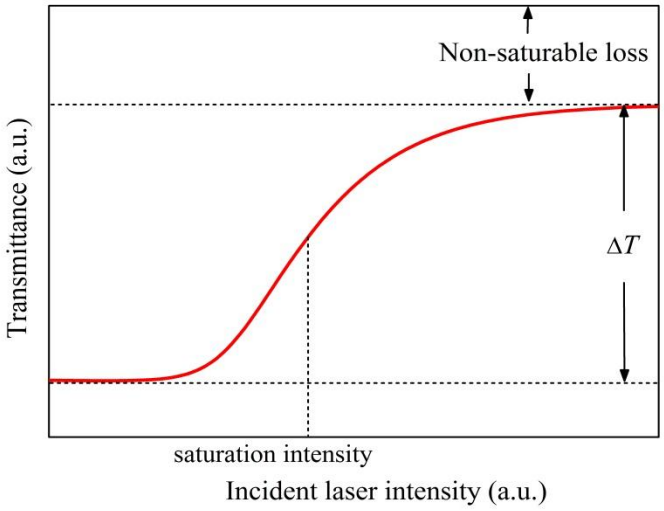

Figure 1.12 Schematic diagram of nonlinear transmittance from a GSA.

1.3.3 Literature review on the passive mode-locking by saturable absorbers

The initial idea of passive mode-locking by saturable absorbers was demonstrated in semiconductor diode lasers in the early 1980's. [95-97] At this early stage, stable continuous-wave mode-locking by saturable absorbers was believed to be impossibly achieved in solid-state lasers. This is mainly attributed to the small gain cross-section (typically more than 1000 times smaller than dye, diode and colour center lasers) and the long upper state lifetime (typically more than 1000 times longer), which would result in strong tendency for self-Q-switching instabilities [83]. This meant that more research efforts have to devote to the improvement in existing saturable absorbers or the

development of new saturable absorbers and/or designs, which partially explained why it took so long for the first successful demonstration. In 1992, Keller *et al*. demonstrated the first stable self-starting passive mode-locked solid-state laser with a new type of intracavity saturable absorber mirror, the antiresonant Fabry-Perot saturable absorber. This was also the first design of SESAM-based passive mode-locking. Since then, diode-pumped solid-state lasers passively mode-locked by SESAMs gradually become dominant in the area of high performance ultrashort lasers; and many new designs of SESAM have been developed [83, 88, 91].

In 2003, Set *et al.* reported for the first time the saturable absorption property of SWNTs for 1 ps pulses at 1550 nm [98]. Subsequently, they successfully developed mode-locked fiber lasers employing such simple structures as saturable absorbers [99]. Since then, SWNTs or its polymer composites based saturable absorbers (CNTSAs) have been widely adopted as mode-locking elements for ultrashort fiber lasers and solid-state lasers in both ring and linear configurations [89, 90]. Comparing to the complex, costly and environmentally unfriendly fabrication procedures of SESAMs, the CNTSA devices only need a low-cost room-temperature fabrication process. The linear and nonlinear parameters of CNTSAs, e.g. linear transmittance, absorption band and threshold, etc., can be simply engineered by selecting CNTs with appropriate diameters and by varying the thicknesses and concentrations of CNT or CNT–polymer layers. As a reflective device, SESAM can only be used in lasers with a linear cavity and a low damage threshold. Whereas, CNT and CNT–polymer composites have higher damage

thresholds and the flexibility of CNT composites allows designing and fabricating different CNTSA structures to fit the different requirements.

Graphene as a promising alternative of saturable absorber for large energy mode-locking for both ultrashort pulse fiber lasers and solid-state lasers has been investigated extensively since 2009. Table 1.1 summarizes most of the representative studies on the passively mode-locked fiber lasers and solid-state lasers using graphene saturable absorbers. It also shows a performance comparison between graphene mode-locked ultrafast lasers and selected CNT-based devices [68, 69].

As can be seen from Table 1.1, the performance of graphene mode-locked ultrafast lasers has been improved significantly since their first demonstration [25]. The average output power has been increased by three-orders of magnitude from a few mW [25] to 1 W [100]. Different produce strategies (e.g. LPE [26, 28, 31-33, 89, 100-108], CVD [25, 30, 46, 109-119], reduced graphene oxide (RGO) [29, 120-124], micromechanical exfoliation [27, 125-127], epitaxial [128], etc.) have been employed for GSA fabrication. To date, GSAs have been demonstrated for pulse generation at 1 μm [33, 100, 102, 115, 116, 121, 128-130], 1.2 μm [30, 111] and 1.5 μm [25-29, 31, 32, 46, 89, 101-110, 112-114, 117-120, 122-127, 131]. The most common wavelength so far is ~1.5 μm, not because GSAs have any preference for a particular wavelength, but because this is the standard wavelength of optical telecommunications. Widely tunable fiber lasers mode-locked with GSAs have also been reported.[102, 103]

Fiber lasers are attractive due to their efficient heat dissipation and alignment-free

fiber format. GSAs have been successfully used to mode-lock fiber lasers. In this case, the simplest and most economical approach for GSA integration consists in sandwiching the GSA between two fiber connectors (Figure 1.9) [25-28, 31, 89, 101-107, 109, 110, 113-119, 122-127, 131]. Other approaches, such as evanescent-wave based integration have also been reported especially for high-power pulse generation [29, 120]. Sub-200fs ultrafast pulses have been achieved using a stretched-pulse design [104, 105].

Solid-state lasers are typically used for high-power output, as an alternative to fiber lasers. GSAs have also mode-locked solid-state lasers [30, 33, 46, 100, 102, 111, 112, 121]. Large-area (> 1 cm^2) CVD graphene can be transferred on quartz substrates or high-reflectivity mirrors for solid-state laser mode-locking [30, 46, 111, 112]. Cho *et al.* reported 94 fs pulse generation from a GSA mode-locked solid-state laser with 230 mW output power [30]. Another approach for GSA fabrication relies in spin-coating LPE graphene on either quartz substrates [100, 102] or high-reflectivity mirrors [33], which are then inserted into a solid-state cavity for ultrafast pulse generation. With this method, average power up to 1 W was achieved using a solid-state Nd:YVO_4 laser [100]. The output wavelength was ~ 1 μm with output energy ~14nJ [100].

Graphene-based saturable absorber shows promising potential to replace conventional SESAM and CNT as mode-lockers for ultrafast fiber and solid-state lasers because of the good performance, easy fabrication, low cost and wide availability. Comparing with SESAMs, graphene as a saturable absorber for passive mode-locking

has the following advantages: (i) considerable design freedom offered by controlling the number of graphene layers or composite concentrations or by chemical functionalization; (ii) super broadband saturable absorption; (iii) ultrafast saturation recovery time; and (iv) simple and low-cost fabrication[114]. Moreover, graphene provide a remarkable approach to overcome the drawbacks of CNTSAs. For instance, CNTs with a certain diameter only contribute to the saturable absorption of a particular wavelength of light, and CNTs tend to form bundles that turn into scattering sites. Therefore, coexistence of CNTs with different diameters introduces extra non-saturable losses to the mode-locker, making mode-locking difficult to achieve [110].

Table 1.1 Representative works on the graphene-based mode-locked lasers.

Mode-locker		**Laser**	**Performance**						**Year**	**Reference**
Fabrication type	Coupling method	Gain material	λ (nm)	Spectral bandwidth (nm)	Pulse width	Repetition rate (MHz)	Power (mW)	TBP		
CVD	Sandwiching	ErDF	1565	5	756 fs	1.79	2		2009	[25]
CVD	Sandwiching	ErDF	1576	10	415 fs	6.84	50	0.518	2009	[109]
RGO	Sandwiching	ErDF	1590	5	700 fs	6.95	50	0.412	2009	[124]
LPE	Sandwiching	ErDF	1557	-	800 fs	-	-	-	2009	[89]
RGO	Free space	Nd:YAG	1064	0.42	4 ps	88	100	0.44	2010	[121]
LPE	Sandwiching	ErDF	1559	5.24	464 fs	19.9	-	0.3	2010	[26, 101]
RGO	Evanescent field interaction	ErDF	1561	1.96	1.3 ps	6.99	51	-	2010	[29, 120]
FG	Sandwiching	ErDF	1570-1600	-	1.08 ps	6.95	-	0.4	2010	[131]
CVD	Sandwiching	ErDF	1570-1600	3-9	40-140 fs	1.5	3.5	44.3	2010	[110]
CVD	Free space	Cr:forsterite	1237	14	130 fs	75	230	0.36	2010	[111]
LPE	Sandwiching Free space	ErDF Nd:YVO_4	1525-1559 1064	3 0.17	0.9-1.2 ps -	8 75	1 1000	0.3-0.4 -	2010	[102, 103] [100, 102]
CVD	GSAM	Er:Yb:glass	1550	17	260 fs	88	4.5	-	2010	[46, 112]
CVD	Sandwiching	ErDF	1560-1570 1570-1600 1570-1600	4.1 5.7-15.3 3-6	655 fs 240-650fs 70-150 ps	- - -	- - -	0.335 - -	2010	[113]
CVD	Sandwiching	ErDF	1584 1564	7.18 1.5	71 ps 2.1 ps	1.5 10	- -	63.7 0.37	2010	[114]
LPE	Sandwiching	ErDF	1532	-	850 fs	5.27	-	-	2010	[28]
CVD	Sandwiching	YbDF	1070	1.29	580 ps	0.9	0.37	196	2010	[115, 116]

Table 1.1 (*Contd.*)

Mode-locker		Laser		Performance					Year	Reference
Fabrication type	Coupling method	Gain material	λ (nm)	Spectral bandwidth (nm)	Pulse width	Repetition rate (MHz)	Power (mW)	TBP		
LPE	Sandwiching	ErDF	1558	15.6	174 fs	27.4	1.2	0.335	2010	[104, 105]
Exfoliation	Sandwiching	ErDF	1576	0.8	3.2 ps	10.9	3	-	2010	[27, 125]
LPE	Sandwiching	ErDF	1573	0.6	4.3 ps	91.5	-	-	2011	[31, 106]
CVD	Sandwiching	ErDF	1561	5	1.23 ps	2.5	50	-	2011	[117]
LPE	GSAM	Nd:$GdVO_4$	1065	0.58	16 ps	43	360	-	2011	[33]
LTE	GSAM	YbDF	1075	0.12	680 ps	1.04	170	-	2011	[129, 130]
LPE	Sandwiching	ErDF	1560	0.76	16 ns	0.227	15	1499	2011	[107]
CVD	Sandwiching	ErDF	1560	3.88	684 fs	25.38	1.54	-	2011	[118, 119]
Exfoliation	Sandwiching	ErDF	1566	4.92	880 fs	6.22	-	-	2011	[126, 127]
CVD	Free space	Cr:forsterite	1240	20	94 fs	74.65	230	0.37	2011	[30]
RGO	Sandwiching	ErDF	1562	2.1	938 fs	15.2	4.1	-	2011	[122, 123]
LPE	GSAM	ErDF	1565	12.5	190 fs	42.8	0.4	-	2011	[32]
Epitaxial	GSAOC	YbDF	1040	1.2	520 ps	1.05	20	-	2011	[128]
LPE	GSAM	ErYbDF	1562	3.2	880 fs	9670	2.5	-	2011	[108]
CNT	-	-	1-2 μm	0.15-200 nm	68 fs- 2 ns	177 kHz - 17 GHz	1.6 W	-	2003-2011	[7, 89, 90]

TBP, Time-bandwidth product; LTE, Low-temperature exfoliation; GSAOC, graphene saturable absorber laser output coupler.

1.4 Objectives and the synopsis of the thesis

Given mode-locking applications mentioned in Section 1.2 and 1.3, there is a demand for systematic investigation on the saturable absorption of graphene, in particular, for its spectral dependence. To date, many research groups [25, 26, 45, 118, 126, 132, 133], including our group [134], have published their observations on the saturable absorption of graphene. However, there is a large discrepancy in the reports of I_s of graphene which might be due to the different synthesis methods and different experimental conditions. In addition, theoretical understanding is lacking behind the above-mentioned advances in experiments. A photodynamic model is first presented by Dawlty *et al*. in 2008. Since then, there have been several reports on the theory. The detailed reviews on these reported theoretical models will be presented in Chapter 2. These theories failed to give an explicit relation between the saturation intensity and the operated laser wavelength. Such a relation is of paramount importance to the designing or engineering of graphene for mode-locking. Therefore, a systematic study on the saturable absorption of graphene at various wavelengths is desired. The study will offer a deep understanding of the mechanisms of saturation in graphene and will facilitate the application of GSA in a wide spectrum range.

The main aim of the research work reported in this thesis is to establish a mathematical approximation model based on the photodynamic model for quantitative explanations of the spectral dependence of saturation intensity in graphene and to theoretically investigate the effects of numbers of graphene layers on saturation

intensities as well as the dependence of saturable absorption on the substrates. The thesis is organized as follows.

In Chapter 2, we start with experimental observations on the ultrafast carrier dynamics in graphene. Based on the above-discussed experimental evidence, existing theoretical understanding is critically reviewed on saturable absorption of graphene. Our mathematical considerations are then introduced and a mathematical model is established for the saturable absorption of graphene. In Chapter 3, experimental measurements of epitaxial graphene's saturation intensity in the spectral range from 700 nm to 1100 nm are presented. In Chapter 4, we validate our mathematical model by comparison with the above-mentioned experiments. Effects of the thickness of graphene on saturation intensities and the dependence of saturable absorption on the substrates are investigated. The dispersion (or spectral dependence) of saturation intensity of graphene and the shortcoming of the model is also discussed. A final conclusion and suggestions for future work are summarized in Chapter 5.

References:

1. Neto, A. C.; Guinea, F.; Peres, N. M. R., Drawing conclusions from graphene. *Physics World* **2006**, 19, 33.

2. Geim, A. K.; Novoselov, K. S., The rise of graphene. *Nat. Mater.* **2007**, 6, 183.

3. Wallace, P. R., The band theory of graphite. *Phys. Rev.* **1947**, 71, 622.

4. Novoselov, K. S.; Geim, A. K.; Morozov, S. V.; Jiang, D.; Zhang, Y.; Dubonos, S. V.; Grigorieva, I. V.; Firsov, A. A., Electric field effect in atomically thin carbon films. *Science* **2004**, 306, 666.

5. Novoselov, K. S.; Jiang, D.; Schedin, F.; Booth, T. J.; Khotkevich, V. V.; Morozov, S. V.; Geim, A. K., Two-dimensional atomic crystals. *Proc. Natl. Acad. Sci. USA* **2005**, 102, 10451.

6. Nair, R. R.; Blake, P.; Grigorenko, A. N.; Novoselov, K. S.; Booth, T. J.; Stauber, T.; Peres, N. M. R.; Geim, A. K., Fine structure constant defines visual transparency of graphene. *Science* **2008**, 320, 1308.

7. Bonaccorso, F.; Sun, Z.; Hasan, T.; Ferrari, A. C., Graphene photonics and optoelectronics. *Nat. Photonics* **2010**, 4, 611.

8. Wang, X.; Zhi, L.; Mullen, K., Transparent, conductive graphene electrodes for dye-sensitized solar cells. *Nano Lett.* **2007**, 8, 323.

9. Singh, R. S.; Nalla, V.; Chen, W.; Wee, A. T. S.; Ji, W., Laser patterning of epitaxial graphene for schottky junction photodetectors. *Acs Nano* **2011**, 5, 5969.

10. De Arco, L. G.; Zhang, Y.; Schlenker, C. W.; Ryu, K.; Thompson, M. E.; Zhou, C. W., Continuous, highly flexible, and transparent graphene films by chemical vapor deposition for organic photovoltaics. *Acs Nano* **2010**, 4, 2865.

11. Xia, F. N.; Mueller, T.; Lin, Y. M.; Valdes-Garcia, A.; Avouris, P., Ultrafast graphene photodetector. *Nat. Nanotechnol.* **2009**, 4, 839.

12. Lin, C. C.; Wang, D. Y.; Tu, K. H.; Jiang, Y. T.; Hsieh, M. H.; Chen, C. C.; Chen, C. W., Enhanced infrared light harvesting of inorganic nanocrystal photovoltaic and photodetector on graphene electrode. *Appl. Phys. Lett.* **2011**, 98, 263509

13. Mueller, T.; Xia, F. N. A.; Avouris, P., Graphene photodetectors for high-speed optical communications. *Nat. Photonics* **2010**, 4, 297.

14. Urich, A.; Unterrainer, K.; Mueller, T., Intrinsic response time of graphene photodetectors. *Nano Lett.* **2011**, 11, 2804.

15. Lee, C. H.; Kim, Y. J.; Hong, Y. J.; Jeon, S. R.; Bae, S.; Hong, B. H.; Yi, G. C., Flexible inorganic nanostructure light-emitting diodes fabricated on graphene films. *Adv. Mater.* **2011**, 23, 4614.

16. Seo, T. H.; Lee, K. J.; Park, A. H.; Hong, C. H.; Suh, E. K.; Chae, S. J.; Lee, Y. H.; Cuong, T. V.; Pham, V. H.; Chung, J. S.; Kim, E. J.; Jeon, S. R., Enhanced light output power of near UV light emitting diodes with graphene/indium tin oxide nanodot nodes for transparent and current spreading electrode. *Opt. Express* **2011**, 19, 23111.

17. Matyba, P.; Yamaguchi, H.; Chhowalla, M.; Robinson, N. D.; Edman, L., Flexible and metal-free light-emitting electrochemical cells based on graphene and PEDOT-PSS as the electrode materials. *Acs Nano* **2011**, 5, 574.

18. Matyba, P.; Yamaguchi, H.; Eda, G.; Chhowalla, M.; Edman, L.; Robinson, N. D., Graphene and mobile ions: The key to all-plastic, solution-processed light-emitting devices. *Acs Nano* **2010**, 4, 637.

19. Sun, T.; Wang, Z. L.; Shi, Z. J.; Ran, G. Z.; Xu, W. J.; Wang, Z. Y.; Li, Y. Z.; Dai, L.; Qin, G. G., Multilayered graphene used as anode of organic light emitting devices. *Appl. Phys. Lett.* **2011**, 98, 059901.

20. Wang, J.; Hernandez, Y.; Lotya, M.; Coleman, J. N.; Blau, W. J., Broadband nonlinear optical response of graphene dispersions. *Adv. Mater.* **2009**, 21, 2430.

21. Feng, M.; Zhan, H. B.; Chen, Y., Nonlinear optical and optical limiting properties of graphene families. *Appl. Phys. Lett.* **2010**, 96.

22. Xu, Y. F.; Liu, Z. B.; Zhang, X. L.; Wang, Y.; Tian, J. G.; Huang, Y.; Ma, Y. F.; Zhang, X. Y.; Chen, Y. S., A graphene hybrid material covalently functionalized with porphyrin: Synthesis and optical limiting property. *Adv. Mater.* **2009**, 21, 1275.

23. Midya, A.; Mamidala, V.; Yang, J. X.; Ang, P. K. L.; Chen, Z. K.; Ji, W.; Loh, K. P., Synthesis and superior optical-limiting properties of fluorene-thiophene-benzothiadazole polymer-functionalized graphene sheets. *Small* **2010**, 6, 2292.

24. Liu, Y. S.; Zhou, J. Y.; Zhang, X. L.; Liu, Z. B.; Wan, X. J.; Tian, J. G.; Wang, T.; Chen, Y. S., Synthesis, characterization and optical limiting property of covalently oligothiophene-functionalized graphene material. *Carbon* **2009**, 47, 3113.

25. Bao, Q. L.; Zhang, H.; Wang, Y.; Ni, Z. H.; Yan, Y. L.; Shen, Z. X.; Loh, K. P.; Tang, D. Y., Atomic-layer graphene as a saturable absorber for ultrafast pulsed lasers. *Adv. Funct. Mater.* **2009**, 19, 3077.

26. Sun, Z. P.; Hasan, T.; Torrisi, F.; Popa, D.; Privitera, G.; Wang, F. Q.; Bonaccorso, F.; Basko, D. M.; Ferrari, A. C., Graphene mode-locked ultrafast laser. *Acs Nano* **2010**, 4, 803.

27. Chang, Y. M.; Kim, H.; Lee, J. H.; Song, Y.-W., Multilayered graphene efficiently formed by mechanical exfoliation for nonlinear saturable absorbers in fiber mode-locked lasers. *Appl. Phys. Lett.* **2010**, 97, 211102.

28. Martinez, A.; Fuse, K.; Xu, B.; Yamashita, S., Optical deposition of graphene and carbon nanotubes in a fiber ferrule for passive modelocked lasing. *Opt. Express* **2010**,

18, 23054.

29. Song, Y. W.; Jang, S. Y.; Han, W. S.; Bae, M. K., Graphene mode-lockers for fiber lasers functioned with evanescent field interaction. *Appl. Phys. Lett.* **2010**, 96, 051122.

30. Cho, W. B.; Kim, J. W.; Lee, H. W.; Bae, S.; Hong, B. H.; Choi, S. Y.; Baek, I. H.; Kim, K.; Yeom, D. I.; Rotermund, F., High-quality, large-area monolayer graphene for efficient bulk laser mode-locking near 1.25 mu m. *Opt. Lett.* **2011**, 36, 4089.

31. Kim, H.; Cho, J.; Jang, S.-Y.; Song, Y.-W.; Chang, Y. M.; Lee, J. H., Deformation-immunized optical deposition of graphene for ultrafast pulsed lasers. *Appl. Phys. Lett.* **2011**, 98, 021104.

32. Cunning, B. V.; Brown, C. L.; Kielpinski, D., Low-loss flake-graphene saturable absorber mirror for laser mode-locking at sub-200-fs pulse duration. *Appl. Phys. Lett.* **2011**, 99, 261109.

33. Xu, J. L.; Li, X. L.; Wu, Y. Z.; Hao, X. P.; He, J. L.; Yang, K. J., Graphene saturable absorber mirror for ultra-fast-pulse solid-state laser. *Opt. Lett.* **2011**, 36, 1948.

34. Castro Neto, A. H.; Guinea, F.; Peres, N. M. R.; Novoselov, K. S.; Geim, A. K., The electronic properties of graphene. *Rev. Mod. Phys* **2009**, 81, 109.

35. Lin, Y.-M.; Dimitrakopoulos, C.; Jenkins, K. A.; Farmer, D. B.; Chiu, H.-Y.; Grill, A.; Avouris, P., 100-GHz transistors from wafer-scale epitaxial graphene. *Science* **2010**, 327, 662.

36. Schwierz, F., Graphene transistors. *Nat. Nanotechnol.* **2010**, 5, 487.

37. Lemme, M. C.; Echtermeyer, T. J.; Baus, M.; Kurz, H., A graphene field-effect device. *IEEE Electron Device Lett.* **2007**, 28, 282.

38. Ryzhii, V.; Ryzhii, M.; Satou, A.; Otsuji, T.; Kirova, N., Device model for graphene bilayer field-effect transistor. *J. Appl. Phys.* **2009**, 105.

39. Williams, J. R.; DiCarlo, L.; Marcus, C. M., Quantum hall effect in a gate-controlled p-n junction of graphene. *Science* **2007**, 317, 638.

40. Ozyilmaz, B.; Jarillo-Herrero, P.; Efetov, D.; Abanin, D. A.; Levitov, L. S.; Kim, P., Electronic transport and quantum hall effect in bipolar graphene p-n-p junctions. *Phys. Rev. Lett.* **2007**, 99, 166804.

41. Cheng, H. C.; Shiue, R. J.; Tsai, C. C.; Wang, W. H.; Chen, Y. T., High-quality graphene p-n junctions via resist-free fabrication and solution-based noncovalent functionalization. *Acs Nano* **2011**, 5, 2051.

42. Cheianov, V. V.; Fal'ko, V.; Altshuler, B. L., The focusing of electron flow and a veselago lens in graphene p-n junctions. *Science* **2007**, 315, 1252.

43. Rana, F., Graphene terahertz plasmon oscillators. *IEEE Trans. Nanotechnol.* **2008**, 7, 91.

44. Mak, K. F.; Sfeir, M. Y.; Wu, Y.; Lui, C. H.; Misewich, J. A.; Heinz, T. F., Measurement of the optical conductivity of graphene. *Phys. Rev. Lett.* **2008**, 101, 196405.

45. Xing, G.; Guo, H.; Zhang, X.; Sum, T. C.; Huan, C. H. A., The physics of ultrafast saturable absorption in graphene. *Opt. Express* **2010**, 18, 4564.

46. Lee, C. C.; Schibli, T. R.; Acosta, G.; Bunch, J. S., Ultra-short optical pulse generation with single-layer graphene. *J. Nonlinear Opt. Phys. Mater.* **2010**, 19, 767.

47. Partoens, B.; Peeters, F. M., From graphene to graphite: Electronic structure around the k point. *Phys. Rev. B* **2006**, 74, 075404.

48. Berger, C.; Song, Z.; Li, T.; Li, X.; Ogbazghi, A. Y.; Feng, R.; Dai, Z.; Marchenkov, A. N.; Conrad, E. H.; First, P. N.; de Heer, W. A., Ultrathin epitaxial graphite: 2D electron gas properties and a route toward graphene-based nanoelectronics. *J. Phys. Chem. B* **2004**, 108, 19912.

49. Berger, C.; Song, Z. M.; Li, X. B.; Wu, X. S.; Brown, N.; Naud, C.; Mayou, D.; Li, T. B.; Hass, J.; Marchenkov, A. N.; Conrad, E. H.; First, P. N.; de Heer, W. A., Electronic confinement and coherence in patterned epitaxial graphene. *Science* **2006**, 312, 1191.

50. Ni, Z. H.; Chen, W.; Fan, X. F.; Kuo, J. L.; Yu, T.; Wee, A. T. S.; Shen, Z. X., Raman spectroscopy of epitaxial graphene on a sic substrate. *Phys. Rev. B* **2008**, 77, 115416.

51. Huang, H.; Chen, W.; Chen, S.; Wee, A. T. S., Bottom-up growth of epitaxial graphene on 6H-SiC(0001). *Acs Nano* **2008**, 2, 2513.

52. Bolen, M. L.; Harrison, S. E.; Biedermann, L. B.; Capano, M. A., Graphene formation mechanisms on 4H-SiC(0001). *Phys. Rev. B* **2009**, 80, 115433.

53. Poon, S. W.; Chen, W.; Tok, E. S.; Wee, A. T. S., Probing epitaxial growth of graphene on silicon carbide by metal decoration. *Appl. Phys. Lett.* **2008**, 92, 104102.

54. Magaud, L.; Hiebel, F.; Varchon, F.; Mallet, P.; Veuillen, J. Y., Graphene on the C-terminated SiC (0001) surface: An ab initio study. *Phys. Rev. B* **2009**, 79, 161405.

55. Chen, W.; Xu, H.; Liu, L.; Gao, X. Y.; Qi, D. C.; Peng, G. W.; Tan, S. C.; Feng, Y. P.; Loh, K. P.; Wee, A. T. S., Atomic structure of the 6H-SiC(0001) nanomesh. *Surf. Sci.* **2005**, 596, 176.

56. Obraztsov, A. N.; Obraztsova, E. A.; Tyurnina, A. V.; Zolotukhin, A. A., Chemical vapor deposition of thin graphite films of nanometer thickness. *Carbon* **2007**, 45, 2017.

57. Wei, D. C.; Liu, Y. Q.; Wang, Y.; Zhang, H. L.; Huang, L. P.; Yu, G., Synthesis of n-doped graphene by chemical vapor deposition and its electrical properties. *Nano Lett.* **2009**, 9, 1752.

58. Yu, Q. K.; Jauregui, L. A.; Wu, W.; Colby, R.; Tian, J. F.; Su, Z. H.; Cao, H. L.; Liu,

Z. H.; Pandey, D.; Wei, D. G.; Chung, T. F.; Peng, P.; Guisinger, N. P.; Stach, E. A.; Bao, J. M.; Pei, S. S.; Chen, Y. P., Control and characterization of individual grains and grain boundaries in graphene grown by chemical vapour deposition. *Nat. Mater.* **2011**, 10, 443.

59. Reina, A.; Jia, X. T.; Ho, J.; Nezich, D.; Son, H. B.; Bulovic, V.; Dresselhaus, M. S.; Kong, J., Large area, few-layer graphene films on arbitrary substrates by chemical vapor deposition. *Nano Lett.* **2009**, 9, 30.

60. Hernandez, Y.; Nicolosi, V.; Lotya, M.; Blighe, F. M.; Sun, Z. Y.; De, S.; McGovern, I. T.; Holland, B.; Byrne, M.; Gun'ko, Y. K.; Boland, J. J.; Niraj, P.; Duesberg, G.; Krishnamurthy, S.; Goodhue, R.; Hutchison, J.; Scardaci, V.; Ferrari, A. C.; Coleman, J. N., High-yield production of graphene by liquid-phase exfoliation of graphite. *Nat. Nanotechnol.* **2008**, 3, 563.

61. Cui, X.; Zhang, C. Z.; Hao, R.; Hou, Y. L., Liquid-phase exfoliation, functionalization and applications of graphene. *Nanoscale* **2011**, 3, 2118.

62. Coleman, J. N., Liquid-phase exfoliation of nanotubes and graphene. *Adv. Funct. Mater.* **2009**, 19, 3680.

63. Obrzut, J.; Migler, K. B., Optical and conductivity properties of films from liquid-phase exfoliation of natural graphite. In *Graphene and emerging materials for post-cmos applications*, Obeng, Y.; DeGendt, S.; Srinivasan, P.; Misra, D.; Iwai, H.; Karim, Z.; Hess, D. W.; Grebel, H., Eds. The Electrochemical Society: Pennington, 2009; Vol. 19, pp 69.

64. Shao, Y. Y.; Wang, J.; Wu, H.; Liu, J.; Aksay, I. A.; Lin, Y. H., Graphene based electrochemical sensors and biosensors: A review. *Electroanal.* **2010**, 22, 1027.

65. Hou, J. B.; Shao, Y. Y.; Ellis, M. W.; Moore, R. B.; Yi, B. L., Graphene-based electrochemical energy conversion and storage: Fuel cells, supercapacitors and lithium ion batteries. *Phys. Chem. Chem. Phys.* **2011**, 13, 15384.

66. Lotya, M.; Hernandez, Y.; King, P. J.; Smith, R. J.; Nicolosi, V.; Karlsson, L. S.; Blighe, F. M.; De, S.; Wang, Z. M.; McGovern, I. T.; Duesberg, G. S.; Coleman, J. N., Liquid phase production of graphene by exfoliation of graphite in surfactant/water solutions. *J. Am. Chem. Soc.* **2009**, 131, 3611.

67. Ohta, T.; Bostwick, A.; Seyller, T.; Horn, K.; Rotenberg, E., Controlling the electronic structure of bilayer graphene. *Science* **2006**, 313, 951.

68. Dawlaty, J. M.; Shivaraman, S.; Chandrashekhar, M.; Rana, F.; Spencer, M. G., Measurement of ultrafast carrier dynamics in epitaxial graphene. *Appl. Phys. Lett.* **2008**, 92, 042116.

69. Hass, J.; Varchon, F.; Mill; aacute; n-Otoya, J. E.; Sprinkle, M.; Sharma, N.; de Heer, W. A.; Berger, C.; First, P. N.; Magaud, L.; Conrad, E. H., Why multilayer graphene on 4H-SiC(000-1) behaves like a single sheet of graphene. *Phys. Rev. Lett.*

2008, 100, 125504.

70. Yuan, G. D.; Zhang, W. J.; Yang, Y.; Tang, Y. B.; Li, Y. Q.; Wang, J. X.; Meng, X. M.; He, Z. B.; Wu, C. M. L.; Bello, I.; Lee, C. S.; Lee, S. T., Graphene sheets via microwave chemical vapor deposition. *Chem. Phys. Lett.* **2009**, 467, 361.

71. Malesevic, A.; Vitchev, R.; Schouteden, K.; Volodin, A.; Zhang, L.; Van Tendeloo, G.; Vanhulsel, A.; Van Haesendonck, C., Synthesis of few-layer graphene via microwave plasma-enhanced chemical vapour deposition. *Nanotechnology* **2008**, 19, 305604

72. De Arco, L. G.; Zhang, Y.; Kumar, A.; Zhou, C. W., Synthesis, transfer, and devices of single- and few-layer graphene by chemical vapor deposition. *IEEE Trans. Nanotechnol.* **2009**, 8, 135.

73. Bae, S.; Kim, H.; Lee, Y.; Xu, X.; Park, J.-S.; Zheng, Y.; Balakrishnan, J.; Lei, T.; Ri Kim, H.; Song, Y. I.; Kim, Y.-J.; Kim, K. S.; Ozyilmaz, B.; Ahn, J.-H.; Hong, B. H.; Iijima, S., Roll-to-roll production of 30-inch graphene films for transparent electrodes. *Nat. Nanotechnol.* **2010**, 5, 574.

74. Kim, K. S.; Zhao, Y.; Jang, H.; Lee, S. Y.; Kim, J. M.; Ahn, J. H.; Kim, P.; Choi, J. Y.; Hong, B. H., Large-scale pattern growth of graphene films for stretchable transparent electrodes. *Nature* **2009**, 457, 706.

75. Ferrari, A. C.; Meyer, J. C.; Scardaci, V.; Casiraghi, C.; Lazzeri, M.; Mauri, F.; Piscanec, S.; Jiang, D.; Novoselov, K. S.; Roth, S.; Geim, A. K., Raman spectrum of graphene and graphene layers. *Phys. Rev. Lett.* **2006**, 97, 187401.

76. Green, A. A.; Hersam, M. C., Solution phase production of graphene with controlled thickness via density differentiation. *Nano Lett.* **2009**, 9, 4031.

77. Keller, U., Materials and new approaches for ultrashort pulse lasers. *Curr. Opin. Solid State Mater. Sci.* **1996**, 1, 218.

78. Hargrove, L. E.; Fork, R. L.; Pollack, M. A., Locking of he-ne laser modes induced by synchronous intracavity modulation. *Appl. Phys. Lett.* **1964**, 5, 4.

79. Mocker, H. W.; Collins, R. J., Mode competition and self-locking effects in a q-switched ruby laser. *Appl. Phys. Lett.* **1965**, 7, 270.

80. Deutsch, T., Mode-locking effects in an internally modulated ruby laser. *Appl. Phys. Lett.* **1965**, 7, 80.

81. DeMaria, A. J.; Stetser, D. A.; Heynau, H., Self mode-locking of lasers with saturable absorbers. *Appl. Phys. Lett.* **1966**, 8, 174.

82. DiDomenico, J. M.; Geusic, J. E.; Marcos, H. M.; Smith, R. G., Generation of ultrashort optical pulses by mode locking the yaig: Nd laser. *Appl. Phys. Lett.* **1966**, 8, 180.

83. Keller, U., Recent developments in compact ultrafast lasers. *Nature* **2003**, 424, 831.

84. Lagatsky, A. A.; Leburn, C. G.; Brown, C. T. A.; Sibbett, W.; Zolotovskaya, S. A.; Rafailov, E. U., Ultrashort-pulse lasers passively mode locked by quantum-dot-based saturable absorbers. *Prog. Quant. Electron.* **2010**, 34, 1.

85. Goodberlet, J.; Jacobson, J.; Fujimoto, J. G.; Schulz, P. A.; Fan, T. Y., Self-starting additive-pulse mode-locked diode-pumped nd:Yag laser. *Opt. Lett.* **1990**, 15, 504.

86. Cerullo, G.; Silvestri, S. D.; Magni, V., Self-starting kerr-lens mode locking of a ti:Sapphire laser. *Opt. Lett.* **1994**, 19, 1040.

87. Keller, U.; Miller, D. A. B.; Boyd, G. D.; Chiu, T. H.; Ferguson, J. F.; Asom, M. T., Solid-state low-loss intracavity saturable absorber for nd:Ylf lasers: An antiresonant semiconductor fabry-perot saturable absorber. *Opt. Lett.* **1992**, 17, 505.

88. Haiml, M.; Grange, R.; Keller, U., Optical characterization of semiconductor saturable absorbers. *Appl. Phys. B* **2004**, 79, 331.

89. Hasan, T.; Sun, Z. P.; Wang, F. Q.; Bonaccorso, F.; Tan, P. H.; Rozhin, A. G.; Ferrari, A. C., Nanotube-polymer composites for ultrafast photonics. *Adv. Mater.* **2009**, 21, 3874.

90. Wang, J.; Chen, Y.; Blau, W. J., Carbon nanotubes and nanotube composites for nonlinear optical devices. *J. Mater. Chem.* **2009**, 19, 7425.

91. Ursula, K., Ultrafast solid-state lasers. In *Progress in optics*, Elsevier: 2004; Vol. 46, pp 1.

92. Xiang, N., *Monolithic semiconductor saturable absorber mirrors for ultra-short optical pulse generation*. Tampere University of Technology: 2003.

93. Rulli ère, C., *Femtosecond laser pulses: Principles and experiments*. 2nd ed.; Springer: New York, 2005.

94. Jung, I. D.; Kartner, F. X.; Matuschek, N.; Sutter, D. H.; MorierGenoud, F.; Shi, Z.; Scheuer, V.; Tilsch, M.; Tschudi, T.; Keller, U., Semiconductor saturable absorber mirrors supporting sub-10-fs pulses. *Appl. Phys. B* **1997**, 65, 137.

95. Ippen, E. P.; Eilenberger, D. J.; Dixon, R. W., Picosecond pulse generation by passive-mode locking of diode-lasers. *Appl. Phys. Lett.* **1980**, 37, 267.

96. Silberberg, Y.; Smith, P. W.; Eilenberger, D. J.; Miller, D. A. B.; Gossard, A. C.; Wiegmann, W., Passive-mode locking of a semiconductor diode-laser. *Opt. Lett.* **1984**, 9, 507.

97. Vanderziel, J. P.; Tsang, W. T.; Logan, R. A.; Mikulyak, R. M.; Augustyniak, W. M., Subpicosecond pulses from passively mode-locked gaas buried optical guide semiconductor-lasers. *Appl. Phys. Lett.* **1981**, 39, 525.

98. Set, S.; Yaguchi, H.; Jablonski, M.; Tanaka, Y.; Sakakibara, Y.; Rozhin, A.; Tokumoto, M.; Kataura, H.; Achiba, Y.; Kikuchi, K. In *A noise suppressing saturable absorber at 1550 nm based on carbon nanotube technology*, Optical Fiber

Communications Conference, 2003; pp 723.

99. Set, S. Y.; Yaguchi, H.; Tanaka, Y.; Jablonski, M., Laser mode locking using a saturable absorber incorporating carbon nanotubes. *J. Lightwave Technol.* **2004**, 22, 51.

100. Sun, Z.; Lin, X. C.; Yu, H. J.; Hasan, T.; Torrisi, F.; Zhang, L.; Sun, L.; Guo, L.; Hou, W.; Li, J. M.; Ferrari, A. C. In *High-power ultrafast solid-state laser using graphene based saturable absorber*, 2011 Conference on Lasers and Electro-Optics (CLEO), 1-6 May 2011; 2011; p JWA79.

101. Sun, Z.; Hasan, T.; Popa, D.; Torrisi, F.; Wang, F.; Bonaccorso, F.; Ferrari, A. C. In *Ultrafast fiber laser mode-locked by graphene based saturable absorber*, Conference on Lasers and Electro-Optics (CLEO)/Quantum Electronics and Laser Science Conference (QELS), 2010; p CTuR1.

102. Sun, Z.; Lin, X. C.; Popa, D.; Yu, H. J.; Hasan, T.; Torrisi, F.; Kelleher, E. J. R.; Zhang, L.; Sun, L.; Guo, L.; Hou, W.; Li, J. M.; Taylor, J. R.; Ferrari, A. C. In *Wideband tunable, high-power, graphene mode-locked ultrafast lasers*, 2011 Conference on Lasers and Electro-Optics Europe and 12th European Quantum Electronics Conference (CLEO EUROPE/EQEC), 2011.

103. Sun, Z. P.; Popa, D.; Hasan, T.; Torrisi, F.; Wang, F. Q.; Kelleher, E. J. R.; Travers, J. C.; Nicolosi, V.; Ferrari, A. C., A stable, wideband tunable, near transform-limited, graphene-mode-locked, ultrafast laser. *Nano Res.* **2010**, 3, 653.

104. Popa, D.; Sun, Z.; Torrisi, F.; Hasan, T.; Wang, F.; Ferrari, A. C., Sub 200 fs pulse generation from a graphene mode-locked fiber laser. *Appl. Phys. Lett.* **2010**, 97, 203106.

105. Popa, D.; Sun, Z.; Torrisi, F.; Hasan, T.; Wang, F.; Ferrari, A. C. In *Ultrafast and high-energy pulsed lasers with graphene mode-lockers*, 2011 Conference on Lasers and Electro-Optics Europe and 12th European Quantum Electronics Conference (CLEO EUROPE/EQEC), 2011.

106. Kim, H.; Cho, J. H.; Jang, S. Y.; Song, Y. W. In *Nonlinearity-preserved graphene/PVAC composite in optical deposition for fiber mode-locked lasers*, Conference on Optical Fiber Communication (OFC)/National Fiber Optic Engineers Conference(NFOEC), Optical Society of America: 2011; p OThL2.

107. Xu, J.; Liu, J.; Wu, S. D.; Yang, Q. H.; Wang, P. In *High energy low-repetition-rate graphene mode-locked Er-doped fiber lasers*, International Symposium on Photoelectronic Detection and Imaging 2011: Laser Sensing and Imaging and Biological and Medical Applications of Photonics Sensing and Imaging, 2011; p 81924B.

108. Martinez, A.; Yamashita, S. In *Fiber fabry-perot laser mode-locked by graphene for the generation of supercontinuum with 10GHz mode spacing*, 2011 Conference on Lasers and Electro-Optics (CLEO), 1-6 May 2011; 2011; p CMBB4.

109. Zhang, H.; Tang, D. Y.; Zhao, L. M.; Bao, Q. L.; Loh, K. P., Large energy mode locking of an erbium-doped fiber laser with atomic layer graphene. *Opt. Express* **2009**, 17, 17630.

110. Zhang, H.; Tang, D. Y.; Knize, R. J.; Zhao, L. M.; Bao, Q. L.; Loh, K. P., Graphene mode locked, wavelength-tunable, dissipative soliton fiber laser. *Appl. Phys. Lett.* **2010**, 96, 111112.

111. Cho, W. B.; Lee, H. W.; Choi, S. Y.; Kim, J. W.; Yeom, D. I.; Rotermund, F.; Kim, J.; Hong, B. H. In *Monolayer graphene saturable absorber for bulk laser mode-locking*, Conference on Lasers and Electro-Optics (CLEO)/Quantum Electronics and Laser Science Conference (QELS), 2010; p JThE86.

112. Chien-Chung, L.; Guillermo, A.; Scott, B.; Thomas, R. S. In *Mode-locking of an Er:Yb:Glass laser with single layer graphene*, International Conference on Ultrafast Phenomena, Optical Society of America: 2010; p TuE29.

113. Zhang, H.; Tang, D. Y.; Zhao, L. M.; Bao, Q. L.; Loh, K. P.; Lin, B.; Tjin, S. C., Compact graphene mode-locked wavelength-tunable erbium-doped fiber lasers: From all anomalous dispersion to all normal dispersion. *Laser Phys. Lett.* **2010**, 7, 591.

114. Zhang, H.; Tang, D. Y.; Zhao, L. M.; Bao, Q. L.; Loh, K. P., Vector dissipative solitons in graphene mode locked fiber lasers. *Opt. Commun.* **2010**, 283, 3334.

115. Zhao, L. M.; Tang, D. Y.; Zhang, H.; Wu, X.; Bao, Q. L.; Loh, K. P., Dissipative soliton operation of an ytterbium-doped fiber laser mode locked with atomic multilayer graphene. *Opt. Lett.* **2010**, 35, 3622.

116. Zhao, L. M.; Tang, D. Y.; Zhang, H.; Wu, X.; Qiaoliang, B.; Kian Ping, L. In *Atomic multi-layer graphene for dissipative soliton generation in ytterbium-doped fiber laser*, 2010 Photonics Global Conference (PGC), 2010.

117. Bao, Q. L.; Zhang, H.; Ni, Z. H.; Wang, Y.; Polavarapu, L.; Shen, Z. X.; Xu, Q. H.; Tang, D. Y.; Loh, K. P., Monolayer graphene as a saturable absorber in a mode-locked laser. *Nano Res.* **2011**, 4, 297.

118. Chao-Yung, Y.; Lain-Jong, L.; Shau-Ching, L.; Wood-Hi, C. In *Carbon natnotubes and graphene saturable absorber for ultrafast laser mode locking*, 16th OptoeElectronics and Communications Conference (OECC), 4-8 July 2011; 2011; pp 157.

119. Shau-Ching, L.; Pi-Ling, H.; Bi-Zen, H.; Shr-Hau, H.; Chao-Yung, Y.; Jiang-Jen, L.; Wood-Hi, C. In *Mode-locked lasers using polyurethane dispersed graphene saturable absorber*, 16 th OptoeElectronics and Communications Conference (OECC), 2011; pp 307.

120. Mi-Kyung, B.; Won-Suk, H.; Sung-Yeon, J.; Yong-Won, S. In *High-energy pulse formation using graphene as saturable absorber*, 15th OptoeElectronics and Communications Conference (OECC), 5-9 July 2010; 2010; pp 554.

121. Tan, W. D.; Su, C. Y.; Knize, R. J.; Xie, G. Q.; Li, L. J.; Tang, D. Y., Mode locking of ceramic Nd:Yttrium aluminum garnet with graphene as a saturable absorber. *Appl. Phys. Lett.* **2010**, 96, 031106.

122. Gui, L. L.; Zhang, W.; Li, X.; Xiao, X. S.; Zhu, H. W.; Wang, K. L.; Wu, D. H.; Yang, C. X., Self-assembled graphene membrane as an ultrafast mode-locker in an erbium fiber laser. *IEEE Photonics Technol. Lett.* **2011**, 23, 1790.

123. Lili, G.; Wei, Z.; Xiao, L.; Xiaosheng, X.; Hongwei, Z.; Kunlin, W.; Dehai, W.; Changxi, Y. In *Mode-locked operation of an erbium-doped fiber laser using a self-assembled graphene membrane after excitation of Q-switched pulse*, 2011 Conference on Lasers and Electro-Optics Europe and 12th European Quantum Electronics Conference (CLEO EUROPE/EQEC), 2011.

124. Zhang, H.; Bao, Q. L.; Tang, D. Y.; Zhao, L. M.; Loh, K., Large energy soliton erbium-doped fiber laser with a graphene-polymer composite mode locker. *Appl. Phys. Lett.* **2009**, 95, 141103.

125. Chang, Y. M.; Kim, H.; Lee, J. H.; Song, Y. W. In *Passive mode-locker incorporating physically exfoliated graphene for fiber ring lasers*, Conference on Optical Fiber Communication (OFC)/National Fiber Optic Engineers Conference(NFOEC), Optical Society of America: 2011; p OThL3.

126. Martinez, A.; Fuse, K.; Yamashita, S., Mechanical exfoliation of graphene for the passive mode-locking of fiber lasers. *Appl. Phys. Lett.* **2011**, 99, 121107.

127. Martinez, A.; Fuse, K.; Bo, X.; Yamashita, S. In *Mechanical exfoliation of graphene for mode-lock laser applications*, 16th OptoeElectronics and Communications Conference (OECC), 4-8 July 2011; 2011; pp 792.

128. Jiang, L.; Rusheng, W.; Xiangang, X.; Pu, W. In *Mode-locked fiber laser with few-layer epitaxial graphene grown on 6H-SiC substrates*, 2011 Conference on Lasers and Electro-Optics (CLEO), 1-6 May 2011; 2011; p CMK3.

129. Liu, J.; Wu, S.; Yang, Q. H.; Wang, P. In *Mode-locked and Q-switched Yb-doped fiber lasers with graphene saturable absorber*, International Symposium on Photoelectronic Detection and Imaging 2011: Laser Sensing and Imaging and Biological and Medical Applications of Photonics Sensing and Imaging, 2011; p JWA23.

130. Jiang, L.; Sida, W.; Quan-Hong, Y.; Pu, W. In *High-energy all-normal-dispersion graphene mode-locked Yb-doped fiber laser*, 2011 Conference on Lasers and Electro-Optics Europe and 12th European Quantum Electronics Conference (CLEO EUROPE/EQEC), 2011.

131. Bao, Q. L.; Zhang, H.; Yang, J. X.; Wang, S.; Tong, D. Y.; Jose, R.; Ramakrishna, S.; Lim, C. T.; Loh, K. P., Graphene-polymer nanofiber membrane for ultrafast photonics. *Adv. Funct. Mater.* **2010**, 20, 782.

132. Vasko, F. T., Saturation of interband absorption in graphene. *Phys. Rev. B* **2010**, 82, 245422.

133. Zhang, Z.; Voss, P. L., Full-band quantum-dynamical theory of saturation and four-wave mixing in graphene. *Opt. Lett.* **2011**, 36, 4569.

134. Yang, H.; Feng, X.; Wang, Q.; Huang, H.; Chen, W.; Wee, A. T. S.; Ji, W., Giant two-photon absorption in bilayer graphene. *Nano Lett.* **2011**, 11, 2622.

Chapter 2

Photodynamic model

2.1 Ultrafast carrier dynamics in graphene

In recent years, graphene has been successfully demonstrated for many technological applications that highlight its novelty and versatility as a platform for electronic, optoelectronic, photonic, and terahertz devices.[1-4] For graphene based optoelectronic or photonic devices, optimization or improvement of device performance requires a good understanding of nonequilibrium carrier dynamics associated with cooling and recombination of photoexcited carriers. Therefore, photoexcited carrier dynamics in graphene has been a hot research topic attracting intensive attentions.

Many experimental studies revealed that the dynamics of photoexcitation in graphene occurs on ultrafast time scales, governed by the interactions among carriers and their coupling to the lattice.[5-25] The mechanism is schematically illustrated in Figure 2.1, and can be briefly described as follows. Immediately following optical interband excitation by an ultrashort optical pulse, photoexcited electrons (or holes) are in a nonthermal distribution near $\pm (h\nu/2)$ from the band edge, as shown in Figure 2.1(a). This nonequilibrium distribution then transforms into a quasi-equilibrium distribution by carrier-carrier (c-c) and carrier-phonon (c-p) scattering.[5-25] As stated by Breusing *et*

al., there are two potential scenarios for this equilibration process [11]:

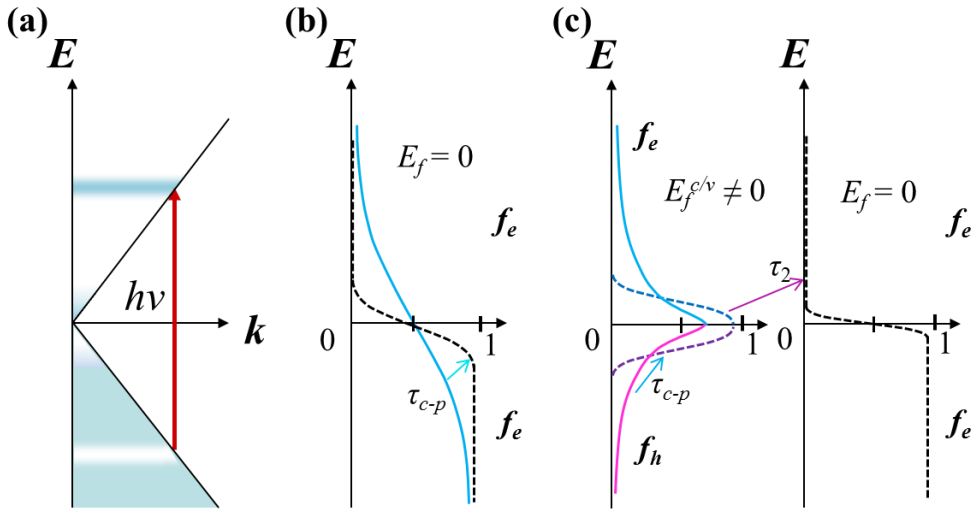

Figure 2.1 (a) Linear band structure of graphene, red arrow indicating interband photoexcitation. **(b)** Schematic of temporally evolving electronic occupation probabilities (f_e) after optical excitation and under the influence of c-p scattering (indicated by $\tau_{c\text{-}p}$), assuming a thermalization towards zero chemical potential. **(c) Left panel:** schematic of temporally evolving electron (f_e) and hole (f_h) occupation probabilities with separate nonzero Fermi levels ($E_f^{c/v} \neq 0$). **Right panel:** The black dashed curve represents restored room temperature equilibrium electron distribution (f_e), characterized by a single Fermi-Dirac distribution function with $E_f = 0$.[11]

(i) If the intra- and interband scattering possess similar rates, a hot equilibrium (Fermi-Dirac) distribution with a Fermi level $E_f = 0$ would be formed, which involves ultrafast electron-hole (e-h) recombination processes [see Figure 2.1(b)].[11] Initially, these equilibrium carriers have an elevated temperature. On a somewhat longer time scale, they cool down by c-p scattering. Thus, the conduction band population experiences a strong variation in this case.

(ii) If the intraband scattering rate is much higher than that of interband scattering/recombination, persistent electron and hole populations would broaden and equilibrate with the intrinsic carrier population through c-c scattering. As a result of c-c scattering, the photogenerated carriers are expected to equilibrate among themselves and establish separate Fermi-Dirac distributions of electrons in the conduction band and holes in the valence band with separate nonzero Fermi levels $E_f^{c/v}$ and elevated temperatures $T_{e/h}$, which are higher than the lattice temperature [see Figure 2.1 (c)]. These photoexcited carriers could block further absorption within a range of $K_B T_e$ around the edge of the conduction and valence bands $E_f^{c/v}$, giving rise to state-filling effects (or Puali blocking). T_e and T_h vary in time during the phonon-mediated carrier cooling [Figure 2.1(c)], while for the symmetric band structure of Figure 2.1(a) and similar cooling rates of electrons and holes, $T_e = T_h$ at all times. Carrier-phonon intraband scattering further cools the thermalized carriers and e-h recombination eventually dominates the relaxation process, until the room-temperature-equilibrium carrier distribution (single distribution with $E_f = 0$) is restored.

In 2007, Butscher *et al*. reported the theoretical study on the relaxation dynamics of photoexcited electrons in graphene.[7] Later, Dawlaty *et al.* reported the experimental investigation on ultrafast carrier dynamics in graphene for the first time in 2008.[8] They found two distinct time scales associated with the relaxation of nonequilibrium photogenerated carriers in epitaxial graphene layers using ultrafast optical pump-probe spectroscopy. An initial fast relaxation transient in the 70 – 120 fs range followed by a

slower relaxation process in the range of 0.4 – 1.7 ps which are attributed to the c-c intraband scattering and c-p intraband/interband scattering processes. Their experimental findings are consistent with the scenario (ii) discussed above, revealing that intraband scattering rate is much higher than interband scattering/recombination. Additionally, the slower relaxation time is found to be independent of the excitation intensity. Moreover, many research efforts on relaxation dynamics of photoexcited carriers in graphene have recently been devoted using ultrafast optical/IR pump-optical/IR/terahertz probe spectroscopy by several groups.[8-23] Table 2.1 summarizes most of the representative works on graphene in visible-infrared (IR) [8, 9, 11-21, 23] and terahertz [10, 12] region. In these studies, graphene fabricated by exfoliation [11, 13, 17], epitaxial [8-10, 12, 14, 16, 19], and CVD [15, 16, 19-21, 23]methods have been used.

Table 2.1 Investigations on ultrafast carrier dynamics in graphene.

Pump condition	Probe condition	Relaxation time scales			Sample	Temperature	Year	Ref.
		τ_1	τ_c	τ_2				
780 nm, 85 fs, 81 MHz	degenerate	70 – 120 fs (c-c, c-p scattering)		0.4 – 1.7 ps (c-p intra- & inter-band scattering)	epitaxial 6, 12, 37 layers	300 K	2008	[8]
800 nm, 100 fs, 250 KHz	1.1 – 2.6 μm	< 150 fs (c-c scattering)		1 – 11 ps (c-ap scattering)	epitaxial ~20 layers	10 K – 290 K	2008	[9]
780 nm, 90 fs, 81 MHz	0.3 – 3.0 THz	10 - 150 fs (c-c scattering)	150 fs – 1 ps (c-p intraband scattering)	1 – 15 ps (e-h recombination)	epitaxial 12, 20 layers	300 K	2008	[10]
1.2 – 1.8 eV, 7 fs,71 MHz	degenerate	20 – 30 fs (c-c, c-op scattering)	50 – 250 fs (c-op scattering)	a few ps (e-h recombination)	exfoliated 20 ~ 30 nm	300 K	2009/ 2011	[11, 18]
810 nm, fs pulse, 250 KHz	IR, THz			~ 1.2 ps (e-h recombination)	epitaxial 1, 4 layers	300 K	2009	[12]
800 nm, 150 fs, 80 MHz	1300 nm	200 – 300 fs (c-c scattering)		2.5 – 5 ps (carrier recombination and/or energy relaxation)	exfoliated 1 – 260 layers	295 K	2009	[13]
390 nm, 230 fs, 89 MHz	780 nm	< 200 fs (c-op scattering)		1 – 2 ps (hot phonon effect)	epitaxial few-, multi-layers	300 K	2010/ 2011	[14, 19]
350 nm, 65 fs, 1 KHz	380 – 670 nm	50 – 70 fs (c-c scattering & initial phonon-mediated carrier cooling)	100 – 200 fs (visible range, c-op scattering)	~ 1.2 ps (near-IR region, op-ap scattering)	CVD multilayer (1 – 4, 8, 10 layers)	300 K	2010/ 2011	[15, 21]
780 nm, 100 fs, 81 MHz	degenerate		500 fs (c-op scattering)		epitaxial 2, 16, 55 layers, CVD ~2 layer	300 K	2010	[16]

Table 2.1. (*Contd.*)

Pump condition	**Probe condition**	**Relaxation time scales**			**Sample**	**Temperature**	**Year**	**Ref.**
		τ_1	τ_c	τ_2				
800 nm, 40 fs, 80 MHz	degenerate		< 160 fs (c-op scattering)	1.5 – 3.4 ps (op-ap coupling)	exfoliated bilayer	10 – 290 K	2010	[17]
1000 – 1700 nm, 120 fs, 1 KHz	900 – 1700 nm		~250 fs (c-op scattering)	~2.4 ps (e-h recombination)	CVD 5, 15, 37, 39 layers	300 K	2011	[20]
780 nm, 90 fs, 81 MHz	THz	tens of femtoseconds (c-c scattering)		~ 1 ps	epitaxial 14, 30 layers	18 – 300 K	2011	[22]
795 nm, 100 fs	0.4 – 1.2 eV		< 500 fs (intraband carrier relaxation)	8.7 ps (e-h recombination)	CVD 1, 10 layers	80 K	2011	[23]

As demonstrated in Figure 2.2, it is generally agreed that following ultrafast photoexcitation, the charge carriers initially scatter and thermalize to quasi-equilibrium with a characteristic time of tens of femtoseconds (τ_1).[10, 11] These hot charge carriers subsequently lose a majority of their energy within hundreds of femtoseconds (τ_c) by transferring energy to the lattice via coupling to optical phonons (c-op scattering) [10, 11, 14-17, 19, 21]. In turn, the optical phonons subsequently relax through anharmonic coupling to acoustic phonons (op-ap scattering) [14, 17, 19, 21]. Within several picoseconds (τ_2), room temperature equilibrium is restored via interband carrier relaxation processes dominated by e-h recombination [8, 10-13, 18, 23].

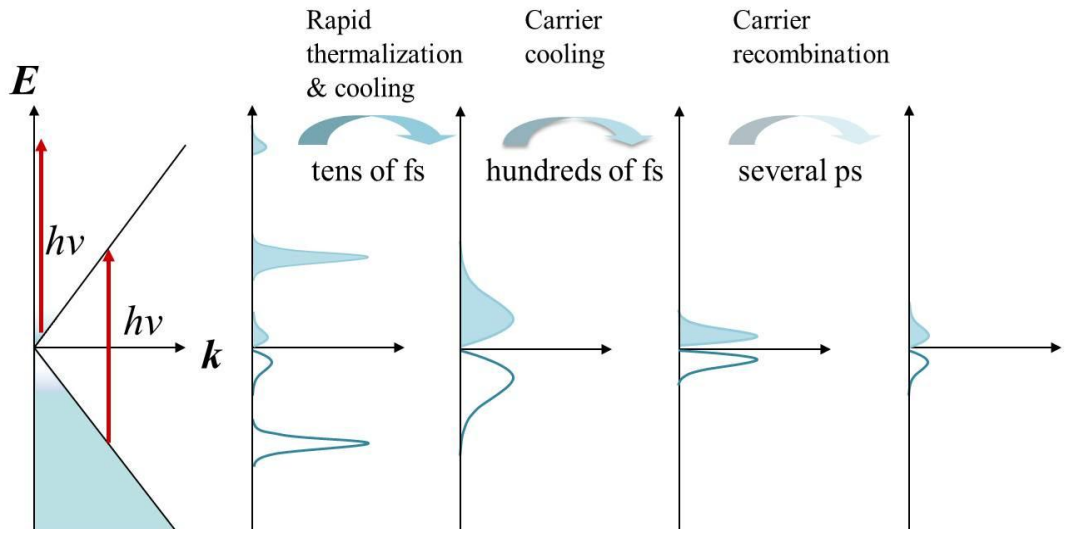

Figure 2.2 Schematic diagrams for photodynamics: After excitation (interband and intraband), the distribution rapidly thermalizes and cools to form a quasi-equilibration. The hot thermally distributed carriers are then cools further due to intraband phonon scattering. Finally, electrons and holes recombine until the equilibrium distribution is restored.

2.2 Literature review on theoretical treatments for saturable absorption in graphene

Given the importance of graphene saturable absorbers as reviewed in Section 1.3.3, theoretical investigations on saturable absorption of graphene have also been performed. Here, we describe them in a chronological order.

The ultrafast carrier dynamic model incorporating band-filling effects together with intraband c-c and c-p scattering, as discussed in Section 2.1, was firstly presented by Dawlaty *et al.* in 2008 [8]. In this work, saturable absorption in graphene was experimentally observed using time-resolved pump-probe spectroscopy. The photodynamic model was then used to qualitatively explain their experimental observations of transient transmittivity. However, this work was mainly focused on uncovering the ultrafast carrier dynamics in graphene and no quantitative study on the saturation intensity of graphene, both experimentally and theoretically, was carried out.

This photodynamic model was then studied in detail by Sun *et al.* [26]. In their study, a stationary state, which can be represented by the Fermi distribution with an assumed effective temperature T_{eff}, was taken as the starting point, giving the carrier occupation probabilities as $f_e(\boldsymbol{p}) = f_h(\boldsymbol{p}) = 1/(\exp(vp/T_{eff})+1)$. Based on this Fermi distribution $f_{e,h}(\boldsymbol{p})$, the photoexcited concentration $n_{e,h}$ and total energy density E were expressed as: $n_{e,h} = 4\int d^2\boldsymbol{p}\cdot f_{e,h}(\boldsymbol{p})/(2\pi)^2, E = 4\int d^2\boldsymbol{p}\cdot vp[f_e(\boldsymbol{p}) + f_h(\boldsymbol{p})]/(2\pi)^2$. The populations also determine the reduction of photo absorption for given laser energy ε_{in}, due to Pauli

blocking, by a factor $1+\Delta\alpha_1/\alpha_1=[1-f_e(\boldsymbol{p})][1-f_h(\boldsymbol{p})]$. From the experimentally measured absorbance of graphene monolayer, $1+\Delta\alpha_1/\alpha_1\sim 0.92$, Sun *et al*. extracted T_{eff} ~ 0.13 eV. In order to estimate T_{eff} theoretically, they assumed that during the pulsed excitation, electrons were photoexcited at a constant rate. This carrier excitation rate was computed from the experimentally measured absorbance,

$$dn_e/dt|_{pump}=dn_h/dt|_{pump}=J_{in}=\frac{\text{density of photons absorbed per pulse per layer}}{\text{pulse width}}.$$

The corresponding energy pumping rate was thus given numerically by $dE/dt|_{pump}=2J_{in}\varepsilon_{in}$. Subsequently the electronic energy cooling rate $dE/dt|_{ph}$ was calculated based on the optical and acoustic phonons emission. From the thermal balance equation $dE/dt|_{pump}+dE/dt|_{ph}=0$, the authors obtained a theoretical estimate of T_{eff} = 0.2 eV. This T_{eff} was then substituted into the Fermi distribution function and the absorption equation to obtain that $1+\Delta\alpha_1/\alpha_1=[1-f_e][1-f_h]=0.78$. This work is the first attempt to quantitatively investigate the saturable absorption in graphene. However, it should be noted that the authors set the Fermi level of the quasi-equilibration state after photoexcitation to be always E_f = 0, which is in contrast to many other reports [4, 7, 8, 10, 11]. More importantly, they did not present the quantitative relation between the saturation intensity and other parameters like light wavelength, the refractive index of the substrate, and number of graphene layers.

In 2010, Xing *et al*. reported a mathematical method to calculate the saturation intensity (I_s) theoretically for the first time [27]. Different from the two works introduced

above, the occupation probabilities $f(\pm\varepsilon)$ were not expressed by the Fermi-Dirac distribution function. Instead, they were described by a pair of temporal differential equations, which means that no stationary state was considered in this analysis. Thus, the absorption probability per unit time $\pi\alpha\cdot(f_t(-\varepsilon)-f_t(\varepsilon))$ can be obtained by solving the equations. Then, the optical absorbance over the laser pulse can be calculated accordingly by integrating temporally and plotted as a function of the incident laser intensity. Thereby, the saturation intensity can be extracted as the intensity where the absorbance decreased by half. This quantitative treatment considered the Gaussian temporal and spatial profile precisely, thus it may best represent the experimental operating laser conditions. However, the saturation intensity obtained relied on the intraband carrier relaxation time τ_1 used in the differential equations. The authors reported an ultrafast relaxation time of ~ 7 fs by fitting the experimental results. Additionally, the authors also totally neglected the effects of substrate and graphene layer number.

Vasko performed a complete theoretical treatment of the saturation mechanism of graphene within the frame work of the temporally local approach [28]. Similar to Xing's theory, the occupation probabilities f_{pt} were also described by a temporal differential equation instead of the Fermi-Dirac distribution function, meaning that no quasi-equilibration was assumed. Transient evolutions of the absorption and transmission coefficients were averaged over pulse duration to get the absorbance and transmittance of an ideal monolayer graphene as a function of the pumping laser intensity. The

saturation thresholds for ultrafast lasers with 10 μm, 1550 nm and 800 nm wavelengths were extracted, respectively. The experiment report has shown that the intraband carrier relaxation by c-c scattering (in 10~ 30 fs) is much faster than the c-op scattering (in hundreds of fs) [11] and thus might be non-negligible in the collision integral $J(f_t \mid p)$ [28]. However, the author ignored c-c scattering, which may weaken the reliability of their results. Moreover, the broadening factor γ chosen, which is still lack of effective accuracy estimation methods, would greatly affect the saturation intensity obtained. A possible contribution from the substrate vibration or multilayer of graphene was also not taken into consideration, which was another disadvantage of their work.

More recently, Zhang and Voss studied saturation effects by full-band quantum-dynamical theory.[29] Two phenomenological time constants (τ_1 carrier relaxation and τ_2 quantum decoherence) were used to evaluate the linear optical response, saturable absorption and four-wave mixing in graphene. With the experimentally obtained saturation intensity and τ_2, τ_1 was extracted as the only parameter by data fitting. However, the quantum decoherence and carrier relaxation rate would vary from sample to sample, thus it might be impractical to get accurate theoretical saturation threshold reversely. Similar to the above works, the authors also did not consider the effects of the substrate and multilayer graphene.

As discussed above, all these theoretical models suffer from the same drawback: both the substrate and number of graphene layers are not taken into consideration. Under this context, in our study we take a set of assumptions to quantitatively compute

the dispersion (or light-wavelength dependence) of saturable absorption in intrinsic multilayer graphene on a substrate. It is given as follows.

2.3 Photodynamic model of saturable absorption in graphene

2.3.1 Universal linear absorption of graphene

Before extending to compute nonlinear optical response of graphene, we first start from discussing its unique universal linear optical absorption. The universal linear absorption in graphene has been extensively investigated in many articles [30-32]. Here we emphasize those aspects which are relevant to saturable absorption in graphene, so that we can lay out a theoretical simulations basis.

We start from demonstrating the expression of absorbance (A) in graphene. The reflectance (R) and transmittance (T) of light at the interface of air and the substrate separated by a graphene sheet can be derived from Maxwell's equations.[32, 33] Figure 2.3 illustrates the scattering geometry of the electric fields for the incident light ($\boldsymbol{E_i}$), the light transmitted through the graphene sheet to the substrate ($\boldsymbol{E_s}$), and the light transmitted through the substrate to air ($\boldsymbol{E_t}$). Normally, the thickness of the substrate (sub-millimeter) is much larger compared with that of the graphene sheets (0.335 nm per layer) and can be treated as semi-infinite when calculating T through graphene into the substrate. In the following, we assume the field to be given by $\boldsymbol{E} = (E_x, 0, E_z)$ (p-polarization) and propagate in the direction $\boldsymbol{k} = (k_x, 0, k_z)$.

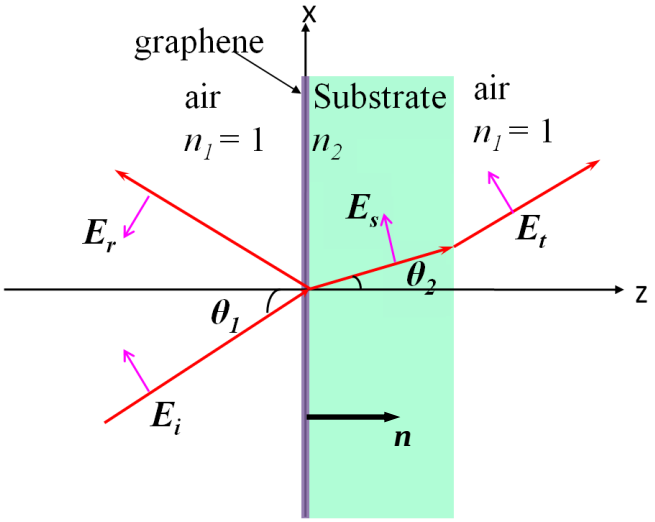

Figure 2.3 Schematic diagram for *p*-polarized light scattering on graphene separated interfaces. n_1 / n_2 represent the refractive indices of the two media.

At the graphene separated interfaces, the electromagnetic boundary conditions then are defined by [32, 33]

$$(\boldsymbol{D}_2 - \boldsymbol{D}_1)\cdot \boldsymbol{n} = \rho\,, \tag{2.1}$$

$$\boldsymbol{n}\times(\boldsymbol{E}_2 - \boldsymbol{E}_1) = 0\,, \tag{2.2}$$

where ρ is the graphene charge density. It should be noticed that ρ= 0 for simple (nonconducting) interface between two dielectrics. By representing the intensity of the incident, reflected, and transmitted electric field as E_i, E_r, and E_s, respectively, the boundary conditions can be written as

$$(E_i - E_r)\cos\theta_1 = E_s\cos\theta_2\,, \tag{2.3}$$

$$-\epsilon_2\epsilon_0 E_s\sin\theta_2 + \epsilon_1\epsilon_0(E_i + E_r)\sin\theta_1 = \rho\,, \tag{2.4}$$

where θ_1 and θ_2 are the incident and refracted angles satisfying Snell's Law $n_1 \sin\theta_1 = n_2 \sin\theta_2$ (n_1 and n_2 are the refractive indices of air and the substrate), ϵ_0 is the vacuum permittivity, $\epsilon_1 = n_1^2$ and $\epsilon_2 = n_2^2$ are the relative permittivity of the two media, respectively. Now the continuity equation in momentum space is expressed as

$$\rho(\omega) = j_x(\omega) k_x / \omega, \tag{2.5}$$

where k_x is the *x*-component of the wave propagation vector, which can be written as

$$k_x = n_1(\omega/c)\sin\theta_1 = n_2(\omega/c)\sin\theta_2, \tag{2.6}$$

and Ohm's law is written as

$$j_x(\omega) = \sigma(\omega) E_x = \sigma(\omega) E_s \cos\theta_2, \tag{2.7}$$

where $\sigma(\omega)$ is the optical conductivity of graphene at angular frequency (ω).

Combining Equations (2.3)-(2.7), the reflectance and transmittance of the graphene sheet are given by [32-35]:

$$\begin{aligned} R &= \left|\frac{E_r}{E_i}\right|^2 = \left|\frac{n_2\cos\theta_1 - n_1\cos\theta_2 + m\cdot\sigma(\omega)\cos\theta_1\cos\theta_2/\varepsilon_0 c}{n_2\cos\theta_1 + n_1\cos\theta_2 + m\cdot\sigma(\omega)\cos\theta_1\cos\theta_2/\varepsilon_0 c}\right|^2, \\ T &= \left|\frac{E_s}{E_i}\right|^2 \cdot \frac{n_2\cos\theta_2}{n_1\cos\theta_1} = \frac{4 n_1 n_2 \cos\theta_1\cos\theta_2}{\left|n_2\cos\theta_1 + n_1\cos\theta_2 + m\cdot\sigma(\omega)\cos\theta_1\cos\theta_2/\varepsilon_0 c\right|^2}, \end{aligned} \tag{2.8}$$

for *p*-polarized incident light.

Similarly, the reflectance and transmittance of the graphene sheet for *s*-polarization can be derived as

$$R = \left|\frac{E_r}{E_i}\right|^2 = \left|\frac{n_1\cos\theta_1 - n_2\cos\theta_2 - m\cdot\sigma(\omega)/\varepsilon_0 c}{n_1\cos\theta_1 + n_2\cos\theta_2 + m\cdot\sigma(\omega)/\varepsilon_0 c}\right|^2,$$
$$T = \left|\frac{E_s}{E_i}\right|^2 \cdot \frac{n_2\cos\theta_2}{n_1\cos\theta_1} = \frac{4n_1 n_2\cos\theta_1\cos\theta_2}{\left|n_1\cos\theta_1 + n_2\cos\theta_2 + m\cdot\sigma(\omega)/\varepsilon_0 c\right|^2}, \quad (2.9)$$

The absorbance (A) can be considered by $A = 1 - T - R$ because of the energy conservation.

$$A = \frac{4n_1\cos\theta_2 m\cdot\mathrm{Re}[\sigma(\omega)]\cos\theta_1\cos\theta_2/\varepsilon_0 c}{\left|n_2\cos\theta_1 + n_1\cos\theta_2 + m\cdot\sigma(\omega)\cos\theta_1\cos\theta_2/\varepsilon_0 c\right|^2}$$
$$A = \frac{4n_1\cos\theta_1 m\cdot\mathrm{Re}[\sigma(\omega)]/\varepsilon_0 c}{\left|n_1\cos\theta_1 + n_2\cos\theta_2 + m\cdot\sigma(\omega)/\varepsilon_0 c\right|^2} \quad (2.10)$$

for *p*- and *s*-polarization, respectively.

It can be seen that the real part of the optical conductivity contributes to absorption primarily, whereas the imaginary part will result in a phase shift. In Equations (2.8–2.10), m is the number of layers in the graphene sheet. The m layers of graphene are considered to be interlayer uncoupled, and hence can be treated approximately as linear superposition.[13, 36, 37] When $m = 0$, the above equations degenerate to the well-documented simple (nonconducting) interface situation.

The optical conductivity of graphene is a complex number given by the sum of the interband conductivity $\sigma_{inter}(\omega)$ and the intraband conductivity $\sigma_{intra}(\omega)$, which are given by [4, 38-41]:

$$\sigma_{inter}(\omega) = i\frac{e^2\omega}{\pi}\int_0^\infty d\varepsilon \frac{1}{(2\varepsilon)^2 - (\hbar\omega + i\Gamma)^2}[f(\varepsilon - E_f^c) - f(-\varepsilon - E_f^v)], \quad (2.11)$$

$$\sigma_{intra}(\omega) = i\frac{e^2/\pi\hbar^2}{\omega + i/\tau}K_B T_e \cdot Log[(e^{E_f^c/K_B T_e} + 1)(e^{-E_f^v/K_B T_e} + 1)], \quad (2.12)$$

where e is the electron charge, $\hbar\omega$ is the photon energy, $f(\varepsilon - E_f^{c/v})$ is the Fermi distribution function with the Fermi energy $E_f^{c/v}$ for the conduction/valence band, Γ describes the broadening of the interband transitions, K_B is the Boltzmann constant, T_e is the electronic temperature, and τ is the intra-momentum relaxation time due to c-c scattering.

If we consider a freestanding monolayer graphene under low intensity normal incidence, the following values should be taken: $n_1 = n_2 = 1$, $m = 1$, $\theta_1 = 0$ and $E_f^{c/v} \approx 0$. The electronic temperature is considered to be ~ 300 K, and the parameters (Γ, τ) are taken from published literature: Γ = 12 meV [28, 41] and τ = 10 fs [27, 41]. We have also used the ranges of Γ = 6 ~ 30 meV [28] and τ = 10 ~ 50 fs [41] to calculate the conductivity. The results variation is quite insignificant (less than 5%), indicating that the conductivity is insensitive to the values in the ranges. The linear optical conductivities at optical-near infrared (NIR) wavelengths are calculated to be almost constant $\sigma(\omega) = \sigma_0 \approx e^2/4\hbar$ [31, 32, 39, 42-45], as depicted in the inset of Figure 2.4. Subsequently, we obtain the universal linear absorbance of monolayer graphene

$$A = \frac{\sigma_0 / \varepsilon_0 c}{\left|1 + \sigma_0 / 2\varepsilon_0 c\right|^2} = \frac{\pi\alpha}{(1 + \pi\alpha/2)^2} \simeq \pi\alpha \,, \tag{2.13}$$

where $\alpha = e^2 / 4\pi\epsilon_0 c\hbar$ is the fine-structure constant. The linear absorbance of monolayer graphene calculated by Equation (2.13) is consistent with many experiments [30, 31, 46] and the theory derived from Fermi's Golden Rule[30]. Additionally, comparison between our theoretical computation and the experimental transmittance data [30] is shown in Figure

2.4. The agreements validate the reliability of the above-derived absorbance formulas. When the wavelength decreases to < 450 nm, the computation starts to deviate from the experiment, which might partially result from the fact that the linear energy dispersion relation becomes invalid at shorter wavelengths.

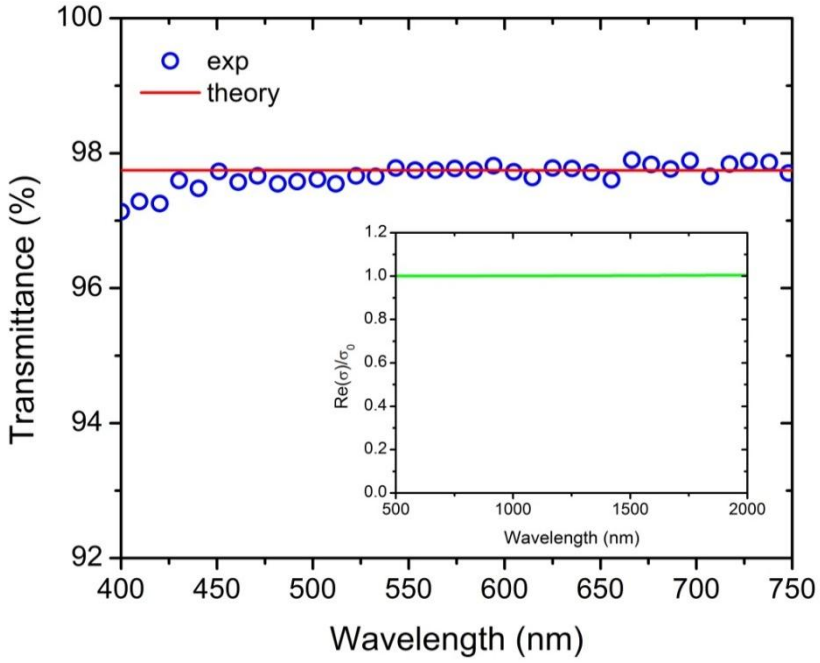

Figure 2.4 Comparison between the theory and the experimental transmittance data in Ref 30 at various wavelengths. Inset: Universal linear optical conductivity for monolayer graphene.

However, when encountering with higher light intensities, the large photoexcited temporal populations of carriers in the conduction and valence bands block further absorption of incoming photons at the same energy (within the pulse duration), giving rise to a bleaching effect as increased transmittance and manifests a saturable absorption

property. Thus, the optical response of graphene evolves itself from linear to nonlinear behaviors, which will be discussed in the following Section.

2.3.2 Saturable absorption in graphene

In order to evaluate the nonlinear transmittance and reflectance, it is necessary to know the optical conductivity in Equations (2.11) and (2.12) as a function of the incident light intensity that is proportional to $|E_i|^2$. To achieve it, we develop a photodynamic model to simulate the relation between the Fermi energy and the photoexcited carrier density that is related to the incident light intensity. The model is detailed as follows.

Immediately following photoexcitation by an ultrashort laser pulse, electrons (holes) are in a nonthermal distribution with a large population near $\pm h\nu/2$ from the band edge. Meanwhile, the conduction carriers due to doping or thermal excitation at room temperature might be excited to higher energy states through intraband transition, as shown in Figure 2.5(a).

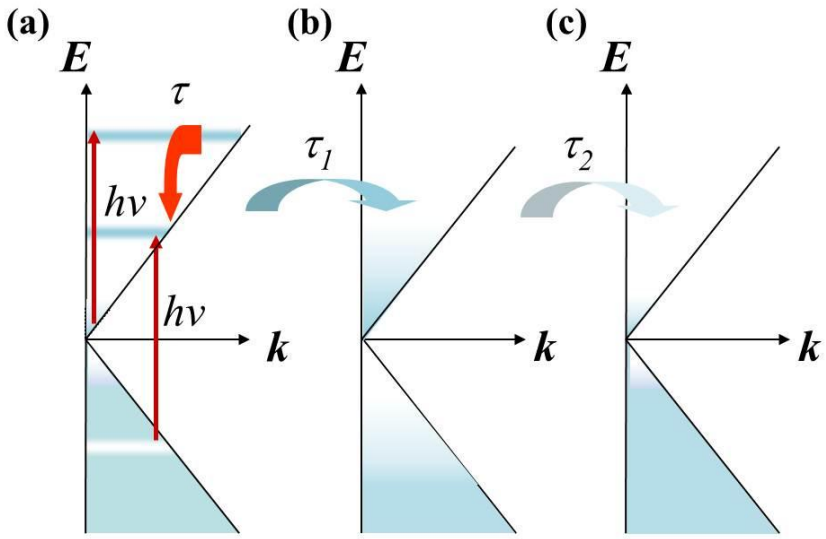

Figure 2.5 Schematic diagrams for photodynamics: (a) carrier excitation by interband and intraband transitions; (b) quasi-equilibrium after c-c scattering; and (c) equilibrium after carrier relaxation through c-p scattering or electron-hole recombination.

Afterwards, we consider the ultrafast intraband carrier thermalization to form quasi-equilibration (dominated by the intraband c-c scattering) in the absence of energy dissipation. Within extremely fast time scale of ~ 10 fs [11, 27], separate Fermi-Dirac distributions [Figure 2.5(b)] can be established at ultra-high temperatures (T_0) with different Fermi levels ($E^0_{fc/v}$). The dependence of the initial electron temperature T_0 on the electron density N can be computed according to the following conditions of particle number and energy conservation [26, 27]. Note that for linear dispersion near the Dirac point, pair c-c scattering cannot lead to interband relaxation, thereby conserving the carrier densities and the total energy:

$$N = 4\int f(\varepsilon - E_{fc}^{0}) d^{2}\mathbf{k} / (2\pi)^{2} \tag{2.14a}$$

$$Nh\nu / 2 = 4\int \varepsilon f(\varepsilon - E_{fc}^{0}) d^{2}\mathbf{k} / (2\pi)^{2} \tag{2.14b}$$

where $f(\varepsilon - E_{fc}^{0})$ is the Fermi distribution function with the Fermi energy E_{fc}^{0} for the conduction band. As an example, we displays in Figure 2.6 the relationship of $T_0 \sim N$ in monolayer graphene at 780 nm excitation, which is similar to Fig. 3 in Ref 27. The dependence of T_0 on N at other photoexcitation wavelengths, from visible to NIR, is also computed, respectively.

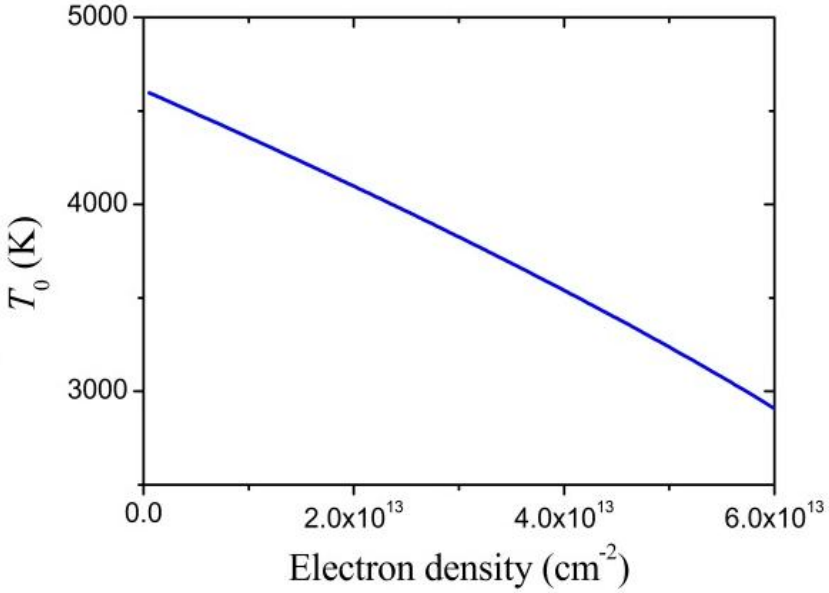

Figure 2.6 Dependence of the initial electron temperature T_0 on the electron density N in monolayer graphene at 780 nm excitation.

For a given N, the corresponding elevated initial electron temperature T_0, which is much higher than the lattice temperature, decreases in time during further phonon-mediated carrier cooling. Note that for the symmetric band structure of Figure 2.5(a)

and similar cooling rates of electrons and holes, the temperature for electrons and holes are identical at all times [11].The energy relaxation of electrons has been investigated both experimentally [6, 11] and theoretically [7, 47]. Figure 2.7 (re-produced from Ref 11) shows the temporal evolution of carrier temperature $T_e(t)$ at a particular electron density, which can be expressed by a bi-exponential decay modeling:

$$T_e(t) = T_0 * (B_1 e^{-t/\mu_1} + B_2 e^{-t/\mu_2}) \tag{2.15}$$

with B_1=0.761, B_2=0.239, μ_1=100 fs, and μ_2=10 ps. Here, it was assumed that the Fermi-Dirac distributions forms instantaneously, *i.e.* at t = 0, T_e= T_0. The parameters in the fitting results (B_1=0.761, B_2=0.239, μ_1=100 fs, and μ_2=10 ps) are proximately consistent with a wide range of reports of photoexcited electron relaxation processes in graphene [8, 10-19, 21, 23].

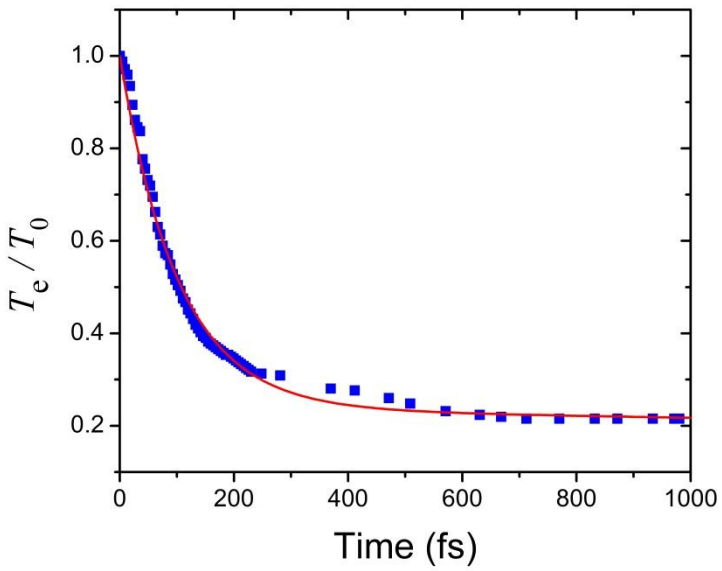

Figure 2.7 Temporal evolution of carrier temperature reported in Ref. 11 (blue squares). The red curve is the bi-exponential fit as discussed in the text.

To reduce numerical efforts, a time-averaged electron temperature during the lifetime of the excited carriers was assumed as the effective electron temperature T_{eff}.[26]

$$T_{eff} = \frac{\int_0^{\tau_2} T_e(t)dt}{\int_0^{\tau_2} dt} \tag{2.16}$$

Noting that here we only consider a situation where the pulse duration is longer than c-c relaxation time, so during the pulse the carriers are assumed to quasi-equilibrate at a quasi-steady state with an effective temperature T_{eff}.[26]

It should be pointed out that in Ref 11 the experiment was carried on 20~30 nm thick freestanding exfoliated graphite film. The electron temperature evolution of epitaxial and CVD graphene on a substrate might be different because of the unintentional doping in growth process and the interaction with the substrate. Moreover, the decay parameters might vary for different N and λ. However, due to the shortage of more updated and precise results on the related parameters, the data reported in Ref 11 was still cited in the theoretical works in this thesis, without considering the effect of N and λ, which would be a shortcoming of our model.

As electron temperature T_e decreases, the conservation of carrier density throughout the equilibration process forces Fermi level to increase with time [11, 47]. Thus, since the effective temperature T_{eff} was computed, the effective Fermi level $E_{fc/v}^{eff}$ was computed correspondingly to preserve the electron density:

$$N = 4\int f(\varepsilon - E_{fc}^{eff}) d^2\mathbf{k} / (2\pi)^2,$$
$$f(\varepsilon - E_{fc}^{eff}) = [1 + \exp(\frac{\varepsilon - E_{fc}^{eff}}{K_B T_{eff}})]^{-1} \quad (2.17)$$

Subsequently, the optical conductivity as a function of the electron densities would be computed by Equations (2.11) and (2.12) using the above obtained parameters $E_{fc/v}^{eff}$ and T_{eff}.

T, *R* and *A* as a function of the electron densities would be computed correspondingly by Equations (2.8 - 2.10). Similarly, the optical response under different wavelengths could also be calculated by the above-discussed procedures.

The photoexcited hot charge carriers disappear when electron-hole recombination subsequently dominates the relaxation process and the room-temperature-equilibrium carrier distribution is restored [Figure 2.5(c)]. This relaxation process can be characterized with a time constant τ_2 around a few picoseconds [8, 10, 11, 13, 14, 21].

In order to depict the relationship between the photoexcited carrier density and the incident light intensity, the following approximation has been made.

The photoexcited charge carriers $\Delta N(t)$ can be approximated by [48, 49]

$$\frac{d\Delta N(t)}{dt} = \frac{A_{inter} I_i(t)}{\hbar\omega} - \frac{\Delta N(t)}{\tau_2}, \quad (2.18)$$

with A_{inter} be the absorbance contributed from interband photoexcitation only, since the intraband photoexcitation does not contribute to the carrier density variation. The incident laser pulse is considered to possess a Gaussian temporal profile

$I_i(t) = I_0 \exp(-t^2 / {\tau_G}^2)$, with τ_G being the half width at 1/e maximum and τ_L being the full width at half maximum, $\tau_G = \tau_L / 2\sqrt{\ln 2}$. In experiment, the measured transmittance/reflectance is the fraction of incident light that passes through/reflected from a sample which is the time-averaged transmitted/reflected fraction of the total incident power over the pulse duration. Thereby in our computation, a Gaussian pulse that is characterized by the on-axis intensity I_0 is considered as a whole. Although the light intensity I_i(t) varies with time, the absorbance A during a pulse is taken as a phenomenological constant that determined by the on-axis intensity I_0. In other words, during a pulse the electrons are assumed to be excited at a phenomenological constant rate, which agrees with the previous report [26].

By solving Equation (2.18), ΔN(t) can be written as

$$\Delta N(t) = \frac{A_{inter}}{\hbar\omega} \int_{-\infty}^{t} I_i(t') \exp(\frac{t'-t}{\tau_2}) dt' \tag{2.19}$$

Under the time-averaging approximation, the time-averaged totally accumulated photoexcited electron density (ΔN) in quasi-equilibrium can be approximately written by [49]

$$\Delta N = \frac{\int_{-\infty}^{+\infty} \Delta N(t) I_i(t) dt}{\int_{-\infty}^{+\infty} I_i(t) dt} \tag{2.20}$$

Accordingly, we obtain the accumulated photoexcited electron density by inserting Equation (2.19) into Equation (2.20) as follows

$$\Delta N = \frac{A_{inter} I_0}{\hbar\omega} f(\tau_L, \tau_2),$$
$$f(\tau_L, \tau_2) = \frac{1}{\sqrt{\pi}\tau_G} \int_{-\infty}^{+\infty} \exp(-\frac{t^2}{{\tau_G}^2}) \left[\int_{-\infty}^{t} \exp(-\frac{t'^2}{{\tau_G}^2}) \exp(\frac{t'-t}{\tau_2}) dt' \right] dt, \quad (2.21)$$

ΔN correlates with the persistent electron density (N) in Equation (2.14) by $N = \Delta N + N_0$, where N_0 is the original charge carrier concentration due to doping or thermal excitation at room temperature. A_{inter} is the previous computed interband absorbance which is related with the carrier density.

By solving Equation (2.21), the optical conductivity (σ), transmittance (T), reflectance (R) and absorbance (A) are expressed as a function of the on-axis laser pulse intensity (I_0).

2.4 Summary

In this chapter, the experimental observations on the ultrafast carrier dynamics in graphene are reviewed and summarized firstly. Then, existing theoretical understanding on saturable absorption of graphene is comprehensively reviewed based on the above-discussed experimental evidence. Finally, our mathematical considerations are given for the saturable absorption of graphene. The computation strategy in our simulation is summarized in Figure 2.8.

As displayed in Figure 2.8, our model is based on a set of assumptions. First, the linear energy dispersion relation and interlayer uncoupled multilayer graphene are considered. Second, an excited electron temperature evolution is assumed based on an

experimental observation. This excited temperature evolution is assumed to be independent of the excitation laser intensity and wavelengths. Third, the carrier recombination time is assumed to be greater than the excitation pulse duration. Last, time-averaging approximations are taken for photoexcited carrier density and photoexcited electron temperature. These points still require further improvements and special optimizations.

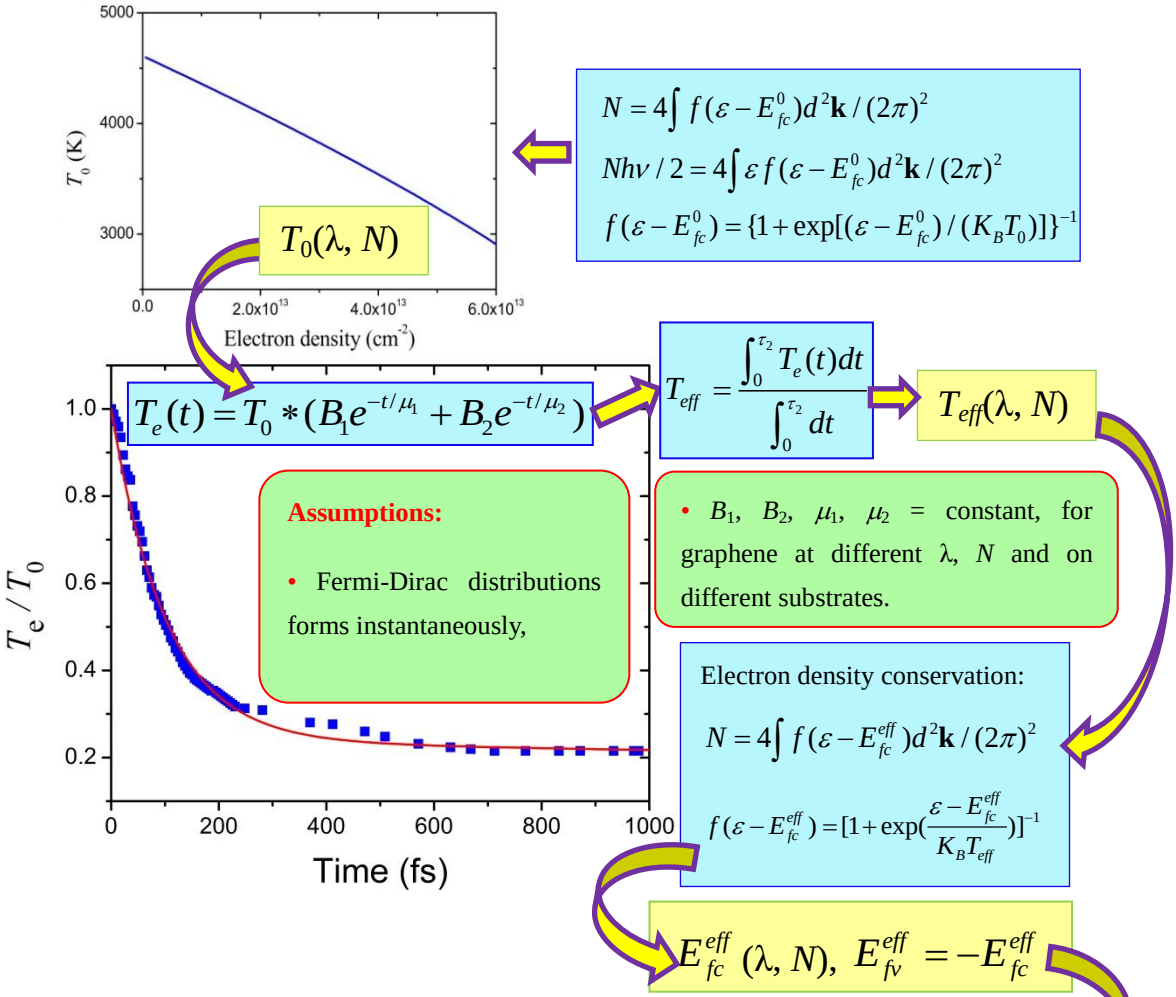

Figure 2.8 Flow chart of our mathematical model.

References:

1. Bonaccorso, F.; Sun, Z.; Hasan, T.; Ferrari, A. C., Graphene photonics and optoelectronics. *Nat. Photonics* **2010**, 4, 611.

2. Xia, F. N.; Mueller, T.; Lin, Y. M.; Valdes-Garcia, A.; Avouris, P., Ultrafast graphene photodetector. *Nat. Nanotechnol.* **2009**, 4, 839.

3. Bao, Q. L.; Zhang, H.; Ni, Z. H.; Wang, Y.; Polavarapu, L.; Shen, Z. X.; Xu, Q. H.; Tang, D. Y.; Loh, K. P., Monolayer graphene as a saturable absorber in a mode-locked laser. *Nano Res.* **2011**, 4, 297.

4. Rana, F., Graphene terahertz plasmon oscillators. *IEEE Trans. Nanotechnol.* **2008**, 7, 91.

5. Seibert, K.; Cho, G. C.; Kutt, W.; Kurz, H.; Reitze, D. H.; Dadap, J. I.; Ahn, H.; Downer, M. C.; Malvezzi, A. M., Femtosecond carrier dynamics in graphite. *Phys. Rev. B* **1990**, 42, 2842.

6. Kampfrath, T.; Perfetti, L.; Schapper, F.; Frischkorn, C.; Wolf, M., Strongly coupled optical phonons in the ultrafast dynamics of the electronic energy and current relaxation in graphite. *Phys. Rev. Lett.* **2005**, 95, 187403.

7. Butscher, S.; Milde, F.; Hirtschulz, M.; Malic, E.; Knorr, A., Hot electron relaxation and phonon dynamics in graphene. *Appl. Phys. Lett.* **2007**, 91, 203103.

8. Dawlaty, J. M.; Shivaraman, S.; Chandrashekhar, M.; Rana, F.; Spencer, M. G., Measurement of ultrafast carrier dynamics in epitaxial graphene. *Appl. Phys. Lett.* **2008**, 92, 042116.

9. Sun, D.; Wu, Z. K.; Divin, C.; Li, X. B.; Berger, C.; de Heer, W. A.; First, P. N.; Norris, T. B., Ultrafast relaxation of excited dirac fermions in epitaxial graphene using optical differential transmission spectroscopy. *Phys. Rev. Lett.* **2008**, 101, 157402.

10. George, P. A.; Strait, J.; Dawlaty, J.; Shivaraman, S.; Chandrashekhar, M.; Rana, F.; Spencer, M. G., Ultrafast optical-pump terahertz-probe spectroscopy of the carrier relaxation and recombination dynamics in epitaxial graphene. *Nano Lett.* **2008**, 8, 4248.

11. Breusing, M.; Ropers, C.; Elsaesser, T., Ultrafast carrier dynamics in graphite. *Phys. Rev. Lett.* **2009**, 102, 086809.

12. Choi, H.; Borondics, F.; Siegel, D. A.; Zhou, S. Y.; Martin, M. C.; Lanzara, A.; Kaindl, R. A., Broadband electromagnetic response and ultrafast dynamics of few-layer epitaxial graphene. *Appl. Phys. Lett.* **2009**, 94.

13. Newson, R. W.; Dean, J.; Schmidt, B.; van Driel, H. M., Ultrafast carrier kinetics in exfoliated graphene and thin graphite films. *Opt. Express* **2009**, 17, 2326.

14. Huang, L. B.; Hartland, G. V.; Chu, L. Q.; Luxmi; Feenstra, R. M.; Lian, C. X.;

Tahy, K.; Xing, H. L., Ultrafast transient absorption microscopy studies of carrier dynamics in epitaxial graphene. *Nano Lett.* **2010**, 10, 1308.

15. Shang, J.; Luo, Z.; Cong, C.; Lin, J.; Yu, T.; Gurzadyan, G. G., Femtosecond UV-pump/visible-probe measurements of carrier dynamics in stacked graphene films. *Appl. Phys. Lett.* **2010**, 97, 163103.

16. Wang, H. N.; Strait, J. H.; George, P. A.; Shivaraman, S.; Shields, V. B.; Chandrashekhar, M.; Hwang, J.; Rana, F.; Spencer, M. G.; Ruiz-Vargas, C. S.; Park, J., Ultrafast relaxation dynamics of hot optical phonons in graphene. *Appl. Phys. Lett.* **2010**, 96, 081917.

17. Zou, X. Q.; Zhan, D.; Fan, X. F.; Lee, D.; Nair, S. K.; Sun, L.; Ni, Z. H.; Luo, Z. Q.; Liu, L.; Yu, T.; Shen, Z. X.; Chia, E. E. M., Ultrafast carrier dynamics in pristine and $FeCl_3$-intercalated bilayer graphene. *Appl. Phys. Lett.* **2010**, 97, 141910.

18. Breusing, M.; Kuehn, S.; Winzer, T.; Malic, E.; Milde, F.; Severin, N.; Rabe, J. P.; Ropers, C.; Knorr, A.; Elsaesser, T., Ultrafast nonequilibrium carrier dynamics in a single graphene layer. *Phys. Rev. B* **2011**, 83, 153410.

19. Huang, L. B.; Gao, B.; Hartland, G.; Kelly, M.; Xing, H. L., Ultrafast relaxation of hot optical phonons in monolayer and multilayer graphene on different substrates. *Surf. Sci.* **2011**, 605, 1657.

20. Obraztsov, P. A.; Rybin, M. G.; Tyurnina, A. V.; Garnov, S. V.; Obraztsova, E. D.; Obraztsov, A. N.; Svirko, Y. P., Broadband light-induced absorbance change in multilayer graphene. *Nano Lett.* **2011**, 11, 1540.

21. Shang, J. Z.; Yu, T.; Lin, J. Y.; Gurzadyan, G. G., Ultrafast electron-optical phonon scattering and quasiparticle lifetime in CVD-grown graphene. *Acs Nano* **2011**, 5, 3278.

22. Strait, J. H.; Wang, H.; Shivaraman, S.; Shields, V.; Spencer, M.; Rana, F., Very slow cooling dynamics of photoexcited carriers in graphene observed by optical-pump terahertz-probe spectroscopy. *Nano Lett.* **2011**, 11, 4902.

23. Yee, K. J.; Kim, J. H.; Jung, M. H.; Hong, B. H.; Kong, K. J., Ultrafast modulation of optical transitions in monolayer and multilayer graphene. *Carbon* **2011**, 49, 4781.

24. Romanets, P. N.; Vasko, F. T., Transient response of intrinsic graphene under ultrafast interband excitation. *Phys. Rev. B* **2010**, 81, 085421.

25. Rana, F.; Strait, J. H.; Wang, H. N.; Manolatou, C., Ultrafast carrier recombination and generation rates for plasmon emission and absorption in graphene. *Phys. Rev. B* **2011**, 84, 045437.

26. Sun, Z. P.; Hasan, T.; Torrisi, F.; Popa, D.; Privitera, G.; Wang, F. Q.; Bonaccorso, F.; Basko, D. M.; Ferrari, A. C., Graphene mode-locked ultrafast laser. *Acs*

Nano **2010**, 4, 803.

27. Xing, G.; Guo, H.; Zhang, X.; Sum, T. C.; Huan, C. H. A., The physics of ultrafast saturable absorption in graphene. *Opt. Express* **2010**, 18, 4564.

28. Vasko, F. T., Saturation of interband absorption in graphene. *Phys. Rev. B* **2010**, 82, 245422.

29. Zhang, Z.; Voss, P. L., Full-band quantum-dynamical theory of saturation and four-wave mixing in graphene. *Opt. Lett.* **2011**, 36, 4569.

30. Nair, R. R.; Blake, P.; Grigorenko, A. N.; Novoselov, K. S.; Booth, T. J.; Stauber, T.; Peres, N. M. R.; Geim, A. K., Fine structure constant defines visual transparency of graphene. *Science* **2008**, 320, 1308.

31. Mak, K. F.; Sfeir, M. Y.; Wu, Y.; Lui, C. H.; Misewich, J. A.; Heinz, T. F., Measurement of the optical conductivity of graphene. *Phys. Rev. Lett.* **2008**, 101, 196405.

32. Stauber, T.; Peres, N. M. R.; Geim, A. K., Optical conductivity of graphene in the visible region of the spectrum. *Phys. Rev. B* **2008**, 78, 085432.

33. Falkovsky, L. A.; Pershoguba, S. S., Optical far-infrared properties of a graphene monolayer and multilayer. *Phys. Rev. B* **2007**, 76, 153410.

34. Falkovsky, L. A., Optical properties of graphene and IV-VI semiconductors. *Physics-Uspekhi* **2008**, 51, 887.

35. Falkovsky, L. A.; Varlamov, A. A., Space-time dispersion of graphene conductivity. *European Physical Journal B* **2007**, 56, 281.

36. Hass, J.; Varchon, F.; Mill; aacute; n-Otoya, J. E.; Sprinkle, M.; Sharma, N.; de Heer, W. A.; Berger, C.; First, P. N.; Magaud, L.; Conrad, E. H., Why multilayer graphene on 4H-SiC(000-1) behaves like a single sheet of graphene. *Phys. Rev. Lett.* **2008**, 100, 125504.

37. Sadowski, M. L.; Martinez, G.; Potemski, M.; Berger, C.; de Heer, W. A., Landau level spectroscopy of ultrathin graphite layers. *Phys. Rev. Lett.* **2006**, 97, 266405.

38. Gusynin, V. P.; Sharapov, S. G.; Carbotte, J. P., Unusual microwave response of dirac quasiparticles in graphene. *Phys. Rev. Lett.* **2006**, 96, 256802.

39. Gusynin, V. P.; Sharapov, S. G.; Carbotte, J. P., Magneto-optical conductivity in graphene. *J. Phys.: Condens. Matter* **2007**, 19, 026222.

40. Peres, N. M. R.; Guinea, F.; Neto, A. H. C., Electronic properties of disordered two-dimensional carbon. *Phys. Rev. B* **2006**, 73, 125411.

41. Dawlaty, J. M.; Shivaraman, S.; Strait, J.; George, P.; Chandrashekhar, M.; Rana,

F.; Spencer, M. G.; Veksler, D.; Chen, Y. Q., Measurement of the optical absorption spectra of epitaxial graphene from terahertz to visible. *Appl. Phys. Lett.* **2008**, 93, 131905.

42. Peres, N. M. R.; Stauber, T.; Neto, A. H. C., The infrared conductivity of graphene on top of silicon oxide. *Epl* **2008**, 84, 38002.

43. Falkovsky, L. A., Universal infrared conductivity of graphite. *Phys. Rev. B* **2010**, 82, 073103.

44. Stauber, T.; Peres, N. M. R.; Net, A. H. C., Conductivity of suspended and non-suspended graphene at finite gate voltage. *Phys. Rev. B* **2008**, 78, 085418.

45. Kuzmenko, A. B.; van Heumen, E.; Carbone, F.; van der Marel, D., Universal optical conductance of graphite. *Phys. Rev. Lett.* **2008**, 100, 117401.

46. Wang, F.; Zhang, Y.; Tian, C.; Girit, C.; Zettl, A.; Crommie, M.; Shen, Y. R., Gate-variable optical transitions in graphene. *Science* **2008**, 320, 206.

47. Bistritzer, R.; MacDonald, A. H., Electronic cooling in graphene. *Phys. Rev. Lett.* **2009**, 102, 206410.

48. Gu, B.; He, J.; Ji, W.; Wang, H. T., Three-photon absorption saturation in ZnO and ZnS crystals. *J. Appl. Phys.* **2008**, 103, 073105.

49. Gu, B.; Sun, Y.; Ji, W., Two-photon-induced excited-state nonlinearities. *Opt. Express* **2008**, 16, 17745.

Chapter 3

Z-scan measurements on saturable absorption in epitaxial graphene

To determine saturable absorption in graphene, we have conducted both transmission open-aperture Z-scan measurement (TZ-scan) and reflection open-aperture Z-scan measurements (RZ-scan) on epitaxial graphene. The Z-scan techniques were used because they are not only a straightforward method, but also an accurate technique for characterization of saturable absorption. It was first introduced and theoretically modeled in 1990 by Sheik-Bahae and his colleagues [1]. Since then, it has been widely employed as a standard technique to characterize various nonlinear optical properties. In general, the Z-scan measurement is based on the transformation of phase distortion to amplitude variation during the laser beam propagation. In experiments, we record the far field energy transmittance as the sample is moved along the z direction through the focal plane of the Gaussian beam. Further detailed information about the Z-scan technique is elaborated in the following section.

The details on the growth and characterization of epitaxial samples used here can be found elsewhere [2-12]. Briefly, three samples have been studied: (1) mono-; (2) bi-; and (3) six- layer graphene on silicon carbide (SiC) substrate. Figure 3.1 shows the measured linear absorption spectra of the three samples with the Shimadzu (UV-3600) UV-VIS-

NIR Spectrophotometer and their comparison with the theory are presented in Section 2.3.1. In the spectral range of interest (780 nm ~ 1100 nm), the measurements are in agreement with the theory within the variation of 0.25%, 1.5% and 3% for the mono-, bi- and six-layer graphene samples, respectively.

This Chapter is organized in the following way. Section 3.1 introduces both lasers and operational principles of Z-scan measurements. The Z-scan data measured at 780 nm and determination of saturation intensity are presented in Sections 3.2 and 3.3, respectively. In Section 3.4, the measurements on the spectral dependence of saturation intensity are reported, followed by a summary in Section 3.5

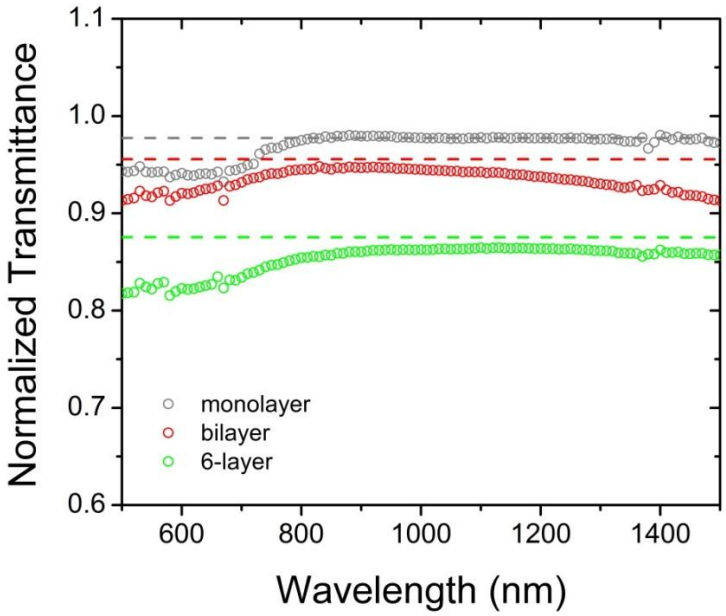

Figure 3.1 Normalized transmittance spectra of mono-, bi- and six-layer graphene samples (circles). The transmittance of graphene samples are normalized by the transmittance through the bare SiC wafer. The dashed lines are the theoretical estimations.

3.1 Operational principle of Z-scan measurements

Two femtosecond laser systems were employed in the above-mentioned saturable absorption measurements. (i) 1 kHz-repetition-rate, 400-fs (FWHM) and 780-nm-wavelength laser pulses were provided by a Ti:Sapphire regenerative amplifier (Quantronix, Titan). The amplifier was seeded by a pump laser at 527 nm, with pulse duration of 150 ns and repetition rate of 1KHz (Qantronix, Darwin). (ii) The second femtosecond laser system was composed of an optical parametric amplifier (Coherent TOPAZ) pumped by a Coherent regenerative amplifier (Coherent Legend, 780 nm, 200-fs pulse duration, 1 kHz repetition rate). The TOPAZ generated tunable wavelength laser pulses from 500 nm to 1550 nm.

3.1.1 Focused Gaussian laser beam [13]

In laser optics, Gaussian beam is widely used to study the nonlinear optical properties and ultrafast dynamics, whose intensity (irradiance) distributions and transverse electric field can be well approximated by Gaussian functions. Lasers operating on the TEM_{00} mode of the laser's optical resonator emit beams that approximate a Gaussian profile. The output laser pulses are usually focused by an optical focal lens to achieve the desired high laser intensity and small excitation volume. The mathematical function that describes the focused Gaussian laser beam, which represents the complex amplitude of the beam's electric field, can be expressed as:

$$E(r,z,t) = \hat{e}\,A(r,t)\frac{w_0}{w(z)}\exp\{i[kz - \tan^{-1}(\frac{z}{z_0}) - \omega t + \frac{kr^2}{2q(z)}]\} + c.c. \quad (3.1)$$

where $\hat{e}$ is the polarization unit vector of the wave, $r = (x^2 + y^2)^{1/2}$ is the radial coordinate from the center axis of the beam, z is the axial distance from the beam's narrowest point (the "waist"), i is the imaginary unit, k is the wave vector of the propagation and ω is the circular frequency of the rapidly oscillating wave. $A(r, t)$ is the space and time dependent wave amplitude. $q(z) = z - iz_0$ is the complex radius of wave front curvature. $w(z)$ is the variable beam radius defined as the half-width of the Gaussian curve, at which the field amplitude drop to $1/e$ of its axial values. $2w_0$ is defined as the beam waist, which is the minimum beam diameter at $z = 0$. The notation "c.c." implies complex conjugate. The relationship between $w(z)$ and w_0 is given by

$$w(z) = w_0[1 + (\frac{z}{z_0})^2]^{1/2} \quad (3.2)$$

z_0 is called the Rayleigh range and is defined by

$$z_0 = \frac{\pi w_0^{\,2}}{\lambda} \quad (3.3)$$

where λ is the optical wavelength in free space. The distance between the points $\pm z_0$ is called the confocal parameter b ($b = 2z_0$) as illustrated in Figure 3.2

The corresponding time-averaged intensity (or irradiance) distribution can be simplified as

$$I(r,z,t) = I_{00}(\frac{w_0}{w(z)})^2 \exp(-\frac{2r^2}{w^2(z)})\exp(-\frac{t^2}{\tau_p^2}) \quad (3.4)$$

I_{00} is the on-axis peak irradiance at focus point and τ_p is the pulse duration.

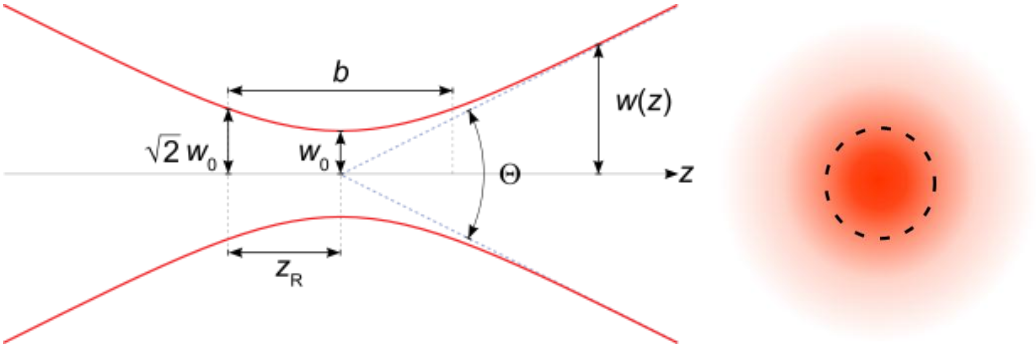

Figure 3.2 Schematic diagram of a Gaussian laser beam propagation and cross section profile. [13, 14]

3.1.2 Transmission and reflection open-aperture Z-scan techniques

The Z-scan technique is based on the variation of light intensity during the beam propagation. In the TZ-scan, the energy transmittance (*T*) of the far field through the sample is recorded as the sample is scanned or moved along the axis of propagation (*z*) of a focused laser beam through its focal plane. As the sample experiences different electric field strengths with changing *z* positions, the recording of the transmission as a function of the *z* coordinate provides accurate information about the nonlinear effects existing in the sample. The experimental set-up for standard Z-scan is schematically depicted in Figure 3.3(a).

The incoming beam is split by a beam splitter, the reflected portion of which is recorded by detector D_0, as a reference to eliminate the fluctuation in the pulse energy. The transmitted portion of beam is focused by a convex lens and incident on the sample. The power of the light transmitted through the sample is measured by the detector D_1 or

D_2. Two types of Z-scan are usually conducted: open-aperture Z-scan (OA Z-scan) and closed aperture Z-scan (CA Z-scan). OA Z-scan is used to determine the magnitude of nonlinear absorption in the sample, in which the entire energy transmitted through the sample is collected with a focus lens and directed to detector D_2. While CA Z-scan is used to determine the magnitude of nonlinear refraction in the sample, in which a small pinhole is placed in the far field before the detector (D_1). As illustrated in Figure 3.3(a), the magnitude of the nonlinearity can be derived from the energy ratio D_2 (or D_1) to D_0 as a function of the sample position *z* (relative to the focal plan). In this study, OA Z-scan was used to investigate the saturable absorption of graphene.

The Z-scan experiment can also be conducted in the configuration of RZ-scan, in which the reflected beam energy from the sample was collected by a detector D_1, as shown in Figure 3.3(b). At higher laser irradiance, the reflectance from the sample is altered due to the nonlinear reflectivity of the sample.

In the Z-scan experiments, the thickness of the sample should be much smaller than the Rayleigh range of the focused beam $l << z_0 = \pi w_0^2 / \lambda$. It is because in such "thin" medium, the changes in the beam diameter across the sample caused by the nonlinear refraction or diffraction can be neglected.

Typically, the OA Z-scan data is analyzed by solving the propagation deferential equation. For the beam propagate in a thin homogeneous saturable absorber, the laser intensity evolved can be evaluated by the following differential equation:

$$dI / dz' = -f(I) = -\alpha(I)I = -\alpha_0 I / (1 + I / I_s) \tag{3.5}$$

where α_0 and I_s are the linear absorption coefficient and saturation intensity, respectively. By formally integrating Equation (3.5) over z', the irradiance at the exit surface of the sample I^{out} is written as:

$$I^{out} = I^{in} - \int_0^L f(I)dz' \tag{3.6}$$

where I^{in} is the input laser intensity at the entrance face of the sample and L is the sample thickness.

Generally, it is difficult to obtain explicit analytical solutions of the laser beam transmitting through a saturable absorber. However, the calculation can be conducted on the basis of the AD method, which has been thoroughly demonstrated in Ref 14-16. Thereafter, the transmittance as a function of sample position z becomes,

$$T(z) = \frac{\int_0^\infty I^{out}(z,r,t)rdrdt}{e^{-\alpha_0 L}\int_0^\infty I^{in}(z,r,t)rdrdt} \tag{3.7}$$

Consequently, the characteristic parameter of a saturable absorber, I_s can be extracted by fitting the OA Z-scan experiment data with Equations (3.1)-(3.7), as shown by the solid curves in Figure 3.4.

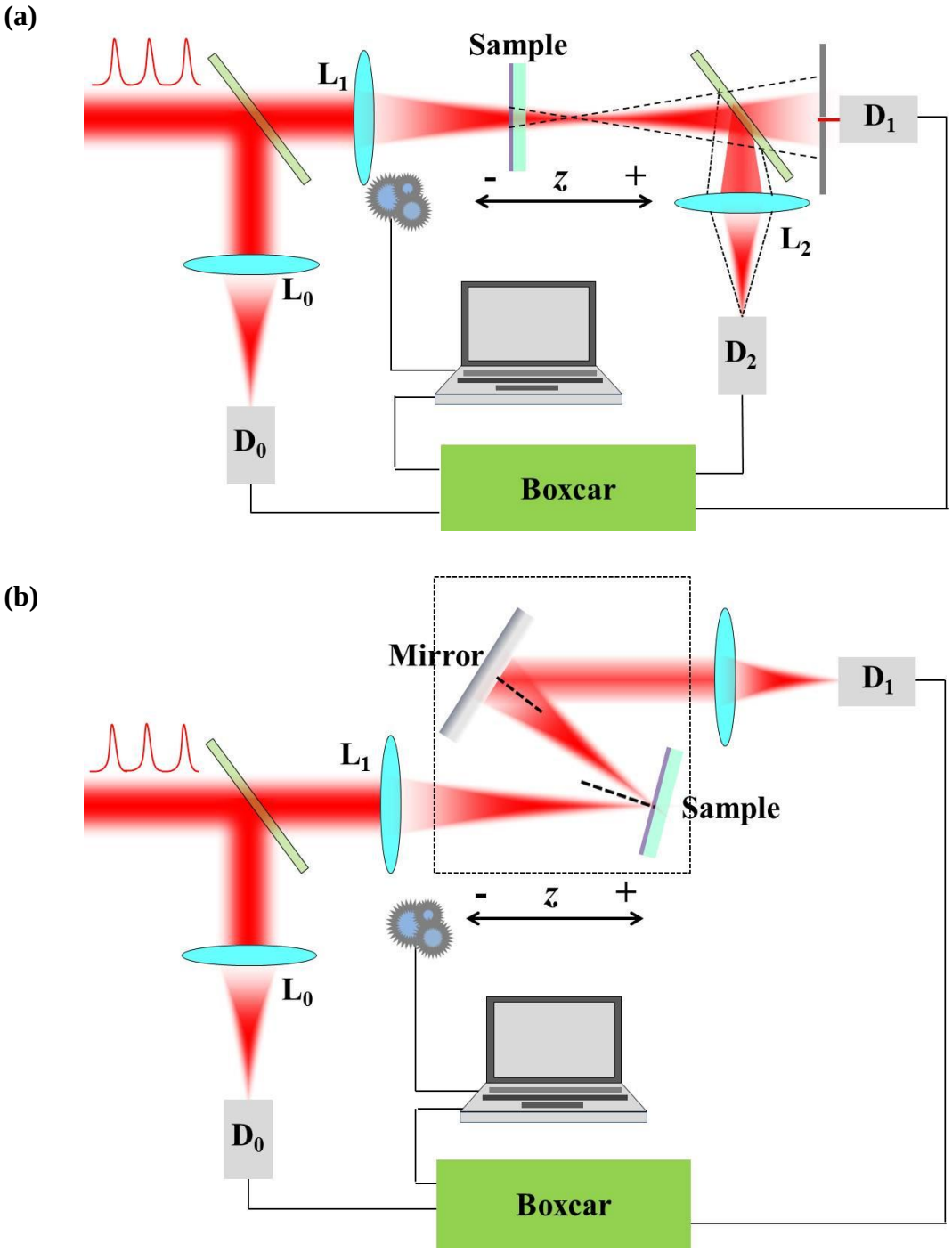

Figure 3.3 Schematic diagram of **(a)** transmission OA/CA Z-scan experiment set-up and **(b)** RZ-scan experiment set-up.

3.2 Z-scan measurements on epitaxial graphene at 780 nm

Figure 3.4(a) shows an example of the open-aperture TZ-scan traces (circles) of the substrate (SiC), mono-, bi- and six-layer graphene samples under 780 nm, 400-fs laser pulses. Each trace represents the experimental results from a single scan of a single sample. For the substrate and monolayer sample, the laser on-axis peak intensity at focal plane (I_{00}) is up to 80 GW/cm^2. While for bilayer and six-layer graphene samples, the maximum laser intensity is kept at I_{00} = 12 GW/cm^2 to avoid two-photon absorption [15]. These Z-scans are recorded when the incident angle is zero. Figure 3.4(a) shows that the normalized transmittance (T/T_0) increases as the sample moves towards the focal plane with higher irradiance, a typical signature for saturable absorption. The RZ-scan traces of SiC substrate, bi- and six-layer graphene under 780 nm femtosecond laser pulses with incident angle of 28 ^{o} are displayed in Figure 3.4(b), where the maximum laser intensity is kept at I_{00} = 65 GW/cm^2 for SiC and I_{00} = 12 GW/cm^2 for the graphene samples. The RZ-scan data of the monolayer sample is not presented here since the nonlinear signal is < 0.5 %, within the range of experimental errors. It should be noted that Figure 3.4 also shows that there is no nonlinear absorption in the substrate under our experimental conditions. Moreover, we have repetitively conducted Z-scan measurements under a sequence of laser intensities on several randomly selected positions of each sample. The results show good repeatability and reproducibility.

The above Z-scan data are the plots of the nonlinear signal as a function of the sample position (z). We obtained the sample transmittance (or reflectance) as a function

of the incident laser intensity by converting the *z*-position to the corresponding laser irradiance through $I_0 = I_{00}/[1+(z/z_0)^2]$, where I_0 and I_{00} are the on-axis peak intensities at position z and the focal plane, respectively, and z_0 is the Rayleigh length of the laser beam. Figure 3.5 shows the converted TZ-scan and RZ-scan data of the graphene samples. It is clearly shown that the saturable absorption signal (T/T_0) increases linearly as the number of graphene layers increases from one to six. The curves display the theoretical simulations which will be discussed in Chapter 4.

(a)

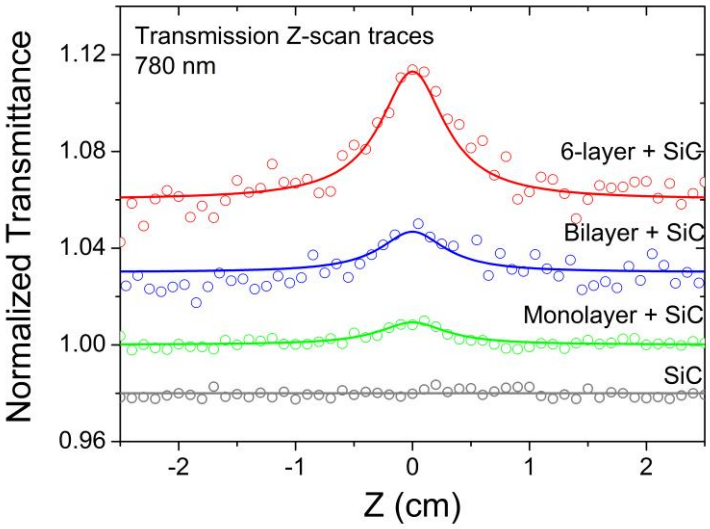

(b)

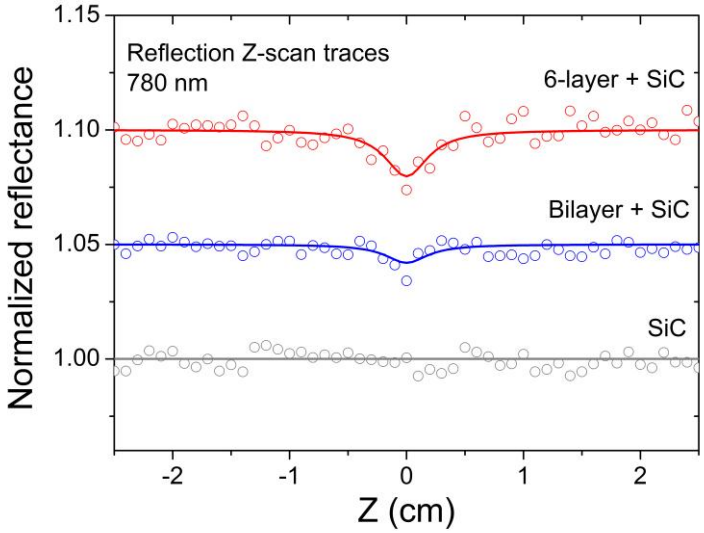

Figure 3.4 (a) Open-aperture TZ-scan traces of substrate (SiC), mono-, bi- and six-layer epitaxial graphene samples under 780 nm femtosecond laser pulses. **(b)** RZ-scan trances of SiC wafer, bi- and six-layer epitaxial graphene samples under 780 nm femtosecond laser pulses. The solid curves are calculated by Equations (3.1-3.7).

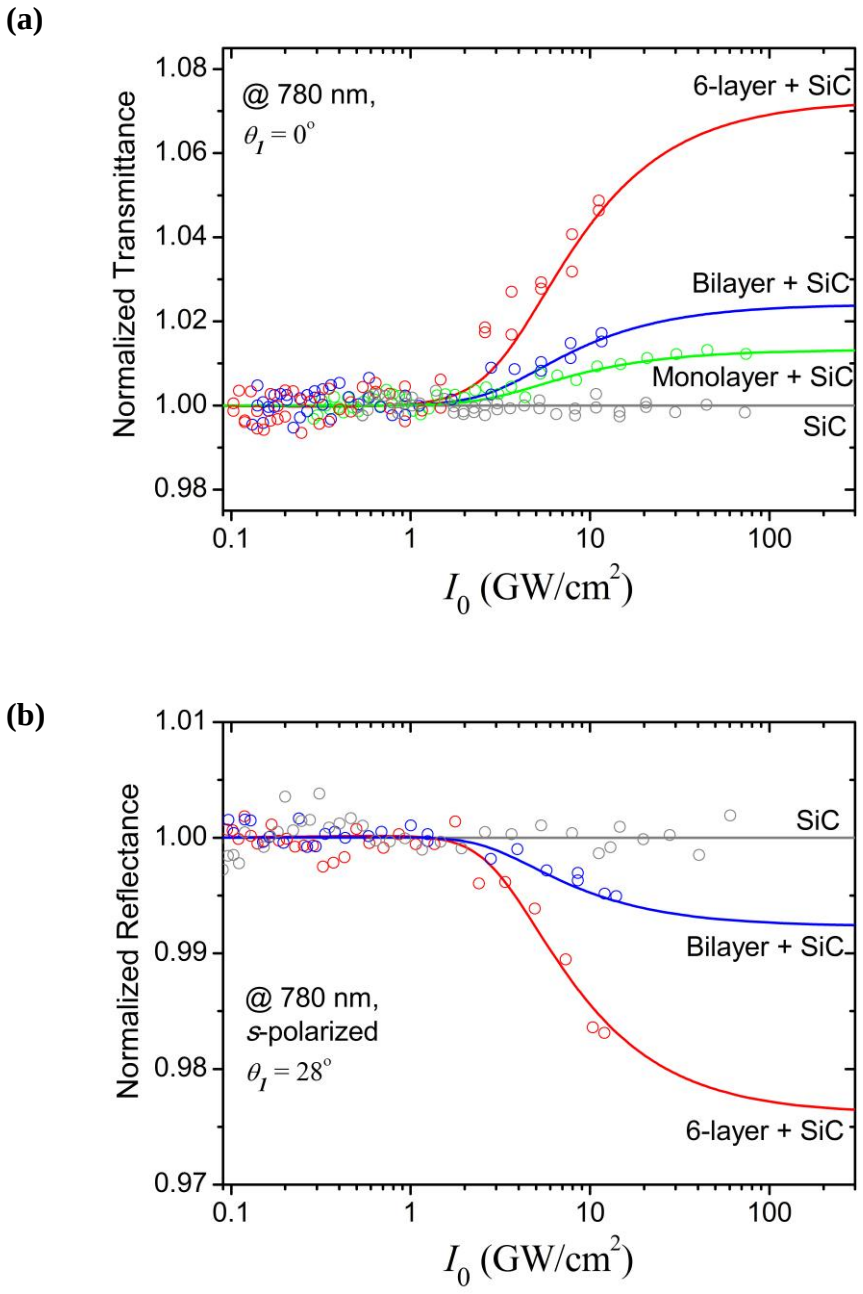

Figure 3.5 (a) Normalized total transmittance and **(b)** reflectance versus incident light irradiance for epitaxial graphene on SiC substrate at 780 nm. The circles are converted from the TZ-Scan and RZ-Scan data as discussed in the text and the curves are the theoretical simulations discussed in Chapter 4.

3.3 Determination of saturation intensity in epitaxial graphene

As discussed in Section 3.1.2, we solve Equations (3.1)-(3.7) numerically. The numerical solutions are used to fit the data in Figures 3.4. From the best fits, we extract the saturation intensity as it is the only free parameter in the numerical simulations. The extracted saturation intensities of our graphene samples with different number of layers are tabulated in Table 3.1. The experimental errors are the actual fluctuation observed in 5 series of repeated measurements, taking into account of the difference between samples points and the estimated error (~ 5%) in the laser pulse intensity measurements. The measured saturation intensity is shown to be almost independent on the number of graphene layers, as the variation of I_s is within the experimental errors ($\pm 40\%$) with the number of graphene layers increasing from one to six. This indicates that with the saturation intensity unaffected, the saturation depth of graphene will increase linearly as the number of graphene layers increases, which will benefit the application of graphene as saturable absorber in mode-locking.

Table 3.1 Saturation intensities of mono-, bi-, and six- layer graphene samples

Sample	Wavelength (nm)	Pulse width (fs)	Repetition rate	I_s (GW/cm^2)			
				TZ-scan fitting	Theory	RZ-scan fitting	Theory
MLG	780	400	1kHz	6 ± 2	7.2		
BLG	780	400	1kHz	6 ± 2	7.3	6 ± 2	7.3
6-LG	780	400	1kHz	5 ± 2	7.7	5 ± 2	7.7

Note that the I_s values under the theory will be discussed in Chapter 4.

It should be pointed out that the above Z-scan measurements were conducted with the laser intensity less than the damage threshold. The damage threshold of epitaxial graphene was reported to be ~ 300 GW/cm^2 [16], in agreement with our Z-scan experiments on the epitaxial graphene samples. In order to avoid laser-induced damage and other higher-order nonlinearities [15], the laser irradiance was kept below ~12 GW/cm^2 when performing Z-scan measurements on bilayer and six-layer graphene, while the highest irradiance was ~70 GW/cm^2 for monolayer graphene. Since the sample damage would induce asymmetry in Z-scan traces due to irreversible nature of damage [19], which can be excluded by the observation of symmetric and repeatable Z-scan traces, as shown in Figure 3.4.

3.4 Wavelength-dependent saturation intensity in epitaxial graphene

We also performed open-aperture TZ-scans on the bi-layer sample in a spectral range 900-1100 nm at room temperature. Figure 3.6(a) shows the TZ-scan data at the wavelength of 900 nm, 1000 nm, and 1100 nm with the on-axis peak intensity of 7 GW/cm^2. In these Z-scan traces, the saturable absorption signal (T/T_0) increases as the wavelength increases from 900 nm to 1100 nm, while the saturation intensity (I_s) is found to decrease from 5(±2) GW/cm^2 at 900 nm to 1.5(±0.5) GW/cm^2 at 1100 nm. Similar to Figure 3.5, the original Z-scan data is transformed into the plot of normalized

transmittance versus the laser irradiance as shown in Figure 3.6(b). The experimental findings on the spectral dependence of saturation intensity are summarized in Table 3.2.

Table 3.2 Spectral dependence of the saturation intensity of graphene

Sample	Wavelength (nm)	Pulse width (fs)	Repetition rate	***I*s (GW/cm^2)**	
				TZ-scan fitting	Theory
BLG	780	400	1kHz	6 ± 2	7.3
	900	200	1kHz	5 ± 2	6.5
	1000	200	1kHz	2 ± 0.5	5
	1100	200	1kHz	1.5 ± 0.5	3.6

Note that the I_s values under the theory will be discussed in Chapter 4.

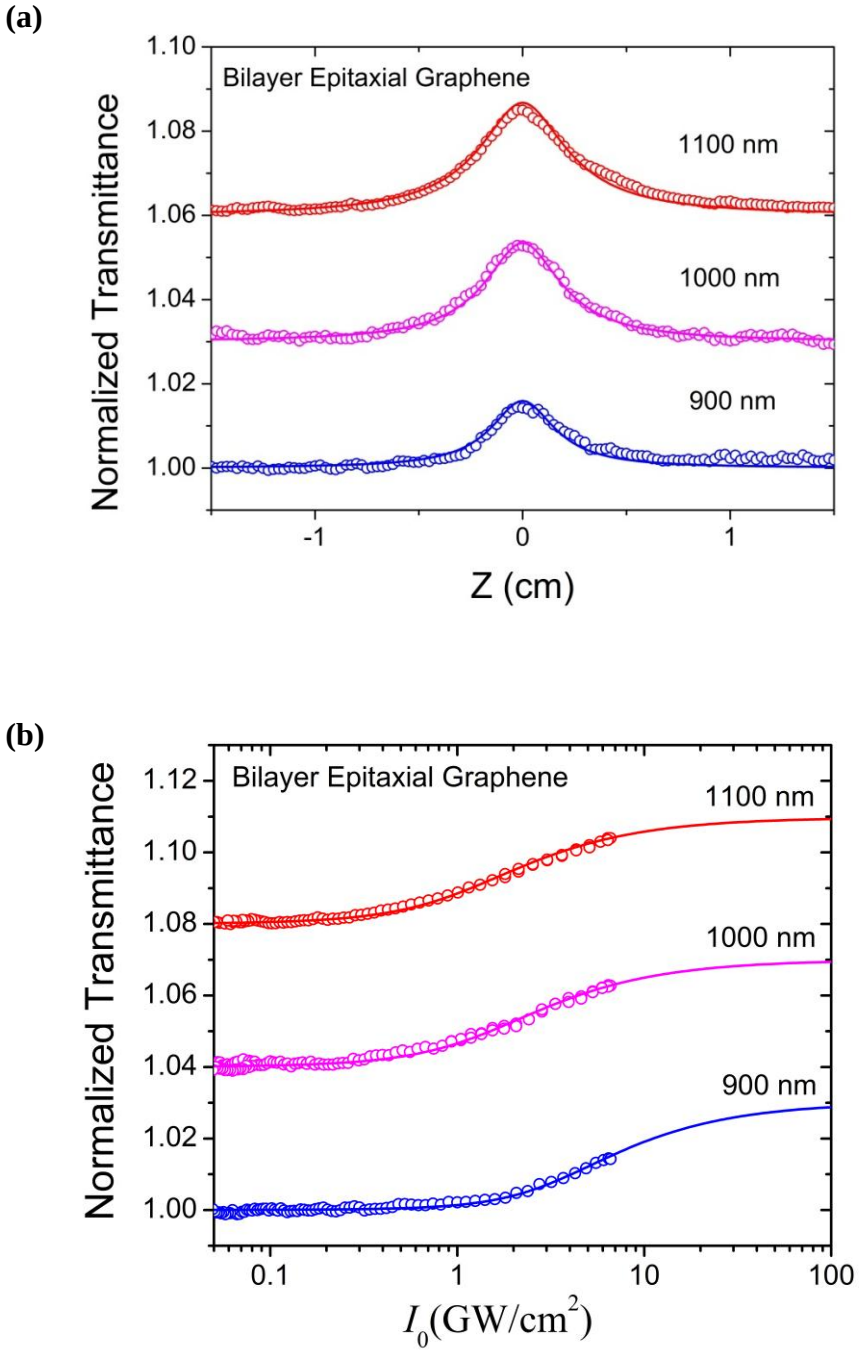

Figure 3.6 The spectral dependence of saturable absorption of graphene. **(a)** Open aperture TZ-scan trances at 900 nm, 1000 nm and 1100 nm with on-axis peak intensity of ~7 GW/cm^2 femtosecond laser pulses. The solid curves show the theoretical calculations by Equations (3.1 – 3.7). **(b)** Normalized transmittance versus irradiance, transformed from original Z-scan data as discussed in the text. The solid curves show the theoretical calculations in Chapter 4.

3.5 Summary

As summarized in Tables 3.1 and 3.2, we experimentally determined the saturation intensity in epitaxial graphene with different number of layers by performing TZ-scan and RZ-scan experiments at 780 nm. The saturation intensities for the mono-, bi-, and six-layer epitaxial graphene are found to be almost independent on the number of graphene layers. TZ-scan measurements on the bilayer graphene sample in a spectral range (780 nm-1100 nm) reveal that the saturation intensity decreases as the operating wavelength increases.

References:

1. Sheik-Bahae, M.; Said, A. A.; Wei, T. H.; Hagan, D. J.; Van Stryland, E. W., Sensitive measurement of optical nonlinearities using a single beam. *IEEE Journal of Quantum Electronics,* **1990**, 26, 760.

2. Huang, H.; Chen, W.; Chen, S.; Wee, A. T. S., Bottom-up growth of epitaxial graphene on 6H-SiC(0001). *Acs Nano* **2008**, 2, 2513.

3. Yang, H.; Baffou, G.; Mayne, A. J.; Comtet, G.; Dujardin, G.; Kuk, Y., Topology and electron scattering properties of the electronic interfaces in epitaxial graphene probed by resonant tunneling spectroscopy. *Phys. Rev. B* **2008**, 78, 041408.

4. Graf, D.; Molitor, F.; Ensslin, K.; Stampfer, C.; Jungen, A.; Hierold, C.; Wirtz, L., Spatially resolved raman spectroscopy of single- and few-layer graphene. *Nano Lett.* **2007**, 7, 238.

5. Lee, D. S.; Riedl, C.; Krauss, B.; von Klitzing, K.; Starke, U.; Smet, J. H., Raman spectra of epitaxial graphene on sic and of epitaxial graphene transferred to SiO_2. *Nano Lett.* **2008**, 8, 4320.

6. Ni, Z. H.; Chen, W.; Fan, X. F.; Kuo, J. L.; Yu, T.; Wee, A. T. S.; Shen, Z. X., Raman spectroscopy of epitaxial graphene on a sic substrate. *Phys. Rev. B* **2008**, 77, 115416.

7. Ferrari, A. C.; Robertson, J., Interpretation of raman spectra of disordered and amorphous carbon. *Phys. Rev. B* **2000**, 61, 14095.

8. Ferrari, A. C.; Meyer, J. C.; Scardaci, V.; Casiraghi, C.; Lazzeri, M.; Mauri, F.; Piscanec, S.; Jiang, D.; Novoselov, K. S.; Roth, S.; Geim, A. K., Raman spectrum of graphene and graphene layers. *Phys. Rev. Lett.* **2006**, 97, 187401.

9. Varchon, F.; Mallet, P.; Magaud, L.; Veuillen, J. Y., Rotational disorder in few-layer graphene films on 6H-SiC(000-1): A scanning tunneling microscopy study. *Phys. Rev. B* **2008**, 77, 165415.

10. Berger, C.; Song, Z.; Li, T.; Li, X.; Ogbazghi, A. Y.; Feng, R.; Dai, Z.; Marchenkov, A. N.; Conrad, E. H.; First, P. N.; de Heer, W. A., Ultrathin epitaxial graphite: 2D electron gas properties and a route toward graphene-based nanoelectronics. *J. Phys. Chem. B* **2004**, 108, 19912.

11. Chen, W.; Xu, H.; Liu, L.; Gao, X. Y.; Qi, D. C.; Peng, G. W.; Tan, S. C.; Feng, Y. P.; Loh, K. P.; Wee, A. T. S., Atomic structure of the 6H-SiC(0001) nanomesh. *Surf. Sci.* **2005**, 596, 176.

12. Poon, S. W.; Chen, W.; Tok, E. S.; Wee, A. T. S., Probing epitaxial growth of graphene on silicon carbide by metal decoration. *Appl. Phys. Lett.* **2008**, 92, 104102.

13. R. L. Sutherland; D. G. Mclean; Kirkpatrick, S., *Handbook of nonlinear optics*. 2nd ed. ed.; Marcel Dekker, Inc.: New York, 2003.

14. http://en.wikipedia.org/wiki/Gaussian_beam

15. Yang, H.; Feng, X.; Wang, Q.; Huang, H.; Chen, W.; Wee, A. T. S.; Ji, W., Giant two-photon absorption in bilayer graphene. *Nano Lett.* **2011**, 11, 2622.

16. Xing, G.; Guo, H.; Zhang, X.; Sum, T. C.; Huan, C. H. A., The physics of ultrafast saturable absorption in graphene. *Opt. Express* **2010**, 18, 4564.

Chapter 4

Theoretical investigation on saturable absorption in intrinsic graphene

The saturable absorption in epitaxial graphene with different number of layers and the spectral dependence of the saturation have been experimentally examined in Chapter 3. In this Chapter, we theoretically investigate the effects of graphene layer numbers on the saturation intensities and the correlation between the saturable absorption and substrates. Besides, the dispersion (or spectral dependence) of saturation intensity of graphene is also quantitatively evaluated and compared with the experimental measurements. It need to be pointed out that in the study of this thesis, the doping effects [1-3] which might attribute to the charge transfer from the defects [4-6]and substrates [7-9] are not taken into consideration and require further investigation. Intrinsic (or un-doped) graphene is assumed in this thesis if not specified.

This Chapter is organized as follows: Section 4.1 summarizes the saturation intensities of graphene reported by other groups and present studies. Section 4.2 presents the theoretical estimation of saturable absorption in intrinsic graphene at 780 nm, where the substrate effects and number of graphene layer impacts on the saturation intensity as well as the modulation depth of graphene are discussed. Our Z-scan measurements are compared with the theory in section 4.3. Section 4.4 demonstrates a

systematic calculation of the spectral dispersion of saturation intensity in graphene, followed by a summary in Section 4.5.

4.1 Literature review on the saturation intensity of graphene

As an important parameter in determining the performance of a saturable absorber, the saturation intensity (I_s) of graphene has recently been studied intensively with direct nonlinear transmittance measurements, Z-scan, and pump-probe techniques [10-17]. Various graphene samples, synthesized by exfoliation, epitaxial, CVD, and LPE methods, have been employed in the previous reports. Besides, theoretical research of saturable absorption in graphene has also attracted much attention [18-20]. However, there is a large discrepancy in the reported I_s of graphene, which might be due to the different synthesis methods and experimental conditions. The saturation intensity of graphene reported by other groups and present study are summarized in Table 4.1.

By sandwiching a CVD graphene sheet between two segments of fibers, I_s was firstly studied by nonlinear transmission measurements with ultrafast laser pulses at 1550 nm (1 ps, 100 MHz) [11]. The I_s of 2-4 layer CVD graphene at 1550 nm was reported to be 0.71 MW/cm^2. Thereafter, the I_s of a LPE graphene-polymer composite was extracted by the nonlinear transmittance measurements with ultrafast laser at 1558 nm (0.58 ps, 38.83 MHz).[12] The saturation intensity I_s of the LPE graphene was measured to be >266 MW/cm^2, which is two orders of magnitude higher than that of CVD-grown graphene in

the previous report. Recently, by depositing exfoliated graphene flakes on the fiber-end, the I_s of exfoliated graphene was studied by nonlinear transmittance measurements with ultrafast laser at 1550 nm (500 fs, 50 MHz).[15] The saturation intensities I_s of 8, 13, 30 layer graphene samples were measured to be 90, 350, and 380 MW/cm^2, respectively. This result is within the same order of magnitude with the report of LPE graphene.

Apart from the quality of graphene samples varying from one synthesis method to the other, the operating wavelength would also determine I_s of graphene.[20] The I_s of epitaxial graphene was measured to be ~ 4 GW/cm^2 at 800 nm using Z-scan technique [10], which is one order higher than the report of exfoliated graphene at 1550 nm. This could be attributed to different operating wavelength, as predicted theoretically by Vasko [20].

Many experimental measurements on saturable absorption of graphene have been conducted in the near infrared spectral range [10-17]; however, a systematical study on the dispersion (or spectral dependence) of saturable absorption in graphene has not been reported yet. The study is desirable for fundamental researches as well as the future applications. It will contribute to a deep understanding of the saturation mechanism in graphene and facilitate the applications of graphene as a saturable absorber in a wide spectrum range.

Table 4.1 Comparison of reports on saturation intensity of graphene

Sample	Geometry	Laser	I_s (GW/cm^2)	Method	References
Epitaxial Graphene	Deposited on SiC substrate	400 fs, 1kHz 780 nm	6 ±2	Z-scan	Present study
		900 nm	5 ±2		
		200 fs, 1kHz 1000 nm	2 ±0.5		
		1100 nm	1.5 ±0.5		
CVD Graphene	Sandwiched between two segments of fibers	1 ps, 100 MHz,1550 nm	0.0007	Transmittance	2009 [11]
Epitaxial Graphene	Deposited on SiC substrate	200 fs, 1 kHz, 800 nm	4 ±1	Z-scan	2010 [10]
Exfoliate Graphene in PVA polymer	Graphene-polymer composite was sandwiched between two segments of fibers	580 fs, 39 MHz,1558 nm	> 0.266	Transmittance	2010 [12]
Exfoliate Graphene	Deposited on the core of an optical fiber-end	500 fs,50 MHZ, 1550nm	0.09-0.38	Transmittance	2011 [15]
Intrinsic Graphene	Ideal graphene on SiO_2 substrate	0.4 ps, 750 nm	0.6	Theoretical	2010 [20]
		0.6 ps, 1550 nm	0.06		
		1 ps, 10.36 μm	0.0002		
Intrinsic Graphene	Ideal freestanding graphene	800 nm	4	Theoretical	2011 [19]

4.2 Theoretical estimations of saturable absorption in intrinsic graphene at 780 nm

In this Section, following the mathematical model which was discussed in Chapter 2, quantitative treatments are implemented to explain our experimental observations. The parameters (Γ, τ ,τ_2) used in our calculation throughout this thesis are taken from previous reports: Γ = 12 meV [20, 21], τ = 10 fs [10, 21] and τ_2 = 2 ps [22-26]. We have also used the ranges of Γ = 6 ~ 30 meV [20] and τ = 10 ~ 50 fs [21] to calculate the optical conductivity of graphene, finding that the variation is so insignificant (less than 5%) that the conductivity is insensitive to the values within the ranges. The carrier relaxation time τ_2 has been reported to be proportional to the crystal coherence length [22], and therefore may vary dramatically from sample to sample. It might also fluctuate much with different operation wavelengths, fabrication methods and sample substrates.[22-34] However, by assuming τ_2 = 0.5 ~ 10 ps in our calculation, the I_s vibration caused is found to be within 20% and is considered to be insignificant. Thus, τ_2 = 2 ps is applied to all the wavelengths from optical to NIR in this theoretical simulation.

Figure 4.1 reproduces the scattering geometry of the laser light. In the following, *T*, *R* and *A* are exactly specified as the transmittance and reflectance at the graphene separated interface, which can be computed from Equations (2.8- 2.10).

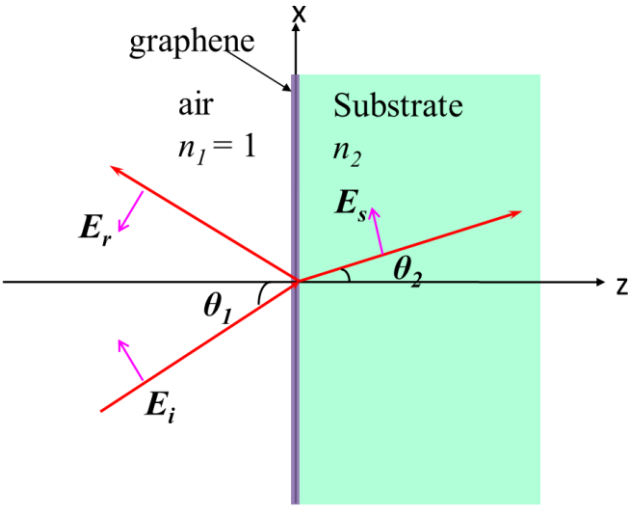

Figure 4.1 Geometry of *p*-polarized light scattering on graphene separated interfaces. n_1 / n_2 represent the refractive indices of the two media.

In order to investigate the substrate influence on the saturable absorption of graphene, we start from the simplest geometry-freestanding ($n_1 = n_2 = 1$) graphene. The complex optical conductivity of freestanding monolayer graphene at 780 nm as a function of the incident light irradiance (I_0) is shown in Figure 4.2(a). It indicates that the intraband transition is insignificant in the real part, while it plays an important role in the imaginary part. Correspondingly, the intensity dependence of *T*, *R* and *A* for freestanding monolayer graphene under normal incidence are shown in Figure 4.2(b). The linear (or low-intensity) absorbance is ~2.3% (see the blue dashed curve), in agreement with the theoretical value and many experimental data [35-37]. At high excitations (>100 GW/cm^2), the absorbance is not completely saturated (or zero) as limited by intraband absorption. Consistent with the report [35], the reflectance from freestanding graphene can be ignored justifiably due to its small magnitude.

In the characterization of saturable absorbers, I_s is an important parameter usually defined as the intensity at which the absorption coefficient drops to half of its linear value. The modulation depth ΔT shown in Figure 4.2(b) is another important performance indicator for a saturable absorber in mode-locking technology. Here, it can be seen that I_s can also been extracted as the intensity at which the transmittance increase by half of ΔT with respect to the low-intensity value. For freestanding monolayer graphene excited by normal incident ultrashort laser pulses (τ_L = 400 fs) at 780 nm, I_s is calculated to be ~2.2 GW/cm^2 by the theoretical model discussed in Chapter 2.

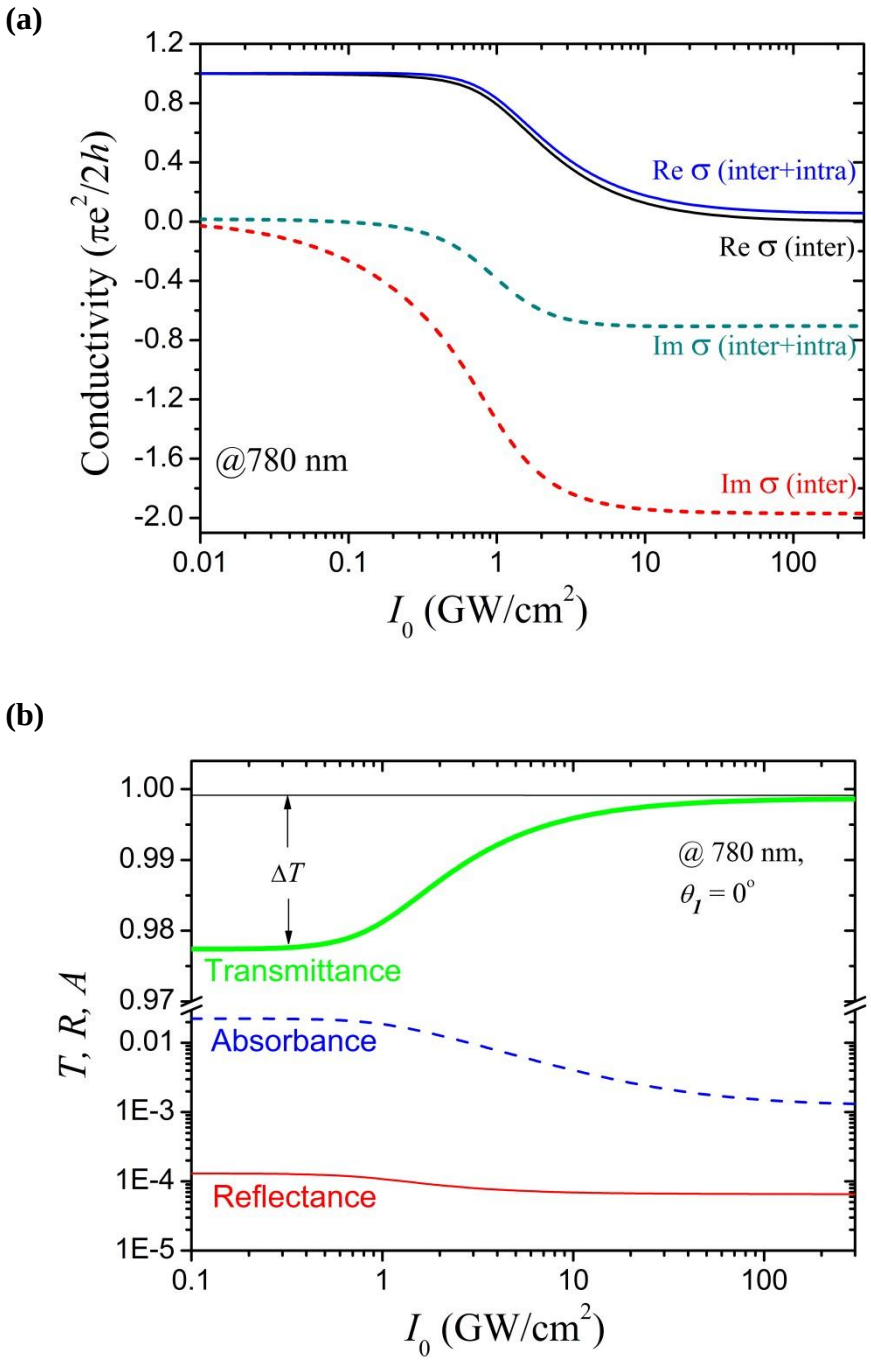

Figure 4.2 (a) Complex inter- and intra-band conductivity (σ_{inter} and σ_{intra}) of freestanding monolayer graphene as a function of the incident light irradiance at 780-nm wavelength. **(b)** The intensity dependence of *T*, *R* and *A* for freestanding monolayer graphene ($n_1 = n_2 = 1$) under normal incidence. The arrows display the modulation depth.

As for the graphene sheets deposited on a substrate ($n_2 \neq 1$), the transmittance, reflectance, and absorbance at the graphene separated interface are modified as discussed below. Figure 4.3(a) displays the *T* and *R* of monolayer epitaxial graphene as a function of the incident light irradiance (I_0), under normal incidence at 780 nm. Because of the presence of substrate (n_2 = 2.61 for SiC), the linear transmittance is reduced from ~97% to ~79%; the linear reflectance is increased from ~ 0.01% to ~20%; and accordingly the linear absorbance of monolayer graphene is reduced from ~2.3% to ~1% (not shown in the Figure), which is in agreement with our experiments. It can also be seen that the transmittance of graphene on SiC substrate saturates at a higher intensity (~ 7.2 GW/cm^2) than that of freestanding graphene (~ 2.2 GW/cm^2). The comparison of *T* between monolayer freestanding graphene and monolayer graphene sheets on two commonly used substrate, quartz (n_2 =1.54) and SiC (n_2 =2.61), is highlighted in Figure 4.3(b). The saturation intensity of graphene is shown to increase as the refractive index of the substrate (n_2) increases. Additionally, the modulation depth of the graphene sample decreases as the refractive index of the substrate (n_2) increases, consistent with the theory reported by Vasko in 2010 [20].

Figure 4.3(b) demonstrates that freestanding graphene would be favorable in the mode-locking technology than graphene on substrates in terms of I_s and the modulation depth.

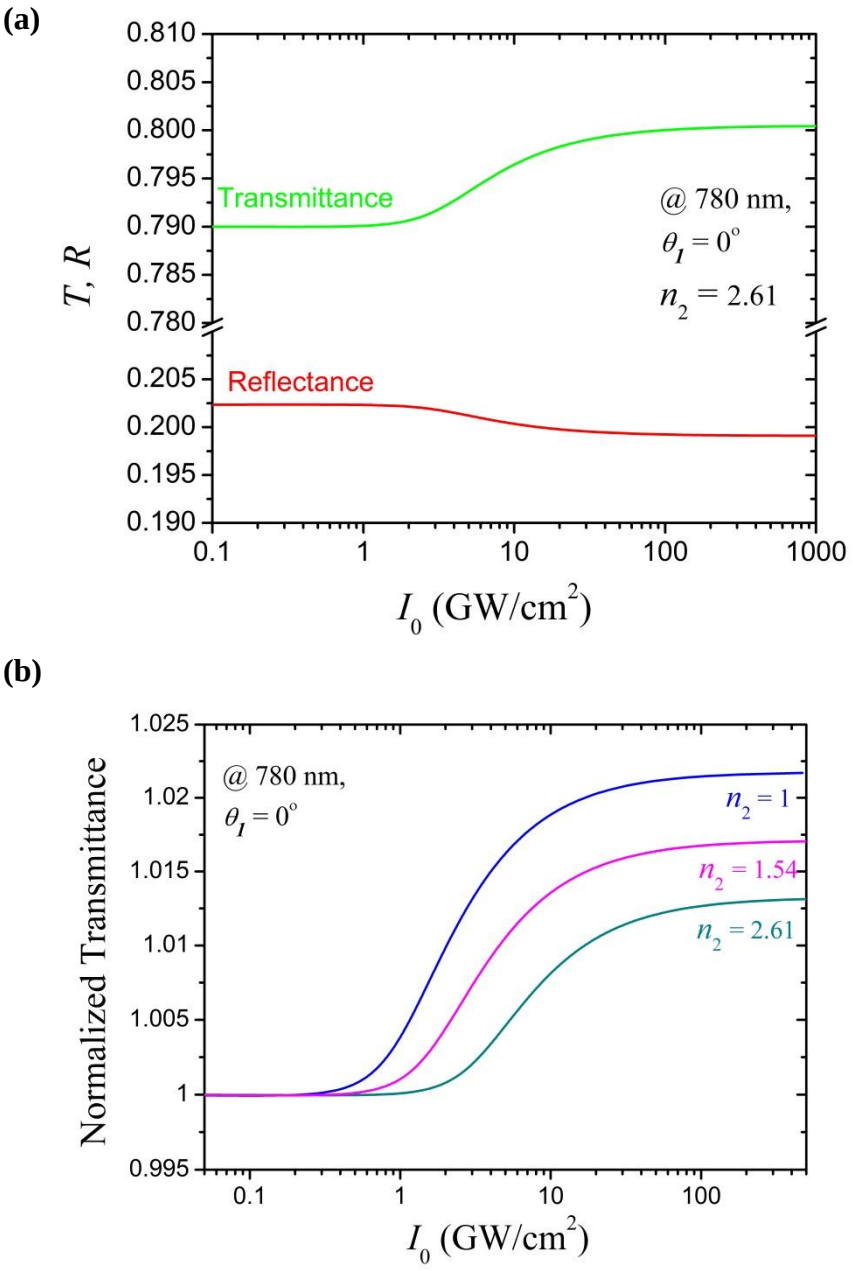

Figure 4.3 (a) The intensity dependence of T and R for monolayer graphene on SiC substrate (n_2 = 2.61) under normal incidence irradiance at 780-nm wavelength. **(b)** Comparison of T between freestanding graphene (m = 1, n_2 = 1) and graphene on substrate (m = 1, n_2 = 1.54 and 2.61).

To illustrate the number of graphene layer effects on saturable absorption, Figure 4.4 compares the transmittances through freestanding graphene with different number of layers. It can be seen that the saturation intensity increases slightly as the number of graphene layer increases. Restricted within ten-layers, the growth is less than 20% (I_s ~ 2.6 GW/cm^2 for ten-layer graphene compared to I_s ~ 2.2 GW/cm^2 for monolayer), which is within the range of our experimental errors (± 40%) and may be undetectable. Here, the number of graphene layers is limited to ten as in experiments more layers may result in more non-saturable losses due to the imperfection of samples, *e.g.* defects, impurities. Although graphene thickness does not alter the saturation intensity in a significant way, it modifies the modulation depth considerably. From Figure 4.4, the modulation depth is found to increase linearly as the number of graphene layers increases from one to ten.

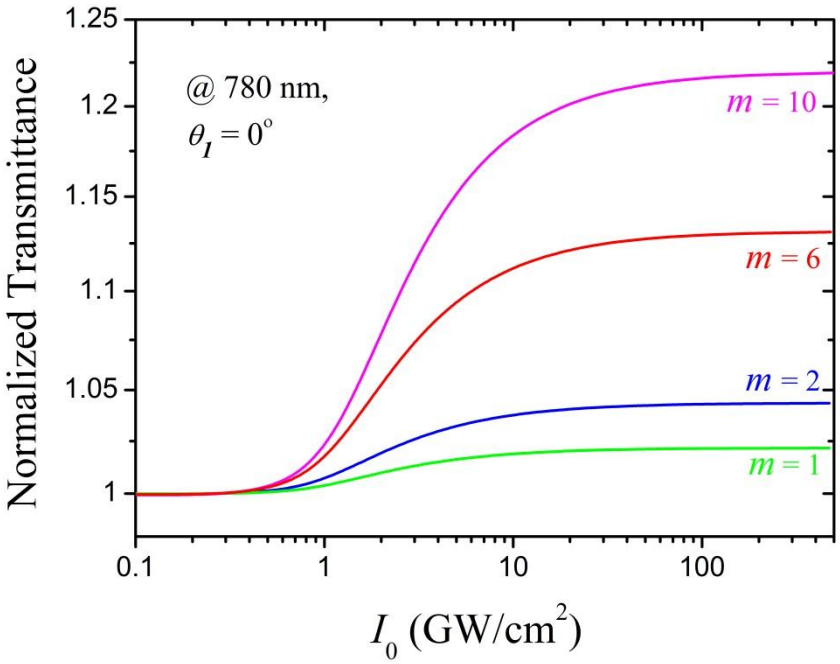

Figure 4.4 Comparison between freestanding mono-, bi-, six- and ten-layer graphene (n_2 = 1).

As an important performance indicator for a saturable absorber, the modulation depth of graphene is shown previously to be proportional to the number of graphene layers, while it is inversely proportional to the refractive index of the substrate. Associated with the universal linear absorption coefficient, the modulation depth would be independent on the operation wavelength at visible-NIR region. Figure 4.5 displays the calculated modulation depth as a function of the number of graphene layers suspended and deposited on quartz and SiC substrates. As shown in the Figure, the modulation depth of 10-layer graphene is about one order of magnitude greater than its monolayer counterpart. Besides, the modulation depth of suspension graphene is nearly two times as large as that on SiC substrate.

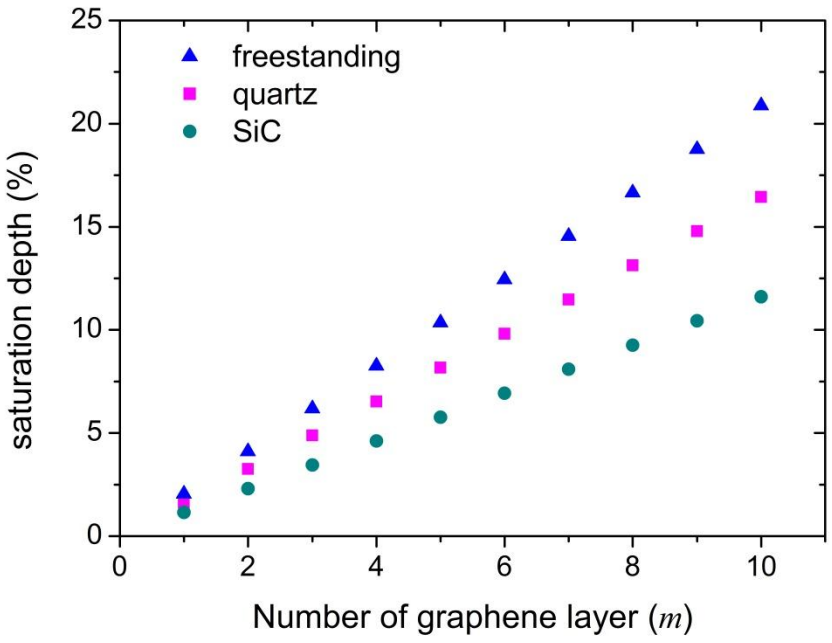

Figure 4.5 Modulation depths as a function of the number of graphene layers suspended and on two different substrates.

4.3 Theoretical fitting of the Z-scan measurements

In order to simulate our experimental measurements on graphene samples consisting of epitaxial graphene and SiC substrate, the computation as followed is taken. The scattering geometry of the *p*-polarized light on the graphene sample is schematically depicted in Figure 4.6. In the theoretical simulations, the total transmittance through the entire graphene sample is approximately to be $T_{total}\ (I_0)= |E_t/E_i|^2 \approx T(I_0)\ T_{sub\text{-}air}$, where $T(I_0)$ is the transmittance through the graphene sheet to the substrate, which has been demonstrated throughout in the previous part, $T_{sub\text{-}air} = 4n_1n_2(n_1+n_2)^{-2}$ is the transmittance of the interface between the substrate and air. Both the multiple reflections and nonlinear refraction in the substrate are assumed to be negligible. The total reflectance is approximately by $R_{total}\ (I_0) \approx R(I_0) + T(I_0)\ R_{sub\text{-}air}\ T(y)$, where $R(I_0)$ and $T(I_0)$ is the reflectance and transmittance at the graphene separated interface, $R_{sub\text{-}air} = (n_1\text{-}n_2)^2/(n_1+n_2)^2$ is the reflectance of the interface between the substrate and air, and $y = I_0\ T(I_0)\ R_{sub\text{-}air}$. The interested values of y are relatively much smaller than I_0 and hence, we assume that $T(y) \approx T(0)$, the linear transmittance of graphene sheet in our calculation.

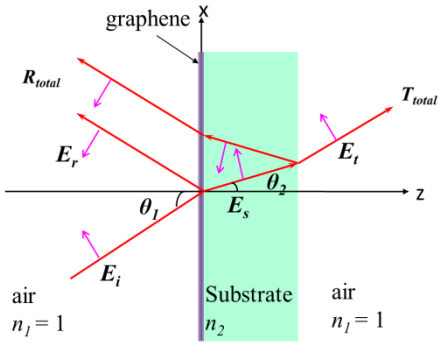

Figure 4.6 A schematic diagram for *p*-polarized light scattering on the graphene sample. n_1 / n_2 represent the refractive indices of the two media.

Consequently, following the above-mentioned method, the total transmittance and reflectance of the graphene sample at 780 nm are calculated, as depicted by the solid curves in Figure 4.7. The theoretical curves in Figure 4.7 are in good accordance with the experimental data in which the maximum laser intensity was up to 80 GW/cm^2. As demonstrated in Chapter 3, the saturation intensities extracted from the Z-scan experiments are 6(±2) GW/cm^2, 6(±2) GW/cm^2 and 5(±2) GW/cm^2 for mono-, bi- and six-layer graphene samples, respectively. Besides, the theoretical I_s is computed to be 7.2 GW/cm^2, 7.3 GW/cm^2 and 7.7 GW/cm^2 for mono-, bi- and six-layer graphene samples, respectively. The vibration of the I_s in theory is within the experimental errors (± 40%) as the number of graphene layers increases from 1 to 6, and thus would be undetectable. The agreements between our computation and experimental data validate our photodynamic approximation theory.

The theoretical simulations of our experimental measurements at 900, 1000 and 1100 nm are conducted similarly, as shown by the solid curves in Figure 4.8. In retrospect to Chapter 3, the saturation intensities extracted from the Z-scan experiments are 5(±2) GW/cm^2 at 900 nm, 2(±0.5) GW/cm^2 at 1000 nm and 1.5(±0.5) GW/cm^2 at 1100 nm. The numerical solutions of the I_s are found to be 6.5 GW/cm^2, 5 GW/cm^{2}and 3.6 GW/cm^2 at 900 nm, 1000 nm and 1100 nm, respectively. It should be pointed out that in order to better fit the experimental data, m = 2.5 were used in the simulation. Besides, to fit the theoretical curves with the experimental circles in Figure 4.8, the numerical computed horizontal axis are modified by a factor of ×0.5 and × 0.53 for 1000 nm and

1100 nm, respectively.

Within one order of magnitude, agreements can be found between our model and the experiments. The discrepancy might be attributed to unintentional doping in the sample or spatial profile of laser pulse used in the experiments. In our theoretical model, the spatial profile of laser pulses is not taken into consideration, which requires to be further amended. Besides, the graphene samples are assumed to have no defects which may introduce scattering loss. Moreover, this theoretical treatment is based on many approximations where the assumptions might fail and thus causes deviation from experiment. Noticeably, there is a relatively large discrepancy between experiments and theory for 1000 nm and 1100 nm wavelengths. Besides the factors listed above which are beyond control, it might be most likely due to failure of the second assumption summarized at Section 2.4. In our model, the excited electron temperature evolution is assumed to be independent of the excitation laser wavelength, which is lacking of evidence to support. The excited electron temperature decay parameters employed in our calculation are deduced from an experimental observation made at 830 nm. The parameters might be more acceptable for spectral range from 780 nm to 900 nm. But, beyond the range, the parameters used are questionable and needed to be measured in future investigations.

(a)

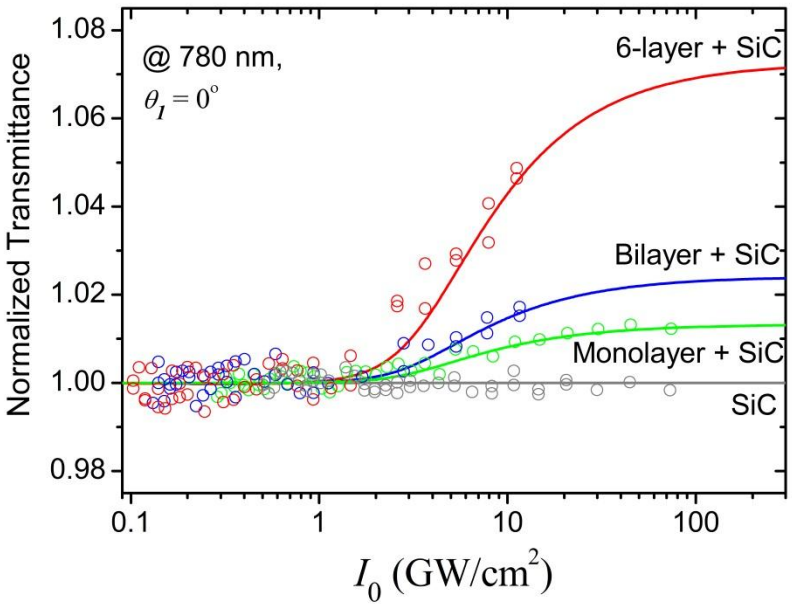

(b)

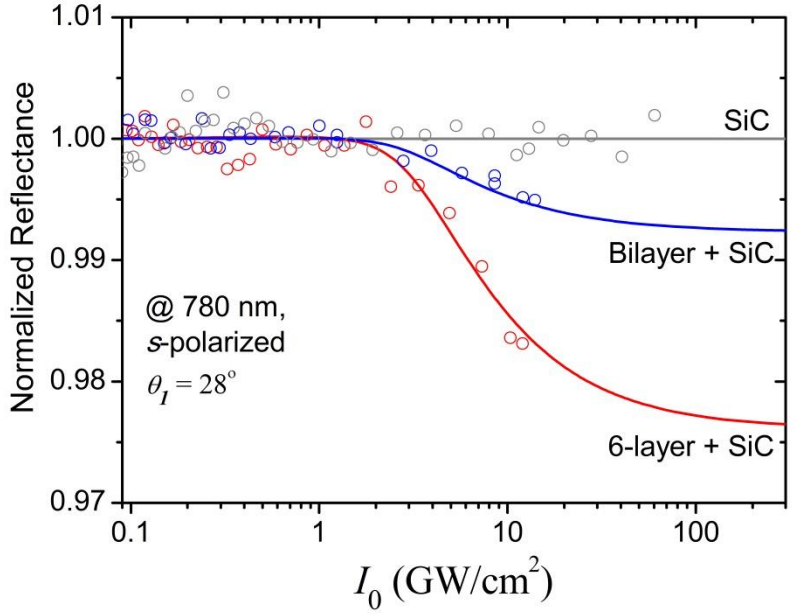

Figure 4.7 (a) Normalized total transmittance and **(b)** reflectance versus incident light irradiance for epitaxial graphene on SiC substrate at 780 nm. The circles are converted from the TZ-Scan and RZ-Scan data as demonstrated in Chapter 3 and the curves are the theoretical simulations discussed in the text.

(a)

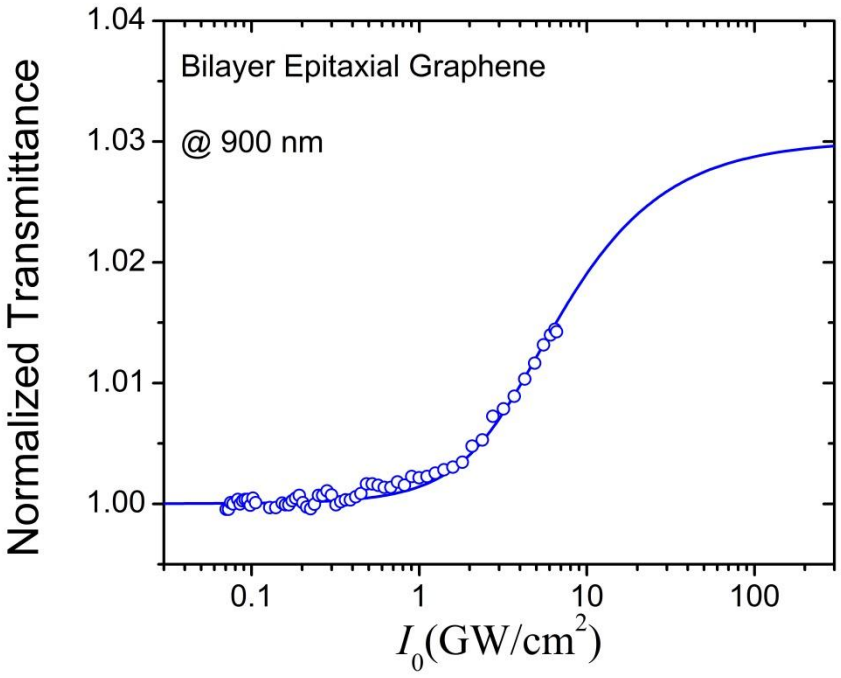
Bilayer Epitaxial Graphene
@ 900 nm
Normalized Transmittance
1.04
1.03
1.02
1.01
1.00
0.1
1
10
100
$I_0(\mathrm{GW/cm^2})$

(b)

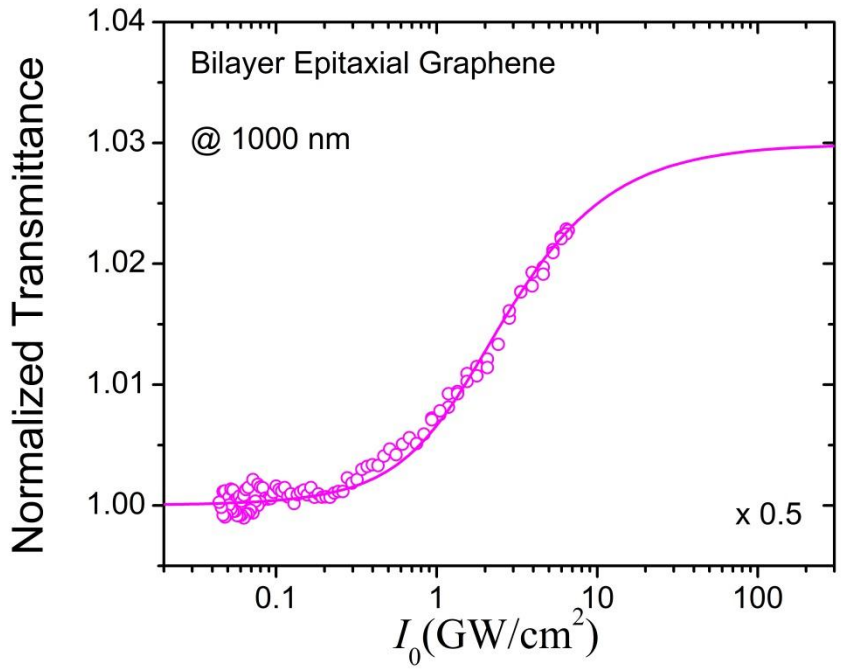
Bilayer Epitaxial Graphene
@ 1000 nm
x 0.5
Normalized Transmittance
1.04
1.03
1.02
1.01
1.00
0.1
1
10
100
$I_0(\mathrm{GW/cm^2})$

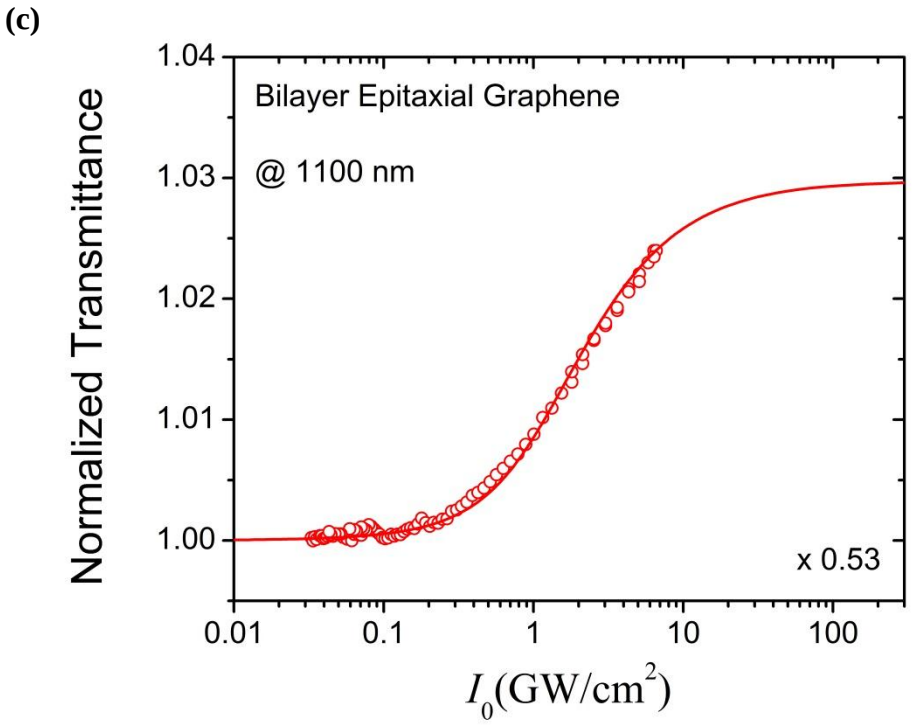

Figure 4.8 Normalized total transmittance versus incident light irradiance for epitaxial bilayer graphene on SiC substrate at **(a)** 900 nm, **(b)** 1000 nm and **(c)** 1100 nm. The circles are converted from the TZ-Scan and RZ-Scan data as demonstrated in Chapter 3 and the curves are the theoretical simulations discussed in the text.

4.4 Spectral dispersion of saturation intensity in intrinsic graphene

In Section 3.4 of this thesis, the Z-scan measurements of saturable absorption in epitaxial graphene at different wavelengths have been presented. Here, we will demonstrate a systematic calculation of the spectral dispersion of saturation intensity in graphene.

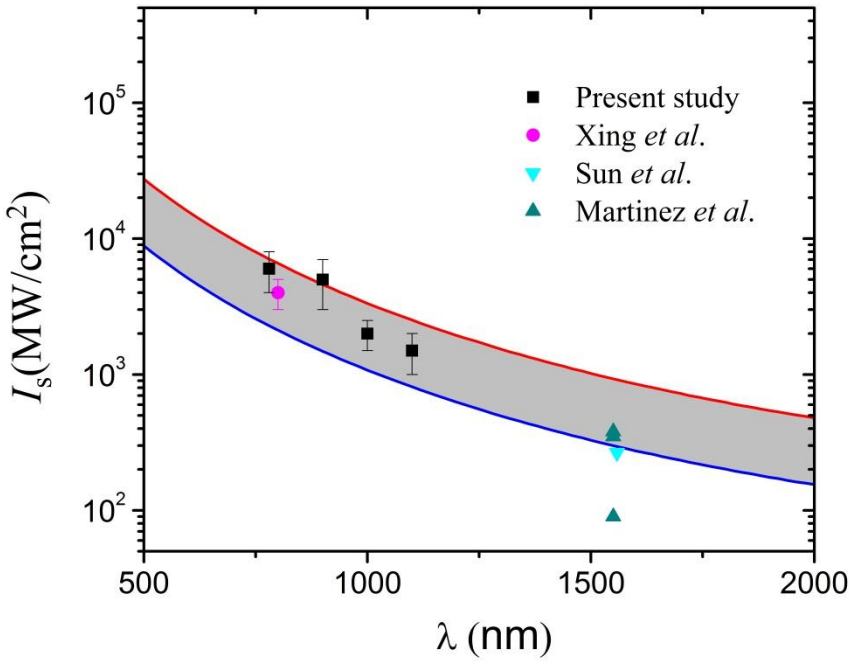

Figure 4.9 Spectral-dependent saturation intensity in graphene. The data points are the experimental values of our samples and experimental data reported by other groups, and the curves are the theoretical results. The red curve is calculated with n_2 = refractive index of SiC, and the blue curve is calculated by using $n_2 = 1$.

Figure 4.9 shows the theoretical estimated and experimental measured saturation intensities at various wavelengths ranging from the visible to near-infrared spectral region. Two boundary lines are plotted for coverage of freestanding graphene and graphene on SiC substrate. The saturation intensity decreases as the laser operating wavelength is red-shifted. Approximately, the saturation intensity at 1550 nm is one order of magnitude less than that at 780 nm. It can be seen that graphene is a superior saturable absorber in producing ultrashort laser pulses in a wide spectral range, especially in the infrared range.

The data points include the experimental values of our samples described above and the data reported by other groups [10, 12, 15]. Within one order of magnitude, agreements can be found between our model and the experiments. However, we notice that the above agreement between the theory and the experiments is achieved on graphene samples that were made by epitaxial growth or exfoliation. Conversely, our estimation deviates far from the results of Bao *et al.* [11] who observed I_s to be ~ 0.7 MW/cm^2 in samples prepared by CVD method. In comparison with other experimental reports, the saturation intensity of CVD graphene is almost three orders lower than the value of graphene samples synthesized by other methods [11, 12, 15]. Such lower saturation intensity might be induced by the unique characteristic of CVD graphene. It was reported that the electronic mobility of CVD graphene is much lower than that of exfoliated and epitaxial graphene, due to the local electronic corrugations and doped regions in it [38-40]. Additionally, CVD graphene is well known with a high number of structural defects.[6] Charge carrier doping of graphene by these defects may change its electronic properties [6] and results to a modification in the optical saturation. In view of the defects and doping in CVD graphene, the theoretical assumptions made in our calculation would be inaccurate and cause divergence between theory and experiment. Nevertheless, to the best of our knowledge, no theory is capable to predict such low saturation intensity to date; further systematic investigations into CVD-growth graphene are required.

Moreover, it needs to be pointed out that in the fiber lasers such as Ref [11, 12, 15, 41], the graphene structures were embedded into the laser cavities, therefore the

electrodynamical conditions (for propagated, reflected, and absorbed radiations) were different from the simple geometry considered here. This geometry irregularity may be attributed to the deviation between experiments and our theory. Thus, the reported I_s of the GSAs used in the fiber lasers are in qualitative agreements with the theoretical considerations performed here [11, 12, 15, 41]. A special measurement with the use of the simplest geometry of a well-characterized graphene sample positioned on a semi-infinite substrate is necessary for more accurate comparison.

4.5 Discussion and conclusions

To summarize, a mathematical approximation model has been developed to theoretically analyze the conditions for realization of an efficient GSA. From the systematically theoretical investigation on the saturable absorption of an intrinsic graphene under ultrafast excitation, we found that the saturation intensity of graphene shows little dependence on its thickness, while the modulation depth is proportional to the number of layers of graphene. Moreover, the graphene placed on a substrate with higher refractive index (n_2) saturates at a higher intensity. The modulation depth of the graphene sample is found to decrease as n_2 increases. The spectral conditions of saturation of absorption were found in the visible-NIR spectral regions, which indicate the saturation intensity of graphene decrease as the light wavelength increases. The consideration performed demonstrates a frequency-independent saturation, different from other saturable absorbers based on bulk materials or heterostructures. Finally,

reports on saturable absorption of graphene from other groups have been compared with our results. It is concluded that graphene performs superiorly as a saturable absorber due to its ultrafast recovery time, broadband response, large modulation depth and low loss of scattering.

Our theoretical consideration is based on ideal monolayer graphene. However, in practice the graphene samples used in the experiments are not perfect .They consist of many defects [6] which may contribute to the optical scattering loss and other ambiguous influence on saturable absorption. The multilayer graphene samples used in the experiments could be interlayer coupled; therefore the linear energy dispersion relation of graphene needs further modification and the superposition between layers maybe no longer valid. Besides, unintentional doping in graphene samples which could originate from charge carrier transfer by defects [4, 5] and substrates [7-9] are not considered in our theory. This theoretical model is also limited by that the assumptions and approximations may not be satisfied in practice. In our calculation, carrier temperature evolution parameters are extracted from an experimental observation. Identical parameters are considered for different excitation intensity and wavelengths. However, the parameters might fluctuate from sample to sample due to graphene synthesis methods, substrates and sample quality. Also, time-averaging approximations are taken for photoexcited carrier density and the temperature of photo excited electrons. In addition, the spatial profile of pumping pulses, which might cause the lateral diffusion of carriers,[42] and a heating of phonons [43, 44] may be essential; these phenomena request a

special treatment both theoretically and experimentally. These shortcomings in our theoretical calculation and experiment require further improvements and optimizations.

References:

1. Wang, F.; Zhang, Y.; Tian, C.; Girit, C.; Zettl, A.; Crommie, M.; Shen, Y. R., Gate-variable optical transitions in graphene. *Science* **2008**, 320, 206.

2. Waldmann, D.; Jobst, J.; Speck, F.; Seyller, T.; Krieger, M.; Weber, H. B., Bottom-gated epitaxial graphene. *Nat. Mater.* **2011**, 10, 357.

3. Shi, Y.; Dong, X.; Chen, P.; Wang, J.; Li, L.-J., Effective doping of single-layer graphene from underlying SiO_2 substrates. *Phys. Rev. B* **2009**, 79, 115402.

4. Castro Neto, A. H.; Guinea, F.; Peres, N. M. R.; Novoselov, K. S.; Geim, A. K., The electronic properties of graphene. *Rev. Mod. Phys* **2009**, 81, 109.

5. Reich, S.; Maultzsch, J.; Thomsen, C.; Ordejón, P., Tight-binding description of graphene. *Phys. Rev. B* **2002**, 66, 035412.

6. Banhart, F.; Kotakoski, J.; Krasheninnikov, A. V., Structural defects in graphene. *Acs Nano* **2010**, 5, 26.

7. Chen, W.; Chen, S.; Qi, D. C.; Gao, X. Y.; Wee, A. T. S., Surface transfer p-type doping of epitaxial graphene. *J. Am. Chem. Soc.* **2007**, 129, 10418.

8. Gierz, I.; Riedl, C.; Starke, U.; Ast, C. R.; Kern, K., Atomic hole doping of graphene. *Nano Lett.* **2008**, 8, 4603.

9. Giovannetti, G.; Khomyakov, P. A.; Brocks, G.; Karpan, V. M.; van den Brink, J.; Kelly, P. J., Doping graphene with metal contacts. *Phys. Rev. Lett.* **2008**, 101.

10. Xing, G.; Guo, H.; Zhang, X.; Sum, T. C.; Huan, C. H. A., The physics of ultrafast saturable absorption in graphene. *Opt. Express* **2010**, 18, 4564.

11. Bao, Q. L.; Zhang, H.; Wang, Y.; Ni, Z. H.; Yan, Y. L.; Shen, Z. X.; Loh, K. P.; Tang, D. Y., Atomic-layer graphene as a saturable absorber for ultrafast pulsed lasers. *Adv. Funct. Mater.* **2009**, 19, 3077.

12. Sun, Z. P.; Hasan, T.; Torrisi, F.; Popa, D.; Privitera, G.; Wang, F. Q.; Bonaccorso, F.; Basko, D. M.; Ferrari, A. C., Graphene mode-locked ultrafast laser. *Acs Nano* **2010**, 4, 803.

13. Martinez, A.; Fuse, K.; Xu, B.; Yamashita, S., Optical deposition of graphene and carbon nanotubes in a fiber ferrule for passive modelocked lasing. *Opt. Express* **2010**, 18, 23054.

14. Song, Y. W.; Jang, S. Y.; Han, W. S.; Bae, M. K., Graphene mode-lockers for fiber lasers functioned with evanescent field interaction. *Appl. Phys. Lett.* **2010**, 96, 051122.

15. Martinez, A.; Fuse, K.; Yamashita, S., Mechanical exfoliation of graphene for the passive mode-locking of fiber lasers. *Appl. Phys. Lett.* **2011**, 99, 121107.

16. Kim, H.; Cho, J.; Jang, S.-Y.; Song, Y.-W.; Chang, Y. M.; Lee, J. H., Deformation-immunized optical deposition of graphene for ultrafast pulsed lasers. *Appl. Phys. Lett.* **2011**, 98, 021104.

17. Xu, J. L.; Li, X. L.; Wu, Y. Z.; Hao, X. P.; He, J. L.; Yang, K. J., Graphene saturable absorber mirror for ultra-fast-pulse solid-state laser. *Opt. Lett.* **2011**, 36, 1948.

18. Mishchenko, E. G., Dynamic conductivity in graphene beyond linear response. *Phys. Rev. Lett.* **2009**, 103, 246802.

19. Zhang, Z.; Voss, P. L., Full-band quantum-dynamical theory of saturation and four-wave mixing in graphene. *Opt. Lett.* **2011**, 36, 4569.

20. Vasko, F. T., Saturation of interband absorption in graphene. *Phys. Rev. B* **2010**, 82, 245422.

21. Dawlaty, J. M.; Shivaraman, S.; Strait, J.; George, P.; Chandrashekhar, M.; Rana, F.; Spencer, M. G.; Veksler, D.; Chen, Y. Q., Measurement of the optical absorption spectra of epitaxial graphene from terahertz to visible. *Appl. Phys. Lett.* **2008**, 93, 131905.

22. Dawlaty, J. M.; Shivaraman, S.; Chandrashekhar, M.; Rana, F.; Spencer, M. G., Measurement of ultrafast carrier dynamics in epitaxial graphene. *Appl. Phys. Lett.* **2008**, 92, 042116.

23. George, P. A.; Strait, J.; Dawlaty, J.; Shivaraman, S.; Chandrashekhar, M.; Rana, F.; Spencer, M. G., Ultrafast optical-pump terahertz-probe spectroscopy of the carrier relaxation and recombination dynamics in epitaxial graphene. *Nano Lett.* **2008**, 8, 4248.

24. Newson, R. W.; Dean, J.; Schmidt, B.; van Driel, H. M., Ultrafast carrier kinetics in exfoliated graphene and thin graphite films. *Opt. Express* **2009**, 17, 2326.

25. Breusing, M.; Ropers, C.; Elsaesser, T., Ultrafast carrier dynamics in graphite. *Phys. Rev. Lett.* **2009**, 102, 086809.

26. Breusing, M.; Kuehn, S.; Winzer, T.; Malic, E.; Milde, F.; Severin, N.; Rabe, J. P.; Ropers, C.; Knorr, A.; Elsaesser, T., Ultrafast nonequilibrium carrier dynamics in a single graphene layer. *Phys. Rev. B* **2011**, 83, 153410.

27. Sun, D.; Wu, Z. K.; Divin, C.; Li, X. B.; Berger, C.; de Heer, W. A.; First, P. N.; Norris, T. B., Ultrafast relaxation of excited dirac fermions in epitaxial graphene using optical differential transmission spectroscopy. *Phys. Rev. Lett.* **2008**, 101, 157402.

28. Huang, L. B.; Hartland, G. V.; Chu, L. Q.; Luxmi; Feenstra, R. M.; Lian, C. X.; Tahy, K.; Xing, H. L., Ultrafast transient absorption microscopy studies of carrier dynamics in epitaxial graphene. *Nano Lett.* **2010**, 10, 1308.

29. Shang, J.; Luo, Z.; Cong, C.; Lin, J.; Yu, T.; Gurzadyan, G. G., Femtosecond UV-pump/visible-probe measurements of carrier dynamics in stacked graphene films. *Appl. Phys. Lett.* **2010**, 97, 163103.

30. Obraztsov, P. A.; Rybin, M. G.; Tyurnina, A. V.; Garnov, S. V.; Obraztsova, E. D.; Obraztsov, A. N.; Svirko, Y. P., Broadband light-induced absorbance change in multilayer graphene. *Nano Lett.* **2011**, 11, 1540.

31. Strait, J. H.; Wang, H.; Shivaraman, S.; Shields, V.; Spencer, M.; Rana, F., Very slow cooling dynamics of photoexcited carriers in graphene observed by optical-pump terahertz-probe spectroscopy. *Nano Lett.* **2011**, 11, 4902.

32. Yee, K. J.; Kim, J. H.; Jung, M. H.; Hong, B. H.; Kong, K. J., Ultrafast modulation of optical transitions in monolayer and multilayer graphene. *Carbon* **2011**, 49, 4781.

33. Romanets, P. N.; Vasko, F. T., Transient response of intrinsic graphene under ultrafast interband excitation. *Phys. Rev. B* **2010**, 81, 085421.

34. Choi, H.; Borondics, F.; Siegel, D. A.; Zhou, S. Y.; Martin, M. C.; Lanzara, A.; Kaindl, R. A., Broadband electromagnetic response and ultrafast dynamics of few-layer epitaxial graphene. *Appl. Phys. Lett.* **2009**, 94.

35. Nair, R. R.; Blake, P.; Grigorenko, A. N.; Novoselov, K. S.; Booth, T. J.; Stauber, T.; Peres, N. M. R.; Geim, A. K., Fine structure constant defines visual transparency of graphene. *Science* **2008**, 320, 1308.

36. Mak, K. F.; Sfeir, M. Y.; Wu, Y.; Lui, C. H.; Misewich, J. A.; Heinz, T. F., Measurement of the optical conductivity of graphene. *Phys. Rev. Lett.* **2008**, 101, 196405.

37. Stauber, T.; Peres, N. M. R.; Geim, A. K., Optical conductivity of graphene in the visible region of the spectrum. *Phys. Rev. B* **2008**, 78, 085432.

38. Bonaccorso, F.; Sun, Z.; Hasan, T.; Ferrari, A. C., Graphene photonics and optoelectronics. *Nat. Photonics* **2010**, 4, 611.

39. Liu, Z.; Bol, A. A.; Haensch, W., Large-scale graphene transistors with enhanced performance and reliability based on interface engineering by phenylsilane self-assembled monolayers. *Nano Lett.* **2010**, 11, 523.

40. Schultz, B. J.; Patridge, C. J.; Lee, V.; Jaye, C.; Lysaght, P. S.; Smith, C.; Barnett, J.; Fischer, D. A.; Prendergast, D.; Banerjee, S., Imaging local electronic corrugations and doped regions in graphene. *Nat. Commun.* **2011**, 2, 372.

41. Sun, Z. P.; Popa, D.; Hasan, T.; Torrisi, F.; Wang, F. Q.; Kelleher, E. J. R.; Travers, J. C.; Nicolosi, V.; Ferrari, A. C., A stable, wideband tunable, near transform-limited, graphene-mode-locked, ultrafast laser. *Nano Res.* **2010**, 3, 653.

42. Partoens, B.; Peeters, F. M., From graphene to graphite: Electronic structure around the k point. *Phys. Rev. B* **2006**, 74, 075404.

43. Lui, C. H.; Mak, K. F.; Shan, J.; Heinz, T. F., Ultrafast photoluminescence from graphene. *Phys. Rev. Lett.* **2010**, 105, 127404.

44. Kaverzin, A. A.; Strawbridge, S. M.; Price, A. S.; Withers, F.; Savchenko, A. K.; Horsell, D. W., Electrochemical doping of graphene with toluene. *Carbon* **2011**, 49, 3829.

Chapter 5

Conclusions

5.1 Summary and results

This thesis aims to establish a mathematical model for quantitative understanding of the saturable absorption in graphene and to theoretically investigate the spectral dependence of saturation intensity in graphene as well as the effects of graphene layer numbers and substrates on the saturation. The main results discussed in previous chapters will be summarized here and the suggestions for future work will also be presented in this chapter.

In Chapter 2, the experimental observations on the nonequilibrium carrier dynamics in graphene associated with the cooling and recombination of photoexcited carriers were summarized. It has been theoretically argued and experimentally shown that following ultrafast photoexcitation, the charge carriers initially scatter and thermalize to quasiequilibrium with a characteristic time of tens of femtoseconds. These hot charge carriers subsequently lose a majority of their energy within hundreds of femtoseconds by transferring energy to the lattice via coupling to optical phonons (c-op scattering). In turn, the optical phonons subsequently relax through anharmonic coupling to acoustic phonons (op-ap scattering). Within several picoseconds, room temperature equilibrium

is finally restored via interband carrier relaxation processes dominated by e-h recombination. Based on the above-discussed photodynamics, previous theoretical models were critically reviewed on saturable absorption of graphene. These theories failed to give an explicit relation between the saturation intensity and the operating laser wavelength, number of graphene layers, as well as the substrates. In our study, we employed the photodynamic model to develop a mathematical approximation for quantitative explanations on the dispersion of saturable absorption in the intrinsic graphene due to Pauli blocking effects by the interband absorption. Our consideration is based on a set of assumptions about the carrier relaxation processes. Firstly, a simplified description of carrier relaxation and temperature evolution is assumed for different electron densities and different wavelengths. Secondly, time-averaging approximations are taken for photoexcited carrier density and photoexcited electron temperature in our treatment.

As discussed in Chapter 3, saturable absorption in epitaxial graphene was unambiguously determined by conducting Z-scan measurements on the monolayer, bilayer and six-layer graphene samples at 780 nm with 1 kHz, 400-fs laser pulses. It was found that the nonlinear signal increases linearly as the number of graphene layer is increased up to six, which indicates that the modulation depth can be enhanced by increasing the stacking of graphene layers. Furthermore, the spectral dependence of saturable absorption of graphene was systematically studied by extending Z-scan measurements from 780 nm to the spectral range of 900 nm to 1100 nm with

femtosecond laser pulses on epitaxial graphene. It was demonstrated that the saturation intensity of graphene is sensitively dependent on the operating wavelength, which reduces from ~5 GW/cm^2 to 1.5 GW/cm^2 as the operating wavelength increases from 900 nm to 1100 nm.

Systematically theoretical investigations on the saturable absorption of an intrinsic graphene under ultrafast excitation were presented in Chapter 4. The saturation intensity of graphene shows little dependence on its thickness, while the saturation depth is proportional to the number of layers of graphene. Moreover, the graphene placed on a substrate with higher refractive index (n_2) saturates at a higher intensity. It is also shown that the saturation depth of the graphene sample decreases as n_2 increases. Our mathematical model was validated by comparison with the experimental measurements of saturable absorption of epitaxial graphene in the spectral range from 780 nm to 1100 nm. The spectral conditions of saturation of absorption were found in the visible-near infrared spectral regions, revealing that the saturation intensity of graphene decrease as the light wavelength increases. Different from other saturable absorbers based on bulk materials and heterostructures, our study exhibits a broadband response of graphene as a saturable absorber. Finally, published literature on saturable absorption of graphene from other groups was compared with our results. It is concluded that graphene performs superiorly as a saturable absorber due to its ultrafast recovery time, broadband response, large modulation depth and low loss of scattering.

5.2 Suggestions for future work

The thesis has systematically investigated the saturable absorption in graphene. The main contributions of this work are in the development of a mathematical model to quantitatively study the saturable absorption of graphene and explicitly determine the dependence of the saturation intensity on the laser operating wavelength, number of graphene layers as well as the substrates, which is of paramount importance to the designing or engineering of graphene for mode-locking.

There are several interesting directions for future study related with the research presented in this thesis.

One possible avenue of future research is to investigate the dependence of the saturable absorption of graphene on doping effects. In this thesis, our calculation is restricted to the intrinsic graphene. However, graphene can be doped by either physical or chemical methods [1-3], where the nonlinear optical absorption could provide more desirable electro-optical applications. It has been observed that when graphene is doped, i.e. the distribution of electrons and holes are not symmetric about the Dirac point, 2.3% universal linear optical absorption of graphene becomes non-universal at low photon energy due to state blacking [4]. The interband absorption is minimized when the Fermi level approaches half of the excitation photon energy. Although the doping effect on the interband absorption was already observed at low excitation levels [1, 4], the effects of doping on the saturable absorption have, to the best of our knowledge, not been investigated.

Another direct extension of this work would be to perform the detail investigations on the saturable absorption of CVD graphene. The saturation intensity of CVD graphene samples was shown to be almost three orders lower than the value of graphene samples synthesized by other methods [5-12]. Such lower saturation intensity might be induced from the unique characteristic of CVD graphene. It was reported that the electronic mobility of CVD graphene is much lower than that of exfoliated and epitaxial graphene, due to the local electronic corrugations and doped regions in CVD graphene [13-15]. Nevertheless, to the best of our knowledge, no theory is capable of describing CVD-growth graphene with low saturation intensity to date, which is worthwhile for further systematic investigations.

Recently, a surprisingly giant nonlinear refractive index of graphene ($n_2 \approx 10{-}7$ cm^2W^{-1}) was observed using Z-scan technique [16], which is almost nine orders of magnitude larger than the bulk dielectrics. This suggests that graphene might be a promising nonlinear medium, which paves the way for graphene-based nonlinear photonics. In the theoretical view, we have demonstrated that, from the Equations (2.8-2.10), the real part of the optical conductivity contributes to absorption primarily, whereas the imaginary part will result in a phase shift. Therefore, the third possible avenue of future research is to unambiguously distinguish the nonlinear phase shift of graphene under strong laser illumination theoretically.

References:

1. Wang, F.; Zhang, Y.; Tian, C.; Girit, C.; Zettl, A.; Crommie, M.; Shen, Y. R., Gate-variable optical transitions in graphene. *Science* **2008**, 320, 206.

2. Waldmann, D.; Jobst, J.; Speck, F.; Seyller, T.; Krieger, M.; Weber, H. B., Bottom-gated epitaxial graphene. *Nat. Mater.* **2011**, 10, 357.

3. Shi, Y.; Dong, X.; Chen, P.; Wang, J.; Li, L.-J., Effective doping of single-layer graphene from underlying SiO_2 substrates. *Phys. Rev. B* **2009**, 79, 115402.

4. Mak, K. F.; Sfeir, M. Y.; Wu, Y.; Lui, C. H.; Misewich, J. A.; Heinz, T. F., Measurement of the optical conductivity of graphene. *Phys. Rev. Lett.* **2008**, 101, 196405.

5. Bao, Q. L.; Zhang, H.; Wang, Y.; Ni, Z. H.; Yan, Y. L.; Shen, Z. X.; Loh, K. P.; Tang, D. Y., Atomic-layer graphene as a saturable absorber for ultrafast pulsed lasers. *Adv. Funct. Mater.* **2009**, 19, 3077.

6. Bao, Q. L.; Zhang, H.; Ni, Z. H.; Wang, Y.; Polavarapu, L.; Shen, Z. X.; Xu, Q. H.; Tang, D. Y.; Loh, K. P., Monolayer graphene as a saturable absorber in a mode-locked laser. *Nano Res.* **2011**, 4, 297.

7. Tan, W. D.; Su, C. Y.; Knize, R. J.; Xie, G. Q.; Li, L. J.; Tang, D. Y., Mode locking of ceramic nd:Yttrium aluminum garnet with graphene as a saturable absorber. *Appl. Phys. Lett.* **2010**, 96, 031106.

8. Zhang, H.; Bao, Q. L.; Tang, D. Y.; Zhao, L. M.; Loh, K., Large energy soliton erbium-doped fiber laser with a graphene-polymer composite mode locker. *Appl. Phys. Lett.* **2009**, 95, 141103.

9. Zhang, H.; Tang, D. Y.; Knize, R. J.; Zhao, L. M.; Bao, Q. L.; Loh, K. P., Graphene mode locked, wavelength-tunable, dissipative soliton fiber laser. *Appl. Phys. Lett.* **2010**, 96, 111112.

10. Zhang, H.; Tang, D. Y.; Zhao, L. M.; Bao, Q. L.; Loh, K. P., Large energy mode locking of an erbium-doped fiber laser with atomic layer graphene. *Opt. Express* **2009**, 17, 17630.

11. Martinez, A.; Fuse, K.; Yamashita, S., Mechanical exfoliation of graphene for the passive mode-locking of fiber lasers. *Appl. Phys. Lett.* **2011**, 99, 121107.

12. Sun, Z. P.; Hasan, T.; Torrisi, F.; Popa, D.; Privitera, G.; Wang, F. Q.; Bonaccorso, F.; Basko, D. M.; Ferrari, A. C., Graphene mode-locked ultrafast laser. *Acs Nano* **2010**, 4, 803.

13. Bonaccorso, F.; Sun, Z.; Hasan, T.; Ferrari, A. C., Graphene photonics and optoelectronics. *Nat. Photonics* **2010**, 4, 611.

14. Liu, Z.; Bol, A. A.; Haensch, W., Large-scale graphene transistors with enhanced performance and reliability based on interface engineering by phenylsilane self-assembled monolayers. *Nano Lett.* **2010**, 11, 523.

15. Schultz, B. J.; Patridge, C. J.; Lee, V.; Jaye, C.; Lysaght, P. S.; Smith, C.; Barnett, J.; Fischer, D. A.; Prendergast, D.; Banerjee, S., Imaging local electronic corrugations and doped regions in graphene. *Nat. Commun.* **2011**, 2, 372.

16. Zhang, H.; Virally, S.; Bao, Q.; Kian Ping, L.; Massar, S.; Godbout, N.; Kockaert, P., Z-scan measurement of the nonlinear refractive index of graphene. *Opt. Lett.* **2012**, 37, 1856.